

UNIVERSITY OF CRETE



DEPARTMENT OF MATERIALS SCIENCE AND TECHNOLOGY

**Device Engineering for enhanced Performance &  
Stability of Organic Photovoltaics**

George Kakavelakis

July 2015

Supervisors: Dr. Emmanuel Stratakis, Prof. Emmanuel Kymakis

## Abstract

*The effect of metallic (free of surfactants and ligand coated) nanoparticles (NPs) incorporated into different photoactive (P3HT:PCBM, P3HT:ICBA and PCDTBT:PC<sub>71</sub>BM) and interfacial layers (TiO<sub>x</sub>) of bulk heterojunction (BHJ) organic photovoltaic (OPV) devices was systematically studied. It was evidenced that the NPs doping gives rise to photovoltaic (PV) efficiency and enhanced stability, thereby lowering device degradation rate during prolonged illumination. Spectroscopic analysis combined with photon-to-electron conversion efficiency measurements indicate that the efficiency improvement can be attributed to enhanced light harvesting and subsequent higher exciton generation rate into the photoactive layer. Therefore, this enhancement is attributed to localized surface plasmon resonant absorption (Au NPs) and scattering effects (Al NPs). Furthermore, it was demonstrated that the device performance was improved only in the case that metal NPs were in close proximity or even better in direct contact with polymer donor (bare or coated with the same ligand as the donor material). On the other hand, the introduction of Au nanorods (NRs) inside the TiO<sub>x</sub> back contact interfacial layer acts as a mirror in the device structure, increasing exciton generation through back contact scattering and thus charge collection. The most efficient cells produced in this work incorporating Au NRs into TiO<sub>x</sub> transport layer of a PTB7:PC<sub>71</sub>BM based photoactive layer, demonstrated power conversion efficiency (PCE) of 8.25 %, with J<sub>sc</sub> of 17.46 mA/cm<sup>2</sup>, Voc of 0.76V and FF of 0.62.*

## Acknowledgments

*I would like to express my deepest gratitude to my supervisors, Dr. Emmanuel Stratakis and Prof. Emmanuel Kymakis, for giving me the opportunity to carry out this project in their group and for their supervision and guidance along the project. I genuinely thank them for their continuous positive and encouraging attitude and for always being great leaders to look up to. I finally thank them for all the projects, tasks and challenges that have been given to me and that helped me expand significantly my knowledge in the field.*

*Additionally, i would like to thank my friend and contributor Prof. Costas Petridis for his guidance and useful comments along the writing of this thesis.*

*Moreover, i would like to give my thanks to all the lab members, Minas Stylianakis, Dimitrios Konios, Anna Orfanoudaki, Miron Krassas and Pavlos Tzourmpakis for their support.*

*Furthermore, i am sincerely grateful to an old member of this group, George D. Spyropoulos, for sharing his experience and for his kind advices at the first steps of my work.*

*Finally, i would like to give all my gratitude to a very important person of my life, my girlfriend Georgia Perathoraki, who was there with a smile every time i felt disappointed.*

*Dedicated to my parents, Joseph Kakavelakis & Amalia Xenaki, to  
my grandmother Stella-Aikaterini Volaka-Xenaki and to my uncle  
Stelios Xenakis*

## Abbreviations and Symbols

AM	Air Mass
BHJ	Bulk heterojunction
HOMO	Highest occupied molecular orbital
ITO	Indium tin oxide
$J_{sc}$	Short Circuit current density
LSPR	Localize plasmon resonance
LSPs	Localize surface plasmons
LUMO	Lowest unoccupied molecular orbital
OPVs	Organic Photovoltaics
P3HT	Poly(3-hexylthiophene-2,5-diyl)
PCDTBT	Poly[N-9-hepta-decanyl-2,7-carbazolealt-5,5-(4,7-di-2-thienyl-2,1,3-benzothiadiazole)]
PTB7	Poly[[4,8-bis[(2-ethylhexyl)oxy]benzo[1,2-b:4,5-b']dithiophene-2,6-diyl][3-fluoro-2-[(2-ethylhexyl)carbonyl]thieno[3,4-b]thiophenediyl]
PC <sub>71</sub> BM	Phenyl-C71-butyric acid methyl ester
PCBM	Phenyl-C61-butyric acid methyl ester
PEDOT:PSS	Poly(3,4-ethylenedioxythiophene) poly(styrenesulfonate)
SPPs	Surface plasmon polaritons
TEM	Transmission electron microscopy
$V_{oc}$	Open circuit voltage
FF	Fill Factor
DCB	Dichlorobenzene
CB	Chlorobenzene
EQE	External Quantum Efficiency
PCE	Power Conversion Efficiency
HTL	Hole transporting layer
ETL	Electron transporting layer

$J_{ph}$  Photocurrent density

DIO 1,8-diiodooctane

## Table of Contents

Abstract .....	2
Acknowledgments .....	3
Abbreviations and Symbols.....	5
Introduction.....	8
Organic Electronic Materials .....	14
Bulk Heterojunction Organic Solar Cells.....	26
Plasmonic Theory .....	33
Experimental Procedures .....	52
Results and Discussion .....	69
Conclusions and Future Directions.....	112
List of Publications.....	114

# Chapter 1

## Introduction

### 1.1 Solar Energy

When the global warming and depletion of common used energy supplies, such as fossil fuels started threatening the balance of human life, great attention was driven towards the renewable (alternative) energy sources. Among number of renewable energy sources, such as wind energy, hydroelectric energy, biomass and geothermal energy, solar energy has the highest potential. A very small fraction of sun power (less than 0.02 %) reaching the earth surface can satisfy the worldwide energy needs.. Yet, by the end of year 2014, solar technology based sources have been providing only 0.9 % of all the energy consumed by humans according to Renewable Energy Policy Network (REN21) report<sup>1</sup>.

There are various solar technologies for harvesting the sun energy, which can be divided to two categories: passive solar and active solar. An example of passive technique can be the designing of a building in such a way that it efficiently harvests and stores the sun energy in it. Active solar technologies are the solar thermal collectors or photovoltaic (PV) devices. However, the fastest and most efficient direct conversion of sun light into electrical energy is possible only through photovoltaic devices. The PV effect, discovered by Becquerel<sup>2,3</sup> is the fundamental physical process, by which the semiconductor material converts electromagnetic radiation (sun light) into electrical power.

The paradox is that despite our environment is surrounded with abundant solar power, the PV technology is still too expensive to become a primary energy source. Therefore, the main task of the solar cell research community is to develop a technology, which can provide cheap PV products and make the photo-conversion of sun light into electrical power cost efficient.

### 1.2 Solar Cell Generations

---

<sup>1</sup>[http://www.ren21.net/wp-content/uploads/2015/06/GSR2015\\_KeyFindings\\_lowres.pdf](http://www.ren21.net/wp-content/uploads/2015/06/GSR2015_KeyFindings_lowres.pdf)

<sup>2</sup>A. E. Becquerel, *Comptes Rendus De L'Académie Des Sciences*, 1839, 9, 145.

<sup>3</sup> A. E. Becquerel, *Comptes Rendus De L'Académie Des Sciences*, 1839, 9, 561.

So far photovoltaic devices (solar cells) can be categorized in three technology generations according to the timeline of their development<sup>4</sup>.

The first generation (1G) solar cells are large scale, single junction devices. Most of the production is based on silicon wafers including single crystal and multi-crystalline silicon. About 90 % of the current photovoltaic production is based on first generation. The efficiency of the single junction cells has a theoretical limit of about 30% (the Shockley–Queisser limit)<sup>5,6</sup> and currently the common silicon wafer based devices show nearly 20% efficiency with the highest reported efficiencies reaching 25%<sup>7</sup>. Yet, the cost per produced Watt is nearly 4 times higher than conventional energy sources' prices due to the material's used high cost (half of the cost of 1G devices is the silicon wafer) and high manufacturing & processing expenses. Although, the cost lowers along with the progress of the technology, the 1G products will probably reach their price limit before achieving the competitive level in the market.

The second generation (2G) solar cells are addressing the cost issue and the primary task is to decrease the amount of expensive material used in the production process while keeping the efficiency of the device high. The foremost approach is producing thin film solar cells on low cost substrates (such as glass and flexible substrates such as PET). Different techniques are utilized for production process such as solution deposition, vapor deposition, electroplating and etc. Most successful materials for 2G are amorphous silicon, CuIn(Ga)Se<sub>2</sub> (CIGS), CdTe/CdS, which are being deposited on thin substrates. Devices based on these materials can deliver lab efficiencies up to 19 %, but the module efficiencies are reaching only 14 % due to difficulties in producing large-scale uniform films<sup>7</sup>. Although thin film technology can significantly decrease the PVs fabrication budget, 2G solar cells will be constrained by certain cost ceilings per watt due to efficiency limits and the material costs.

The third generation (3G): The alternative way to get the cost down is to increase the efficiency by multiple stacking (sandwich) of solar cells. 3G solar cells introduce the idea of multi junction solar cells, which can significantly increase the device efficiency via improvement in harvesting of photons and even overcome the theoretical limit of 30 %. Currently the highest efficiencies reported for multi-junction solar cells are over 33 %<sup>7</sup>.

---

<sup>4</sup> D. M. Bagnall and M. Boreland, *Photovoltaic technologies, Energy Policy*, 2008, 36, 4390-4396

<sup>5</sup>W. Shockley and H. J. Queisser, Detailed Balance Limit of Efficiency of P-N Junction Solar Cells, *J.Appl.Phys.*, 1961, 32, 510-519.

<sup>6</sup> M. C. Hanna and A. J. Nozik, Solar conversion efficiency of photovoltaic and photo electrolysis cells with carrier multiplication absorbers, *J.Appl.Phys.*, 2006, 100, 074510.

<sup>7</sup> M. A. Green, K. Emery, Y. Hishikawa, and W. Warta, Solar Cell Efficiency Tables (Version 34), *Prog.Photovolt: Res.Appl.*, 2009, 17, 320-326.

In addition, 3G utilizes completely new concepts in terms of device architectures and materials. As an example, three typical approaches of photovoltaics are Dye – Sensitized Solar Cells (DSSCs)<sup>8,9</sup>, Perovskite Solar Cells (PeSCs) and Organic Photovoltaics (OPVs). DSSCs are based on combination of dyes with metal oxides and electrolyte. The efficiencies of DSSC are in the range of 12 % for small lab scale devices, while the lifetime of the devices is rather low compared to inorganic solar cells. Similar to the sensitization in DSSCs, in PeSCs the perovskite material is coated onto a charge-conducting mesoporous scaffold most commonly TiO<sub>2</sub> – as light-absorber. The efficiencies of PeSCs have already exceeding 20% and their future promises to be bright. On the other hand OPV technology is based on organic compounds such as conjugated polymers and fullerenes blended together forming heterojunctions in the nanoscale. The OPVs record certified performance has overcome the level of 10% using simple deposition techniques and low cost fabrication materials.

Anthracene was the first organic compound in which photoconductivity has been observed by Pochettino in 1906<sup>10</sup> and which launched a new era for studying organic compounds for electronic applications. Particularly in the last decade the field of OPVs has been growing really fast and showing promising potential for rather cheap PV technology. For that reason, in recent years OPVs became one of the most fascinating fields of research due to their promising advantages.

---

<sup>8</sup> M. Gratzel, Photoelectrochemical cells, *Nature*, 15-11-2001, 414, 338-344.

<sup>9</sup> M. K. Nazeeruddin, A. Kay, I. Rodicio, R. Humphry-Baker, E. Mueller, P. Liska, N. Vlachopoulos, and M. Graetzel, *J.Am.Chem.Soc.*, 1-5-2002, 115, 6382-6390.

<sup>10</sup> A. Pochettino, *Acad.Lincei Rend.*, 1906, 15, 355.

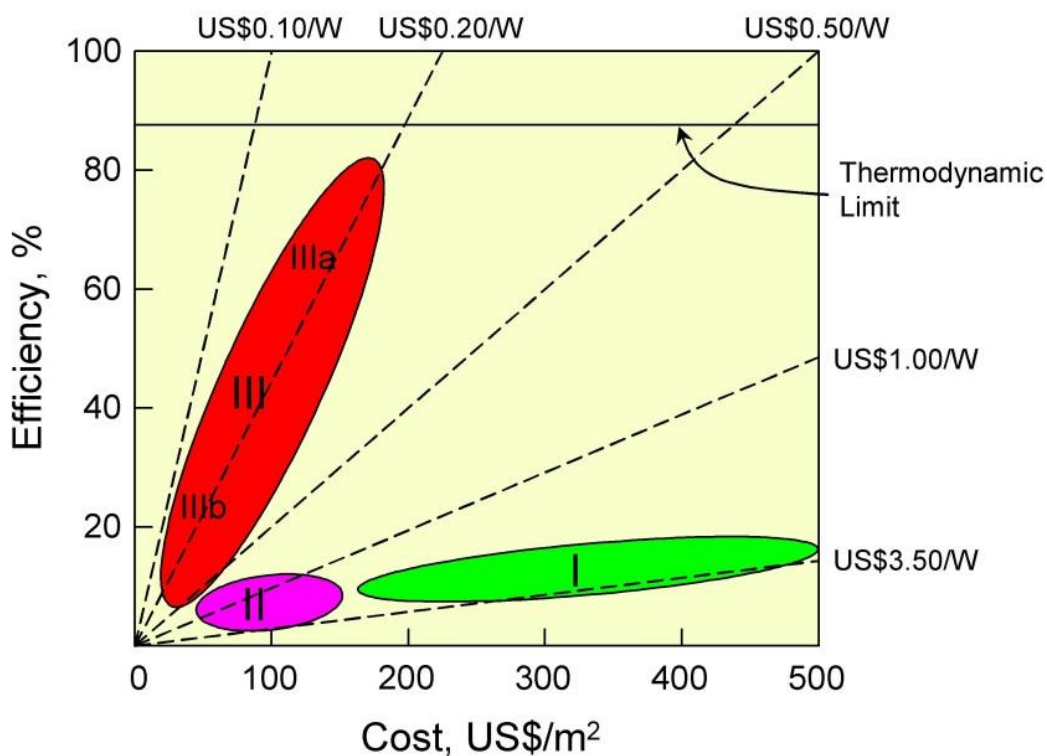


Figure 1.1 Efficiency dependence on cost for the three photovoltaic technology generations<sup>11</sup>. OPVs are enlisted in the category IIIb.

### 1.3 Organic Solar Cells: Benefits and Requirements

OPVs that use conjugated polymers offer the possibility of low cost, exploitation of less toxic manufacturing methods and the option to use large area, light weight, flexible substrate panels. Conjugated polymers are organic molecules with alternating single and double carbon-carbon bonded atoms and their electrical conductivity ranges from that of insulators to that of metals. They combine both the optoelectronic properties of semiconductors, the excellent mechanical and processing properties of polymeric materials and can be fabricated easily & cheaply by many solution processing techniques such as printing, doctor-blading, slot die and roll-to-roll on top of any selected substrate. These characteristics give a great advantage for the commercialization of OPVs compared to any other competitive technology.

Despite these advantages, OPVs, similar with its counterparts, have to fulfill the basic requirements for renewable energy production. In the energy market the competitive position of every solar technology is mainly determined by factors such as its efficiency, its lifetime and its costs regarding the electricity generation (per Wp). The potential of organic photovoltaics has to be judged by these key figures as well, and two of them are drawbacks at the present. Fig.1.2 depicts the requirements that

<sup>11</sup> [http://depts.washington.edu/cmditr/modules/opv/solar\\_technologies.html](http://depts.washington.edu/cmditr/modules/opv/solar_technologies.html)

organic photovoltaics simultaneously should satisfy in order to be commercialized. A product development succeeding in only two aspects like, e.g. competitive costs and reasonable efficiency, will only be able to address niche markets unless the third parameter, in that case, life time, is also optimized.

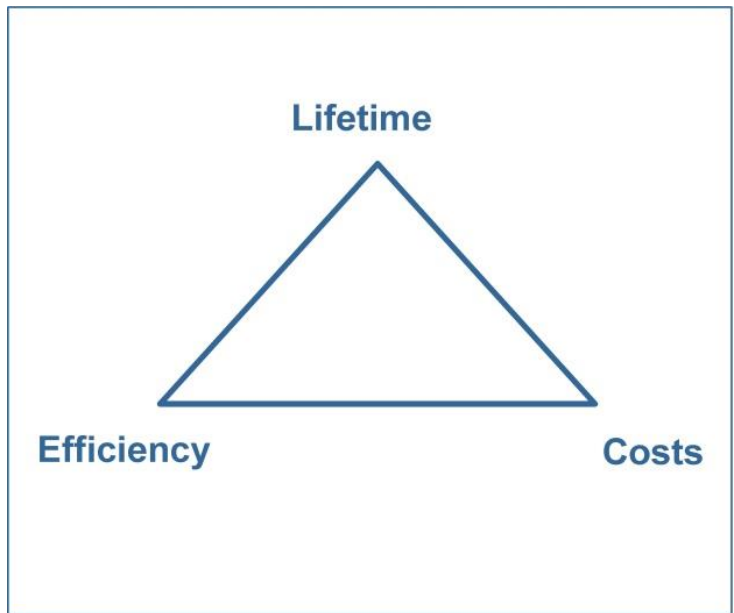


Figure 1.2 The critical triangle for photovoltaics with the three key factors

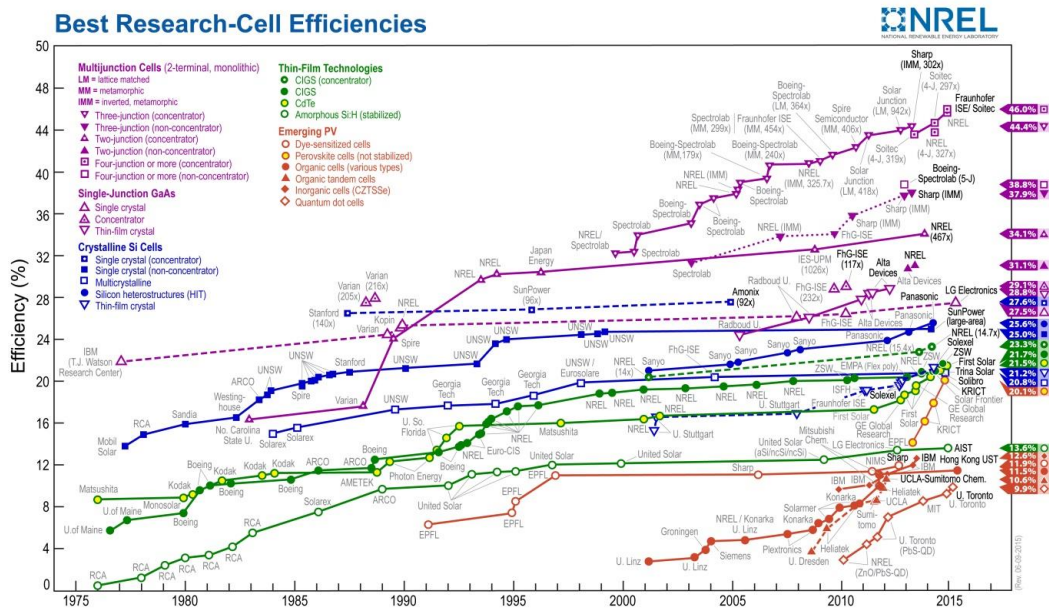


Figure 1.3 Best research-cell efficiencies for several technologies presented by the National Renewable Energy Laboratory<sup>12</sup> (June 2015)

### 1.4 Motivation

<sup>12</sup> [http://www.nrel.gov/ncpv/images/efficiency\\_chart.jpg](http://www.nrel.gov/ncpv/images/efficiency_chart.jpg)

The experimental objectives of this thesis were the manufacturing, analysis and optimization of OPV and plasmonic OPV devices, by incorporating metallic nanostructures. The main issue of OPVs is the low active layer absorption due to several limitations of organic electronic materials that will be detailed analyzed in chapter 2. The novel concept of metal nanostructures introduction inside the OPV devices will be explained and be supported with spectroscopic analysis in order to have a clear insight for mechanism responsible for the performance and stability behavior of the hybrid cells. Furthermore, the theoretical part includes the interpretation of these materials and devices operational principles

## Chapter 2

### Organic Electronic Materials

#### 2.1 Conjugated Polymers

Heeger, MacDiarmid and Shirakawa demonstrated in 1977 that chemical doping of conjugated polymers results in an increase of the latter's electronic conductivity by several orders of magnitude. This discovery was awarded with the Nobel Prize in chemistry in 2000<sup>13, 14</sup>. Most organic semiconductor materials are conjugated polymers that essentially consist of a linear framework of alternating single and double bonds between the carbon atoms along the polymer backbone. Conjugated polymers are nowadays used in various organic electronic applications, like transistors, photodiodes, light emitting diodes, solar cells, etc. The origin of the conductivity and semi-conductivity behavior in conjugated polymers, e.g. polyacetylene, is due to alternation of single and double bonds across their molecular structure which comes as a result of chemical bonding behavior of the carbon atoms (see Figure. 2.1).

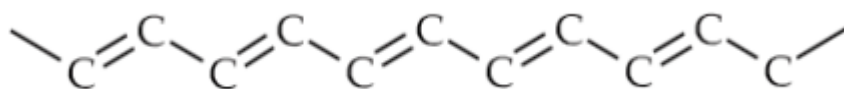


**Figure 2.1** The chain of the carbon atoms with the alternating single and double bonds<sup>15</sup>.

The carbon atom, in the ground state, has four valence electrons, 2 in 2s and 2 in 2p orbitals. In conjugated polymers carbon atoms are  $sp^2$  hybridized. In the  $sp^2$  hybridization the 2s orbital is hybridized with two 2p orbitals ( $2p_x$ ,  $2p_y$ ) giving rise to three  $sp^2$  orbitals and one 2p orbital ( $2p_z$ ) is left (unhybridized). Carbon can form two types of bonds: the  $\sigma$ -bond is formed by the overlap of the hybridized orbitals of the adjacent atoms which are oriented along the chain. So there are three coplanar  $sp^2$  hybridized orbitals which are at an angle of  $120^\circ$  with each other. Therefore three  $\sigma$  bonds are formed, two with neighbor carbon atoms and one with a hydrogen atom. The remaining out of plane  $p_z$  orbitals, each occupied by one electron, overlap with neighboring  $p_z$  orbitals to form bonds which are perpendicular to the chain shown. These electrons are delocalized along the entire polymer backbone, which is the reason for the conducting properties of conjugated polymers.

<sup>13</sup> C. K. Chiang, C. R. Fincher, Y. W. Park, A. J. Heeger, H. Shirakawa, E. J. Louis, S. C. Gau, and A. G. MacDiarmid: Electrical conductivity in doped polyacetylene. *Phys. Rev. Lett.*, Vol. 39, 1098, 1977.

<sup>14</sup> Shirakawa H., Louis E.J., Macdiarmid A.G., et al. *J.C.S. Chem. Comm.* 16 578-580 (1977)

<sup>15</sup> <http://www.chemphys.lu.se/old/kfresearch/com-conjupol.html>

The overlap of  $p_z$  orbitals forms two molecular orbitals, a bonding  $\pi$ -orbital which is the highest occupied molecular orbital (HOMO) and an antibonding  $\pi^*$ -orbital which is the lowest unoccupied orbital (LUMO). The  $\pi$ -orbital and  $\pi^*$ -orbital are equivalent to the valence band and conduction band of an inorganic semiconductor, respectively. The difference between the HOMO and LUMO is called the band gap of the organic material. The optical and electrical properties of an organic material are determined by the band gap. The gap is reduced when the polymer chain is longer. The chemical structure and schematic drawing of ethylene is illustrated in Figure 2.2, which is the simplest example of a conjugated molecule.

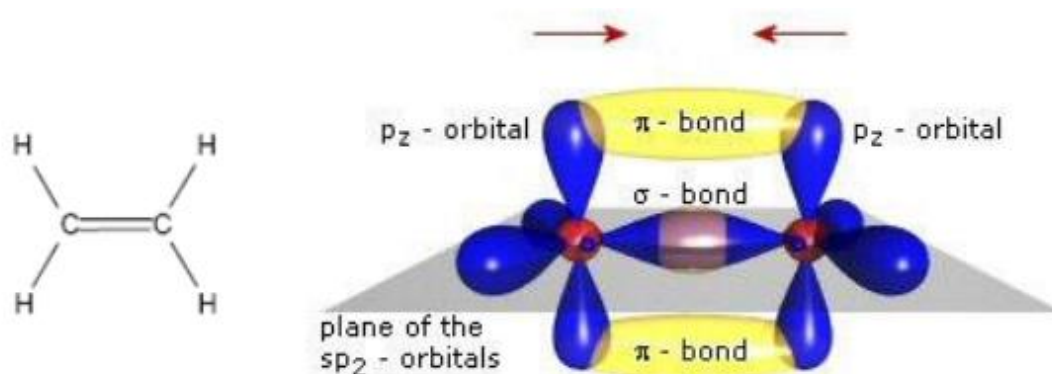


**Figure 2.2** Chemical structure and schematic drawing of ethylene.

## 2.2 Excitons

The concept of excitons is well known in the field of semiconductors and molecular crystals but its existence has been the subject of controversy in the polymer field. For inorganic semiconductors, the exciton is defined as an electron-hole pair bound by Coulomb attraction (Wannier exciton). In molecular crystals, the exciton can be considered as a bound electron-hole pair localised on one molecular unity (molecular exciton or Frenkel exciton). It is also electrically neutral and is characterized by an electric dipole moment. When a photon of light of the appropriate energy interacts with an electron in the ground state, the electron is excited from the HOMO (valence) to the LUMO (conduction) ( $\pi$ - $\pi^*$  transition). However, the resulting electron and hole are still bound, and their motion through the material is coupled. These coupled pairs are known as excitons. An exciton can be considered as a Frenkel exciton, if the pair is confined to one molecular unit or as a Mott-Wannier exciton if it extends over many molecular units<sup>16</sup>. The intermediate case, where the exciton extends over a few adjacent molecular units, can be called the charge-transfer exciton. Also, the terms “inter-chain” and “intra-chain” exciton are used for polymeric semiconductors to indicate that the constituent charges are located on different or on the same polymer chains respectively.

<sup>16</sup> N. C. Gree nham and R. H. Friend, *Solid State Physics* 49, 1 (1995).

The exciton binding energy of conjugated polymers depends strongly on their's structure<sup>17</sup>. For highly crystalline polydiacetylene, the binding energy has been determined to be 0.5 eV, while for amorphous polymers like the polythiophene and PPV, is about 0.4 eV<sup>18,19</sup>.

## 2.3 Polythiophenes

Polythiophenes (PTs)<sup>20</sup> result from the polymerization of thiophenes, a sulfur heterocycle, that can become conducting when electrons are added or removed from the conjugated  $\pi$ -orbitals via doping. Poly(3-hexylthiophene) (P3HT) is one of the most famous and commonly used polymers of this family. It simply has one additional carbohydrate chain in the position 3 of the sulfur heterocycle. Poly[[4,8-bis[(2-ethylhexyl)oxy]benzo[1,2-b:4,5-b']dithiophene-2,6-diyl][3-fluoro-2-[(2-ethylhexyl)carbonyl]thieno[3,4-b]thiophenediyl] (PTB7) is a polythiophene based copolymer and is considered as one of the most efficient donor material used in BHJ OPV devices<sup>21</sup>.

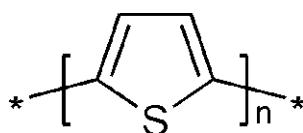


**Figure 2.3** Repeating unit (monomer) of polythiophene<sup>22</sup>

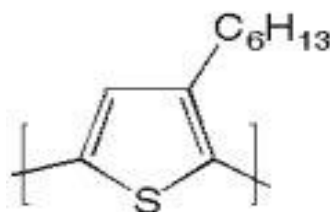


**Figure 2.4** Repeating unit of P3HT<sup>23</sup>

<sup>17</sup> S. Mazumbar, M. Chandross, and N. S. Sariciftci, Primary photoexcitations in conjugated polymers (*World Scientific, Singapore*, 1997).

<sup>18</sup> E. M. Conwell and H. A. Mizes, *Physical Review B* 51, 6953 (1995).

<sup>19</sup> R. N. Marks, J. J. Halls, D. D. C. Bradley, R. H. Friend, and A. B. Holmes, *Journal of Physics-Condensed Matter* 6, 1379 (1994).

<sup>20</sup> Street, G. B.; Clarke, T. C. *IBM J. Res. Dev.* **1981**,25, 51–57.

<sup>21</sup> Y. Liang, Z. Xu, J. Xia, S.-T. Tsai, Y. Wu, G. Li, C. Ray, L. Yu, *Adv. Mater.*, 2010, 22, E135-E138

<sup>22</sup> <http://www.wikiwand.com/en/Polythiophene>

<sup>23</sup> <http://www.sigmaaldrich.com/materials-science/organic-electronics/polymer-semiconductors.html>

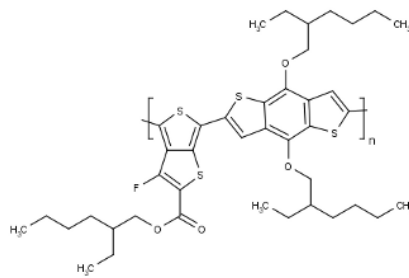


**Figure 2.5** Repeating unit of PTB7<sup>24</sup>

## 2.4 Polycarbazoles

Polycarbazoles (PCs) result from the polymerization of Carbazoles. Carbazole is an aromatic heterocyclic organic compound. It has a tricyclic structure, consisting of two six-membered benzene rings fused on either side of a five-membered nitrogen-containing ring. The compounds' structure is based on the indole structure but in which a second benzene ring is fused onto the five-membered ring at the 2–3 position of indole (equivalent to the 9a–4a double bond in carbazole respectively). Low band gap Poly[N-9'-heptadecanyl-2,7-carbazole-alt-5,5-(4',7'-di-2-thienyl-2',1',3'-benzothiadiazole)] (PCDTBT) is one of the most promising high efficient donor materials for OPV devices<sup>25</sup> demonstrating PCEs over than 6% so far and resulting to more stable devices against degradation<sup>26</sup>.

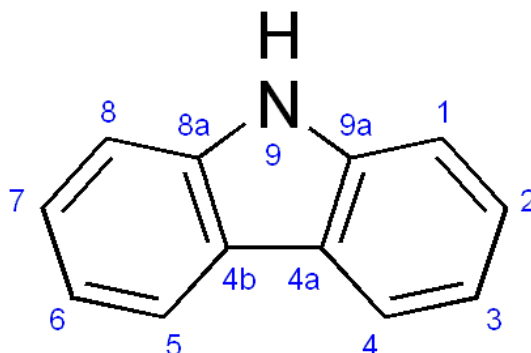


**Figure 2.6** Repeating unit (monomer) of Polycarbazole<sup>27</sup>

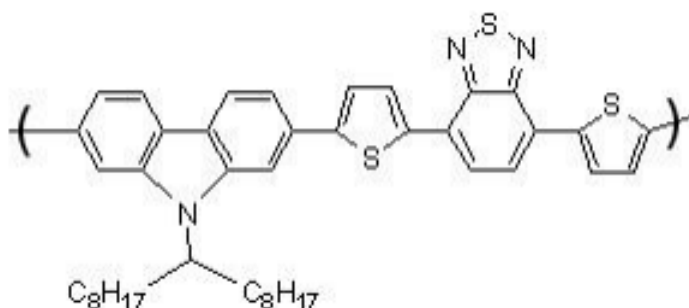


**Figure 2.7** Repeating unit of PCDTBT conjugated polymer<sup>28</sup>

<sup>24</sup> <http://www.ossila.com/products/ptb7>

<sup>25</sup> N. Blouin, A. Michaud and M. Leclerc, *Adv. Mater.*, 2007, 19, 2295–2300

<sup>26</sup> Sung Heum Park et. al., *Nature Photonics* 3, 297 - 302 (2009)

<sup>27</sup> <https://en.wikipedia.org/wiki/Carbazole>

<sup>28</sup> <http://www.ossila.com/products/pcdtbt>

## 2.5 Conjugation length and optical properties

The extended  $\pi$ -systems of conjugated PTs produce some of the most interesting properties of these materials—their optical properties. As an approximation, the conjugated backbone can be considered as a real-world example of the “electron-in-a-box” solution to the Schrödinger equation; however, the development of refined models to accurately predict absorption and fluorescence spectra of well-defined oligo(thiophene) systems is ongoing<sup>29</sup>. Conjugation relies upon overlap of the  $\pi$ -orbitals of the aromatic rings, which, in turn, requires the thiophene rings to be coplanar.

The number of coplanar rings determines the conjugation length—the longer the conjugation length, the lower the separation between adjacent energy levels, and the longer the absorption wavelength. Deviation from coplanarity may be permanent, resulting from mislinkages during synthesis or especially bulky side chains; or temporary, resulting from changes in the environment or binding. This twist in the backbone reduces the conjugation length (see Figure 2.8, bottom), and the separation between energy levels is increased. This results in a shorter absorption wavelength.

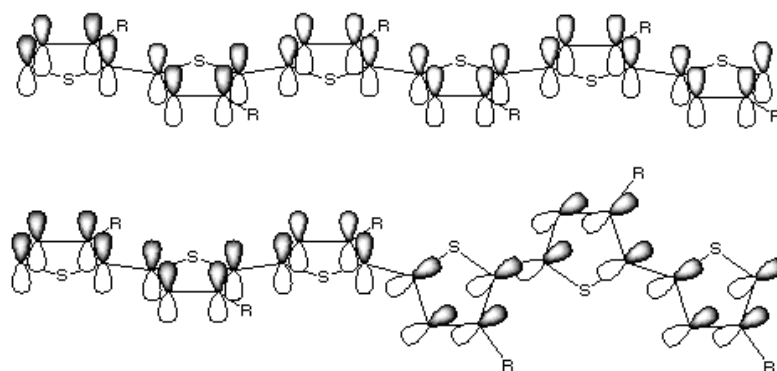


**Figure 2.8** Conjugated  $\pi$ -orbitals of a coplanar and a twisted substituted PT<sup>22</sup>.

Determining the maximum effective conjugation length requires the synthesis of regioregular PTs of defined length. The absorption band in the visible region is increasingly red-shifted as the conjugation length increases, and the maximum effective conjugation length is calculated as the saturation point of the red-shift. Early studies by ten Hoeve *et al.* estimated that the effective conjugation extended over 11 repeat units, while later studies increased this estimate to 20 units. More recently, Otsubo *et al.* synthesized and 96-mer<sup>21</sup> oligothiophenes, and found that the red-shift, while small (a difference of 0.1 nm between the 72- and the 96-mer), does not saturate, meaning that the effective conjugation length may be even longer than 96 units.

<sup>29</sup> [http://en.wikipedia.org/wiki/P3ht#cite\\_note-16](http://en.wikipedia.org/wiki/P3ht#cite_note-16)

A variety of environmental factors can cause the conjugated backbone to twist, reducing the conjugation length and causing an absorption band shift, including solvent, temperature, application of an electric field, and dissolved ions. The absorption band of poly(3-thiophene acetic acid) in aqueous solutions of poly(vinyl alcohol)(PVA) shifts from 480 nm at pH 7 to 415 nm at pH 4. This is attributed to formation of a compact coil structure which can form hydrogen bonds with PVA upon partial deprotonation of the acetic acid group. Chiral PTs showed no induced circular dichroism (ICD) in chloroform, but displayed intense, but opposite, ICDs in chloroform–acetonitrile mixtures versus chloroform–acetone mixtures. Also, a PT with a chiral amino acid side chain displayed moderate absorption band shifts and ICDs, depending upon the pH and the concentration of buffer.

Shifts in PT absorption bands due to changes in temperature result from a conformational transition from a coplanar, rodlike structure at lower temperatures to a nonplanar, coiled structure at elevated temperatures. For example, poly(3-(octyloxy)-4-methylthiophene) undergoes a color change from red–violet at 25 °C to pale yellow at 150 °C. An isosbestic point (a point where the absorbance curves at all temperatures overlap) indicates coexistence between two phases, which may exist on the same chain or on different chains. Not all thermochromic PTs exhibit an isosbestic point: highly regioregular poly(3-alkylthiophene)s (PATs) show a continuous blue-shift with increasing temperature if the side chains are short enough so that they do not melt and interconvert between crystalline and disordered phases at low temperatures.

Finally, PTs can exhibit absorption shifts due to application of electric potentials (electrochromism), or to introduction of alkali ions (ionochromism).

## 2.6 Regioregularity

The asymmetry of 3-substituted thiophenes results in three possible couplings when two monomers are linked between the 2- and the 5-positions. These couplings are:

- 2,5', or head–tail (HT), coupling
- 2,2', or head–head (HH), coupling
- 5,5', or tail–tail (TT), coupling

These three diads can be combined into four distinct triads, shown in Figure 2.9.

The triads are distinguishable by NMR spectroscopy, and the degree of regioregularity can be estimated by integration. Elsenbaumer *et al.* first noticed the effect of regioregularity on the properties of PTs. A regiorandom copolymer of 3-methylthiophene and 3-butylthiophene possessed a

conductivity of 50 S/cm, while a more regioregular copolymer with a 2:1 ratio of HT to HH couplings had a higher conductivity of 140 S/cm. Films of regioregular poly(3-(4-octylphenyl)thiophene) (POPT) with greater than 94% HT content possessed conductivities of 4 S/cm, compared with 0.4 S/cm for regioirregular POPT. PATs prepared using Rieke zinc formed “crystalline, flexible, and bronze-colored films with a metallic luster.” On the other hand, the corresponding regiorandom polymers produced “amorphous and orange-colored films. Comparison of the thermochromic properties of the Rieke PATs showed that, while the regioregular polymers showed strong thermochromic effects, the absorbance spectra of the regioirregular polymers did not change significantly at elevated temperatures. This was likely due to the formation of only weak and localized conformational defects.

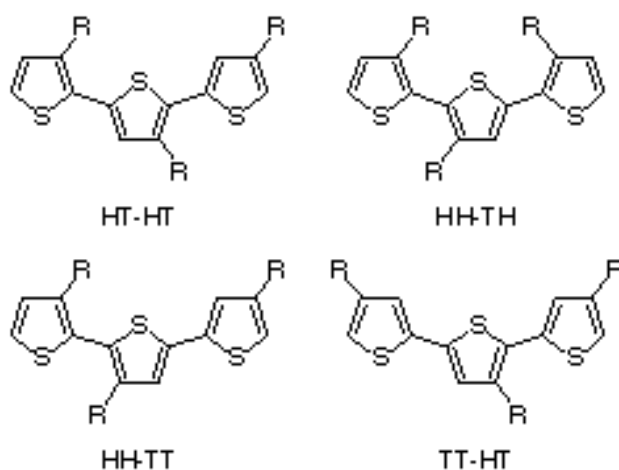


**Figure 2.9** The four possible triads resulting from coupling of 3-substituted thiophenes<sup>22</sup>.

Finally, Xu and Holdcroft demonstrated that the fluorescence absorption and emission maxima of poly(3-hexylthiophene)s occur at increasingly lower wavelengths (higher energy) with increasing HH dyad content. The difference between absorption and emission maxima, the Stokes shift, also increases with HH dyad content, which they attributed to greater relief from conformational strain in the first excited state.

## 2.7 Fullerene Electron Acceptors

Organic materials with appropriate properties, including conjugated polymers and small molecular compounds, can be used as electron donor materials in OPVs. Many organic compounds exhibited potential properties as electron acceptor material, but only a very few electron acceptor materials can

be used in highly efficient OPV devices. Fullerene and its derivatives are the most successful electron acceptor materials.

Fullerene C<sub>60</sub> has well-symmetric structure and exhibits good electron mobility, and as known, one molecule of C<sub>60</sub> can receive four electrons. Therefore, C<sub>60</sub> and its derivatives can be used as electron acceptor materials. In 1992, Sariciftci et al. first used C<sub>60</sub> as electron acceptor and discovered the photoinduced ultrafast electron transfer between electron donor and acceptor<sup>30</sup>. Although, C<sub>60</sub> can be dissolved in CB and DCB, it exhibits very limited solubility in most of the commonly used organic solvents. In order to improve its solubility and also to avoid severe phase separation of D/A blend, [6,6]-phenyl-C<sub>61</sub>-butyric acid methyl ester (PC<sub>60</sub>BM) was applied in OPVs. In the past decade, PC<sub>60</sub>BM and its corresponding C<sub>70</sub> derivative (PC<sub>70</sub>BM) have been dominantly used as acceptors in OPVs. In comparison with PC<sub>60</sub>BM, PC<sub>70</sub>BM possesses stronger absorption in visible range, and hence it attracted much interest recently. However, C<sub>70</sub> is much expensive than that of C<sub>60</sub> due to its tedious purification process, which limits its application. The molecular structures of PC<sub>60</sub>BM, PC<sub>70</sub>BM are shown in Fig. 2.10. PC<sub>60</sub>BM is crystalline dark-brown powder, and possesses good solubility in common organic solvents such as chloroform, toluene, and *o*-Dichlorobenzene<sup>31</sup>.

Absorption spectra of PC<sub>60</sub>BM and PC<sub>70</sub>BM are shown in Fig.2.11. It can be seen that both the two materials show strong absorption at ultraviolet region, from 200 to 400 nm, but PC<sub>70</sub>BM shows stronger absorption in visible region compared to PC<sub>60</sub>BM. Since, OPV devices using PC<sub>70</sub>BM as acceptor will harvest more sunlight, many OPVs using PC<sub>70</sub>BM as acceptor show bigger J<sub>sc</sub> and hence better PCEs than that of PC<sub>60</sub>BM-based devices.

The electrochemical properties and energy level of the fullerene derivatives is very important for OPVs. The open-circuit voltage (V<sub>oc</sub>) of OPVs is determined by the difference between the LUMO energy level of the fullerene acceptors and the HOMO energy level of the polymer donors<sup>32,33</sup>. Therefore, the LUMO energy level of the fullerene derivatives is a key parameter for the application of an acceptor to match with a polymer donor. LUMO level of electron donors or acceptors can be measured by cyclic voltammogram (CV) method. LUMO level of unsubstituted C<sub>60</sub> and PCBM

---

<sup>30</sup> Sariciftci NS, Smilowitz L, Heeger AJ, Wudl F (1992) Photoinduced electron transfer from a conducting polymer to buckminsterfullerene. *Science* 258:1474–1476.

<sup>31</sup> Hummelen JC, Knight BW, Lepeq F, Wudl F (1995) Preparation and characterization of fulleroid and methanofullerene derivatives. *J. Org. Chem.* 60:532–538. doi:10.1021/jo00108a012

<sup>32</sup> Brabec CJ, Sariciftci NS, Hummelen JC (2001) *Plastic solar cells*. origin of the open circuit voltage of plastic solar cells. *Adv Funct Mater* 11:15–26. doi:1616-301X/01/0510-0379

<sup>33</sup> Scharber MC, Wuhlbacher D, Koppe M (2006) Design rules for donors in bulk heterojunction solar cells—towards 10% energy-conversion efficiency. *Adv. Mater.* 18:789–794. doi:10.1002/adma.200501717

were ~ -4.2 and -4.0 eV, respectively<sup>34,35</sup>. Based on the difference of the LUMO levels of those two compounds, it is easy to conclude that LUMO level of C<sub>60</sub> can be elevated by adding the substituent. As discussed in the above section, higher LUMO level of electron acceptor materials would be helpful to get higher V<sub>oc</sub>, and for the purpose to get higher LUMO level, the bisadducts and multiadducts of fullerene were used in OPVs. For example, the LUMO level of bis-PCBM was 0.1–0.15 eV higher than that of PCBM, and when bis-PCBM was used as electron acceptor in P3HT-based OPV device, a V<sub>oc</sub> of 0.72 V was recorded, which was 0.12 V higher than the PCBM/P3HT-based devices<sup>36</sup>. Furthermore, multiadducts can also be used in OPVs, and higher V<sub>oc</sub> of the device can be realized. However, since the substituent of PCBM is inert for electron transport and the symmetric property of fullerene can be weakened, electron transport properties of the bis- or multiadducts were not as good as that of PCBM. Therefore, PC<sub>60</sub>BM and PC<sub>70</sub>BM are still among the best electron acceptors in OPVs.

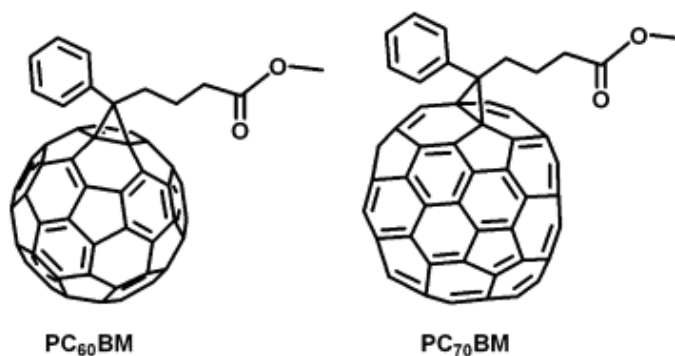


**Figure 2.10** Molecular structures of PC<sub>60</sub>BM and PC<sub>70</sub>BM<sup>37</sup>.

<sup>34</sup> Sariciftci NS, Braun D, Zhang C, Srdanov VI, Heeger AJ, Stucky G, Wudl F (1993) Semiconducting polymer buckminster fullerene heterojunctions: diodes, photodiodes, and photovoltaic cells. *Appl Phys Lett* 62:585–587. doi:10.1063/1.108863.

<sup>35</sup> He YJ, Li YF (2011) Fullerene derivative acceptors for high performance polymer solar cells. *Phys Chem Chem Phys* 13:1970–1983. doi:10.1021/ja103275u

<sup>36</sup> Lenes M, Shelton SW, Sieval AB, Kronholm DF, Hummelen JC, Blom PWM (2009) Electron trapping in higher adduct fullerene-based solar cells. *Adv Funct Mater* 19:3002–3007.

<sup>37</sup> [https://en.wikipedia.org/wiki/Phenyl-C61-butyric\\_acid\\_methyl\\_ester](https://en.wikipedia.org/wiki/Phenyl-C61-butyric_acid_methyl_ester)

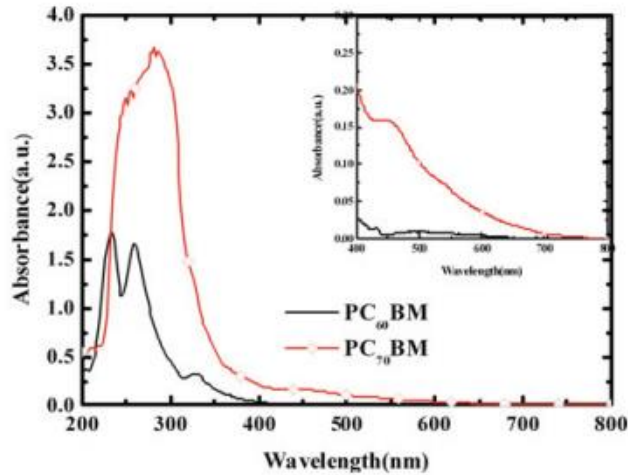


**Figure 2.11** Absorption spectra of PC<sub>60</sub>BM and PC<sub>70</sub>BM

## 2.8 Buffer Layers

### PEDOT:PSS

PEDOT:PSS or Poly(3,4-ethylenedioxythiophene) poly(styrenesulfonate) (fig. 2.12) is a polymer mixture of two ionomers. One component in this mixture is made up of sodium polystyrene sulfonate which is a sulfonated polystyrene. Part of the sulfonyl groups are deprotonated and carry a negative charge. The other component poly(3,4-ethylenedioxythiophene) or PEDOT is a conjugated polymer and carries positive charges and is based on polythiophene. Together the charged macromolecules form a macromolecular salt.

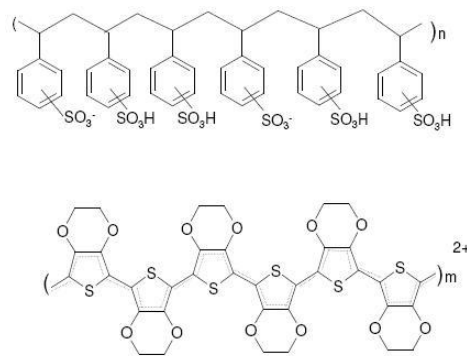


**Figure 2.12** Chemical composition of PEDOT:PSS. The upper region exhibits the oligomer PSS, and the lower region the oligomer PEDOT:PSS<sup>38</sup>

<sup>38</sup><http://www.google.com/patents/WO2012158125A1?cl=en>

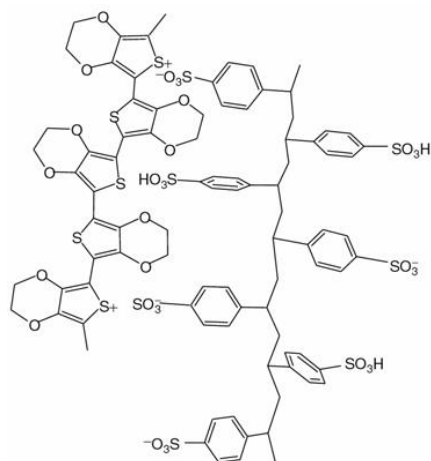


**Figure 2.13** Conformation of PEDOT:PSS

This compound is generally applied as a dispersion of gelled particles in water. A conductive layer is obtained by spreading the gelled particles dispersion layer on glass surface using spin coating and then thermally remove the humidity. Special PEDOT:PSS inks and formulations were developed for different coating and printing processes.

Water based PEDOT:PSS inks are mainly used in slot die coating, flexography, rotogravure and inkjet printing. If a high viscous paste and slow drying is required like in screen-printing processes PEDOT:PSS can also be supplied in high boiling solvents like propanediol. Dry PEDOT:PSS pellets can be produced with a freeze drying method which are redispersable in water and different solvents, for example ethanol to increase drying speed during printing. Finally, to overcome degradation to ultraviolet light and high temperature / humidity conditions PEDOT:PSS UV-stabilizers are available.

It is used as a transparent, conductive polymer with high ductility in different applications. These two materials exhibit high transparency in light of wavelength in the region 350-900 nm. The field of Organic Electronics is one of the fields that utilize this material exploiting these very interesting characteristics. Furthermore, is reducing the roughness of the ITO layer and optimize the electric contact with the active layer. Additionally, increases the work function of the positive electrode from 4.7-4.9 eV (that fluctuates the work function of ITO) to 5eV.

### **Titanium Suboxide (TiO<sub>x</sub>)**

Titanium suboxide (TiO<sub>x</sub>) is introduced as an electron selective layer between the active layer and bottom electrode in OPV devices. Moreover, is one of the most studied metal oxide semiconductors which have high electron mobility and high transparency in visible wavelength region. It also has excellent chemical and thermal stability, non-toxicity, it is inexpensive, and easy in

processing.  $\text{TiO}_x$  can be deposited from various methods namely sputtering, pulsed laser deposition, metal organic chemical vapor deposition, electrochemical deposition and spin coating. Among these methods, spin coating process is compatible with roll-to-roll processing at room temperature; it can be used at a low temperature, it is cost effective, simple in composition control, and able to provide good and smooth thin films.

## Chapter 3

### Bulk Heterojunction Organic Photovoltaics

This chapter introduces background information for this study. The first section outlines the concept of organic solar cells, detailing the device structure and operation mechanism. The last section explores the characteristics of a photovoltaic device. In this part, a brief perspective of the concept, mechanism and design considerations will be discussed.

#### 3.1 Device Structure and Operation Principles

The device structure of organic solar cells is different from traditional silicon wafer based solar cells. The photoactive layer is a blend of conjugated polymers as electron donors and fullerene derivatives as electron acceptors. This photoactive layer is sandwiched between two electrodes with proper work functions. Fig. 3.1 shows a schematic diagram of organic solar cell device structure. In this device architecture, the light is transmitted through the glass substrate. The device is built on a transparent substrate which may be flexible. The substrates are usually glass or polyethylene terephthalate (PET). The anode consists of a semitransparent oxide layer, usually indium tin oxide (ITO). Its role is to allow light to pass through, and to collect holes from the device. A layer of the conductive polymer poly (3,4-ethylenedioxy-thiophene)-poly (styrenesulfonate) (PEDOT:PSS) is applied between the anode and the photoactive layer. This thin layer is spin coated on top of the ITO surface. The PEDOT:PSS layer serves as a hole conducting layer and exciton blocker. It smooths the ITO surface, seals the active layer from oxygen, and prevents the anode material from diffusing into the active layer, which can lead to trap sites<sup>39</sup>. The light absorbing photoactive layer containing the donor and acceptor material is sandwiched between two electrodes. For laboratory devices, this layer is spin coated from a common solution which contains the polymer donor and fullerene acceptor suspended in an appropriate solvent or mixture of solvents. The cathode is usually aluminum, although calcium or silver is sometimes used. The function of the cathode is to collect electrons from the device. This layer is deposited by thermal evaporation.

---

<sup>39</sup> B.R. Saunders, Hybrid polymer/nanoparticle solar cells: Preparation, principles and challenges, *Journal of Colloid and Interface Science*, 369 (2012) 1-15.

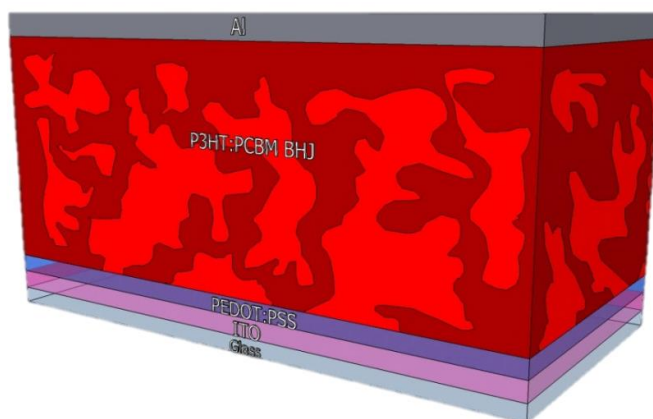


**Figure 3.1** Schematic diagram of organic solar cell device structure. The ITO and Al layer are used as anode and cathode, respectively.

### 3.2 Operation Principles

As the fundamental properties of organic semiconductors are different to that of their inorganic counterparts, the operation of OPV devices is different to that of silicon solar cells. In a silicon solar cell, incident photons break the covalent bonds, which form electron-hole pairs. Due to the crystalline nature of silicon, generation of charge carriers requires only a small force of interaction. Therefore, absorption in silicon leads to effectively free charge carriers. As a result of the low dielectric constant ( $\approx 3$ ) in semiconducting polymer materials, the coulombic forces of attraction between electrons and holes are very high<sup>40,41</sup>. This implies that unlike inorganic semiconductors, in which photo excitation generally forms a free electron and hole, excited states in semiconducting polymers form bound electron-hole pairs. This bound electron-hole pair is referred to as an ‘exciton’. A driving force is required to overcome this excitonic binding energy so that free charge carriers can be produced and transported throughout the device. In organic solar cells, excitons formed in the donor material can be dissociated at the donor-acceptor (D-A) interface. The force required to overcome the exciton binding energy is provided by the energy level offset of the lowest unoccupied molecular orbital (LUMO) of the donor and the LUMO of the acceptor material. Fig. 3.2 displays an energy band diagram of organic solar cells. This energy offset used to dissociate excitons is illustrated as  $\Delta E_{ES}$  Fig. 3.2, which is the excited state energy offset. In order to dissociate excitons formed in the acceptor material, the energy offset of the highest occupied molecular orbital (HOMO) of the acceptor and the HOMO of the donor

<sup>40</sup> W. Cai, X. Gong, Y. Cao, Polymer solar cells: Recent development and possible routes for improvement in the performance, *Solar Energy Materials and Solar Cells*, 94 (2010) 114-127.

<sup>41</sup> G. Garcia-Belmonte, A. Munar, E.M. Barea, J. Bisquert, I. Ugarte, R. Pacios, Charge carrier mobility and lifetime of organic bulk heterojunctions analyzed by impedance spectroscopy, *Organic Electronics*, 9 (2008) 847-851.

material is required. This energy offset used to dissociate excitons is illustrated as  $\Delta E_{GS}$  Fig. 3.2, which is the ground state energy offset. Excitonic dissociation due to these energy offsets occurs at the interface between the donor and acceptor phase, therefore, the arrangement of the two materials in the active layer is crucial for the successful operation of the device.

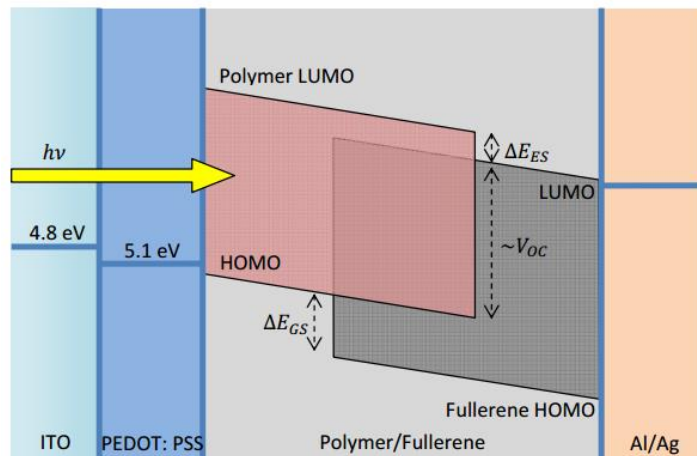


**Figure 3.2** Energy band diagram of donor-acceptor materials in bulkheterojunction organic solar cells.

Excitons can be created when photons are absorbed in the donor material. These excitons then can be dissociated at a D-A interface. Once separated, the electron can transfer to the acceptor material and be transported to the cathode for charge collection. The hole produced in the donor material travels throughout the polymer and is collected at the anode. This process is illustrated in Fig. 3.3 (a). The fullerene acceptor material may also contribute useful photocurrent. When light is absorbed in the acceptor material, an exciton is formed which must be dissociated by the energy offset of the donor HOMO level and the acceptor HOMO level. The hole is then transferred to the donor at an interface and is transported to the anode whilst the electron remains in the acceptor material and travels to the cathode for collection. This process is demonstrated in Fig. 3.3 (b).

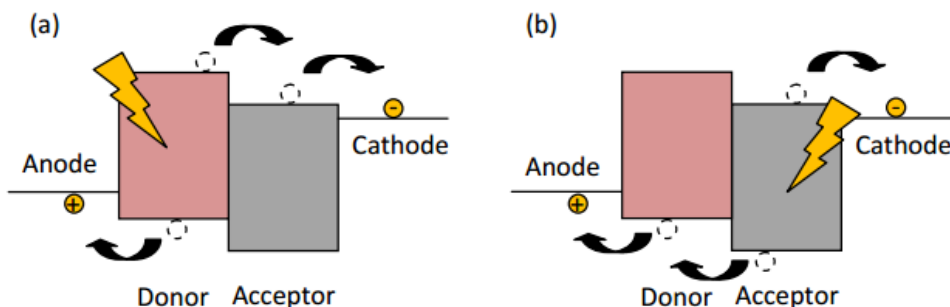


**Figure 3.3** Schematic energy band diagram displaying charge transfer for (a) photo generation in the donor, and (b) photo generation in the acceptor.

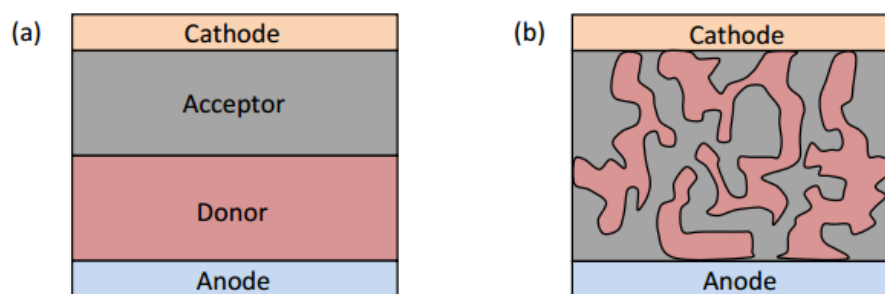


**Figure 3.4** Schematic diagrams of (a) bi-layer heterojunction and (b) bulkheterojunction photoactive layers.

The diffusion length of these bound electron hole pairs, or excitons is very small, in order of 10 nm<sup>42,43,44</sup>. This cause very poor electronic response in organic devices fabricated using a bi-layer structure, similar to that of a p-n junction silicon solar cell, as only photons absorbed within a diffusion length of the junction can produce free charge carriers. A more successful approach is to disperse the donor and acceptor material intimately throughout the active region, which significantly increases the interfacial area. Such a design is referred to as a bulk-heterojunction device structure<sup>45</sup>. Fig. 3.4 displays a cross sectional illustration of both a bi-layer and BHJ device structure. A device with a large dispersion of interfaces throughout the photoactive layer requires smaller exciton diffusion distances, and thus, a larger exciton dissociation yield is achieved. There exists a trade-off between increasing interfacial area via the intimate dispersion of phases and the creation of efficient conductive pathways through which free electrons and holes may be transported. The arrangement of donor and acceptor phase is thus crucial to device performance.

### 3.3 Characteristics of a photovoltaic device

#### 3.3.1 Current-Voltage Characteristics

The light absorbed in the junction creates electron-hole pairs whose concentration is proportional to number of absorbed photons with energies larger that the energy gap ( $E_g$ ) of the material. These

<sup>42</sup> N.S. Sariciftci, L. Smilowitz, A.J. Heeger, F. Wudl, Photoinduced Electron Transfer from a Conducting Polymer to Buckminsterfullerene, *Science*, 258 (1992) 1474-1476.

<sup>43</sup> C.J. Brabec, S. Gowrisanker, J.J.M. Halls, D. Laird, S. Jia, S.P. Williams, Polymer–Fullerene Bulk-Heterojunction Solar Cells, *Advanced Materials*, 22 (2010) 3839-3856.

<sup>44</sup> T.A. Bull, L.S.C. Pingree, S.A. Jenekhe, D.S. Ginger, C.K. Luscombe, The role of mesoscopic PCBM crystallites in solvent vapor annealed copolymer solar cells, *ACS Nano*, 3 (2009) 627-636.

<sup>45</sup> G. Yu, J. Gao, J.C. Hummelen, F. Wudl, A.J. Heeger, Polymer Photovoltaic Cells: Enhanced Efficiencies via a Network of Internal Donor-Acceptor Heterojunctions, *Science*, 270 (1995) 1789-1791.

electrons and holes are separated by the built-in electric field and are responsible for the production of an electric current,  $I_L$ , called the light-generated current. By neglecting the recombination effect in the depletion region and including the effect of generation in this region,  $I_L$  can be expressed as follows:

$$I_L = q A \int_0^w G(x) dx \quad (3.1)$$

Here  $G(x)$  is the generation rate of the electron-hole pairs,  $A$  is the device area, and  $w$  is the width of the depletion region. The direction (and hence, the sign) of the light-generated current is opposite to the direction of the dark current, which can be calculated by the following equation:

$$I_{dark} = I_s \left[ \exp\left(\frac{V}{nKR}\right) - 1 \right] \quad (3.2)$$

whereas  $I_s$  is the saturation current of the diode,  $q$  the elementary charge,  $n$  the diode ideality factor,  $k$  the Boltzmann constant and  $T$  the temperature. If the light generated current is larger than the dark current, the device acts as a current source, that is, as a source of electricity. Then, the total diode current under illumination is given by the Shockley equation:

$$I = I_L - I_s \left[ \exp\left(\frac{V}{nKT}\right) - 1 \right] \quad (3.3)$$

where, as customary for solar cells, we choose the sign of the light-generated current as positive. As can be seen from the above equation, setting  $I$  to zero, the ideal value of the open circuit voltage,  $V_{oc}$ , of a solar cell is given by:

$$V_{oc} = \frac{KT}{q} \ln\left(\frac{I_L}{I_s} + 1\right) \quad (3.4)$$

The built-in electric field separating the photogenerated electrons and holes can at most provide the built-in potential,  $V_{bi}$ . Hence, the built-in voltage gives the upper bound of the open circuit voltage. The effect of the parasitic series and shunt resistances,  $R_S$  and  $R_{SH}$  due to its bulk resistivity and presence of defects can be included in the Shockley equation as:

$$I = I_s \exp\left(\frac{q}{nKT}(V - IR_S)\right) - 1 + \frac{V - IR_S}{R_{SH}} - I_L \quad (3.5)$$

Figure 3.5 shows the equivalent circuit of p-n junction solar cell, in which the I-V curve of this circuit is described by the equation above. The circuit consists of the following three parts. A current source

$I_L$  that considers the light-generated current, a diode that accounts for the nonlinear voltage dependence and a shunt as well as a series resistor.

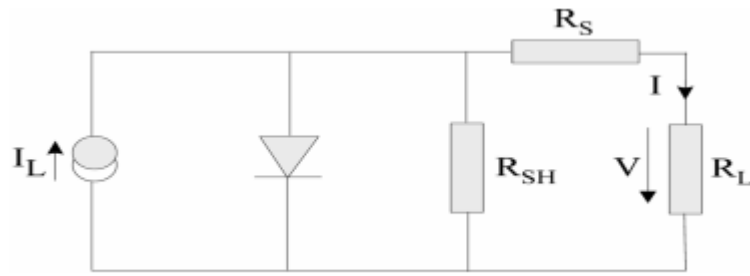


**Figure3. 5** Equivalent circuit of a p-n junction solar cell

The current source generates a current  $I_L$  up on illumination.  $I_L$  can be described as the number of free electron/hole pairs immediately after generation - before any recombination can take place. The series resistance  $R_S$  is due to the bulk resistance of the semiconductor material, the bulk resistance of the metallic contacts and the contact resistance between the metallic contacts and the semiconductor. The shunt resistance  $R_{SH}$  is caused by leakage across the p-n junction around the edge of the cell and in non-peripheral regions in the presence of defects and precipitates of foreign impurities in the junction region.

In conclusion, in the standard p-n junction solar cell, light absorption occurs via band gap excitation of electrons in the bulk of the semiconductor, charge separation in the internal electric field of the p-n junction and charge collection by transport of electrons and holes through the bulk of the semiconductor to the electrical contacts.

### 3.3.2 Solar cell efficiency

Respectively the net current density is given by

$$J(V) = J_{sc} - J_{dark} = J_{sc} - J_0(e^{\frac{qV}{k_bT}} - 1) \quad (3.6)$$

where  $J_s$  is the short-circuit current density and  $J_{dark}$  the current flowing under no illumination described by the ideal Shockley diode equation.

It is common to use I-V characteristics to indicate the efficiency of solar cells. The open-circuit voltage  $V_{oc}$  and the short-circuit current  $I_{sc}$  are determined by a given light level by the cell properties. The open circuit voltage can easily be derived from equation 3.5 given that there is no net current flowing:

$$V_{oc} = \frac{k_B T}{q} \ln\left(1 + \frac{J_{sc}}{J_0}\right) \quad (3.7)$$

An expression for the photocurrent density at short circuit can be given by:

$$J_{sc} = q \int_0^\infty \alpha(E) n_{coll}(E) [1 - R(E)] \Phi(E) d\lambda = q \int_0^\infty EQE(E) \Phi(E) d\lambda \quad (3.8)$$

where,  $\Phi(E)$  is the incident spectral photon flux density and  $R(E)$  the fraction of reflected photons as a function of the photon energy.  $\alpha(E)$  and  $\eta_{coll}(E)$  are the absorption coefficient and collection efficiency of the solar cell material, respectively. The product  $\alpha(E) \times \eta_{coll}(E) \times [1 - R(E)]$  is known as the external quantum efficiency (EQE) and reflects the probability of an incident photon generating one electron that is collected at the contacts. The EQE does not depend on the incident spectrum, hence it is therefore a key quantity in describing solar cell performance under different conditions.

The maximum power delivered to a load by a solar cell occurs when the product  $V \times I$  is at its maximum,  $P_m$ , i.e. when the solar cell operates at its maximum voltage ( $V_m$ ) and maximum current density ( $J_m$ ). The fraction of maximum power and the product of  $V_{oc}$  and  $J_{sc}$  is defined as the fill factor, FF (Figure 3.6), which further can be related to the efficiency,  $\eta$ .

$$\eta = \frac{J_m V_m}{P_s} = \frac{J_{sc} V_{oc} FF}{P_s} \quad (3.9)$$

where  $P_s$  is the incident light power input from the sun.

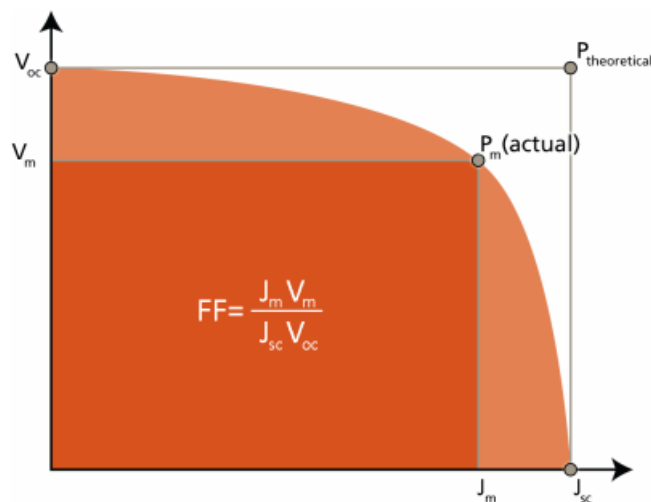


Figure 3. 6 Current-voltage characteristics and the fill factor of a solar cell

## Chapter 4

### Plasmonic Theory

#### 4.1 Surface Plasmons

This part gives an introduction to surface plasmons and their origin. The text is gradually angled towards utilizing surface plasmons to increase the efficiency of photovoltaics and examples of previous work is discussed in this context.

Metal nanoparticles have been used as decorative pigments since the time of the Romans when it was discovered that silver and gold particles in the nano range embedded in dielectric surroundings exhibit unique optical properties<sup>46</sup>. The most famous example is maybe the Lycurgus Cup from the 4th century AD. Analysis have shown that the glass contains small amounts of nanoparticles of silver and gold approximately 70nm in diameter. The cup appears green in the reflected light and looks red when a light is shone from inside and is transmitted through the glass as seen in figure 4.1. This is due to the excitation of surface plasmon modes on the gold and silver particles embedded in it.



**Figure 4. 1** The Roman Lycurgus cup from the 4th century AD in (a) reflected light and (b) transmitted light<sup>47</sup>

<sup>46</sup> Luis M. Liz-Marzán. Nanometals: Formation and color. *Materials Today*, 7:26–31, 2004. 29, 61, 114, 115

<sup>47</sup> Tim Kelf. Surface plasmon polaritons. 7, 29

The energy of the surface plasmon resonance depends on the dielectric constants of both the nanoparticle and the surrounding medium. Mie was the first to explain the red color of colloidal gold nanoparticles in 1908, after Michael Faraday had stated in 1831 that particle size was the color-determining factor<sup>48,49</sup>. Mie's biggest discovery was that materials which real part of the dielectric function was negative, showed an anomalous peak in the absorption spectrum in form of small particles<sup>50</sup>.

The reduction of the dimensions of materials has pronounced effects on the optical properties. The reason for this behavior can generally be ascribed two different phenomena. One is due to the quantum confinement, i.e. increased energy level spacing as the system becomes more confined, and the other is related to the surface plasmon resonance.

Metallic photonic materials demonstrate unique properties due to the existence of electro-magnetic surface waves known as surface plasmons. Surface plasmons are set to become part of the photonics revolution in which the interaction between light and matter is controlled by producing patterned structures that are periodic on the scale of the wavelength of light. Surface plasmons open up a wealth of new possibilities for photonics because they allow the concentration and propagation of light below the usual resolution limit, thus opening up such possibilities as sub-wavelength optical components.

#### **4.1.1 Basic introduction to plasmons**

A plasma is a medium with equal concentrations of positive and negative charges, of which at least one charge type is mobile. Plasmons are quanta of plasma oscillations. Plasmons are particularly related to materials that show metallic properties, i.e. that have free electrons. Consider a material of this kind in equilibrium conditions with its mobile negative charges stabilized by fixed positive ions (cations). This is what is known as the jellium model in metals. Now disturbing these ideal conditions by introducing an external electromagnetic field will give rise to a non-uniform charge distribution and hence an internal field as shown in figure 4.2. The negative charges will gain momentum from this field, but since they are simultaneously pulled back towards the positive charges and we assume they are not energetic enough to escape the electric field created by the nuclei, they end up oscillating about

---

<sup>48</sup>Kenneth Klabunde. *Nanoscale Materials in Chemistry. Wiley-Interscience, first edition, 2001. 29*

<sup>49</sup> Guozhong Cao. *Nanostructures & Nanomaterials - Synthesis, Properties & Applications. Imperial College Press, 57 Shelton Street, London, UK, 2004. 29*

<sup>50</sup> Uwe Kreibitz and Michael Volmer. *Optical properties of metal clusters. Springer, 1995. 29, 30, 37*

the positive charge distribution. This oscillation of mobile electrons from the conduction band is called a plasmon.

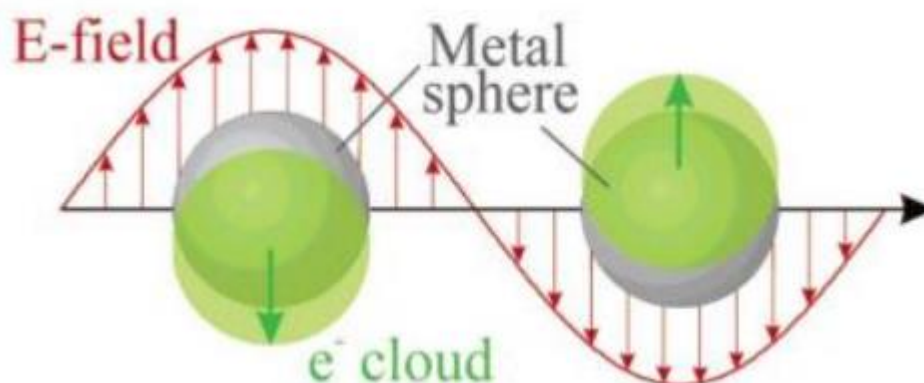


**Figure 4.2** Schematic of the plasmon oscillation of a sphere, showing the displacement of the conduction electrons relative to the nuclei<sup>51</sup>

#### 4.1.2 Bulk and surface plasmons

Most often one distinguishes only between plasmons that exist in the bulk and the ones that exist on the surface of materials. It is however, important to separate the surface-bound plasmons according to the geometry of their surroundings.

##### Bulk plasmons

When considering plasmons that exist in the bulk, one can think of longitudinal oscillation of free electrons in an infinite metallic medium. The frequency of this collective oscillation is called the plasma frequency,  $\omega_p$ , and is given by<sup>52</sup>

$$\omega_p = \frac{\sqrt{ne^2}}{e_0 m_e} \quad (4.1)$$

where  $n$ ,  $e$  and  $m$  are the electron density, electronic charge and mass, respectively, and  $\epsilon_0$  the permittivity of free space. The bulk plasmons do not contribute in the same way as surface plasmons to the interesting optical properties of solids. This is because the probability of plasmon excitation in the bulk of a material is small since the energy of visible light provides too little momentum to the electrons in the crystal. The conduction electrons will thus simply relax back to equilibrium conditions

<sup>51</sup> K. L. Kelly, E. Coronado, L. L. Zhao, and G. C. Schatz. The optical properties of metal nanoparticles: The influence of size, shape, and dielectric environment. *J Phys Chem B*, 107:668–677, 2003. 7, 30, 36

<sup>52</sup> Charles Kittel. *Introduction to Solid State Physics*. John Wiley and Sons, New York, Chichester, seventh edition, December 1996. 30

when using light of optical wavelengths. Hence, electron or x-ray spectroscopy is needed for bulk plasmon characterization<sup>53</sup>.

### **Surface plasmon polaritons (SPPs)**

Because of the long-range nature of the organizing forces in a plasma oscillation, it is reasonable to expect that for sufficiently small systems the electrons will sense the presence of the boundaries and modify their collective behavior accordingly. Indeed, surface plasmons are possible in thin films, propagating along the interface of a conductor and a dielectric medium where the real part of the dielectric function,  $\epsilon$ , has opposite signs<sup>54</sup>. Although analogous to bulk plasmons, these plasmons are restricted to the mobile electrons of surfaces. When the excitation of these plasmons is combined with that of a photon, a surface plasmon polariton is created. Two important properties of SPPs must be considered related to the photon-excitation of plasmons: First, there is a momentum mismatch between the SPP and the exciting photon. Second, the electromagnetic field caused by the oscillations has its maximum at the surface and will decay exponentially with the distance to the surface<sup>55,56</sup>, this is said to be evanescent or near-field. Consequently, special techniques must be used to couple the light into plasmons and we can say that SPPs are non-radiative waves on the surface.

---

<sup>53</sup> Brian J. Soller, Howard R. Stuart, and Dennis G. Hall. Energy transfer at optical frequencies to silicon-on-insulator structures. *Opt. Lett.*, 26(18):1421–1423, 2001. 30, 42

<sup>54</sup> Harry A. Atwater and Albert Polman. The optical properties of metal nanoparticles: The influence of size, shape, and dielectric environment. *MRS Bulletin*, 30(3):385–389, 2005. 31

<sup>55</sup> Harry A. Atwater and Albert Polman. The optical properties of metal nanoparticles: The influence of size, shape, and dielectric environment. *MRS Bulletin*, 30(3):385–389, 2005. 31

<sup>56</sup> Luis Prill Sempere. Surface plasmon polaritons (spp) and their use in subwave-length optics. Term paper for *Physics of Nanostructures*. 31, 32

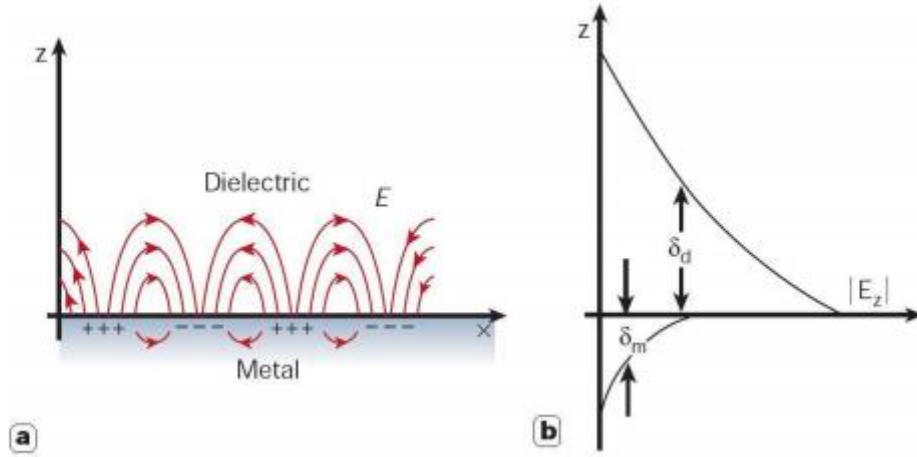


**Figure 4. 3** The electric field perpendicular to the surface is enhanced near the surface and decays exponentially with distance away from it (a). This field is said to be evanescent, reflecting the bound surface plasmon modes and prevents power from propagating away from the surface (b)

At flat metal surfaces, excitations can only be achieved in the metal-dielectric interface by the use of special geometries that provides the required wavevector,  $k_{sp}$ , matching of the surface wave with that of the light producing it (e.g. Kretschmann<sup>57</sup> or Otto<sup>58</sup> configuration). (3 principles: prism and total internal reflection; scattering from topological defects like small holes in a thin film; periodic corrugations in the metal's surface).

SPPs have higher  $k$ -values and thus higher momentum ( $hk$ ) than light of the same frequency. This will give rise to a strong resonant interaction between oscillating electrons and the electro-magnetic field caused by the light, which again results in unique optical properties. This can be understood by looking at the surface plasmon dispersion relation derived from the Maxwell equations under appropriate boundary conditions:

$$k_{sp} = k_0 \sqrt{\frac{\epsilon_m \epsilon_d}{\epsilon_m + \epsilon_d}} \quad (4.2)$$

where the free space vector is  $k_0 = w/c$  and  $\epsilon_m$  and  $\epsilon_d$  the dielectric constants of the metal and the dielectric medium, respectively. The dielectric constant of the metal is frequency dependant and given by the Drude formula<sup>59</sup> :

<sup>57</sup> Paras N. Prasad. Nanophotonics. Wiley-Interscience, 2004. 31

<sup>58</sup> Andreas Otto. Excitation of nonradiative surface plasma waves in silver by the method of frutrated total efection. Zeitschrift für Physik A, 216:398–410, 1968.31

<sup>59</sup> Craig F. Bohren and Donald R. Huffman. Absorption and scattering of light by small particles. John Wiley and Sons, Inc., Weinheim, Germany, 1983. 7, 31, 33, 34, 35, 36, 37, 73, 109, 115, 119

$$\varepsilon(\omega) = 1 - \frac{\omega_p^2}{(\omega^2 + i\gamma\omega)} \quad (4.3)$$

where  $\omega_p$  is given by eq (4.1) and is the collision frequency of the electrons usually termed the damping coefficient. Then, to get the surface plasmon  $k$  vector larger than that of light, the square root in equation 4.2 must be larger than 1. This is obtained when  $\varepsilon_m$  and  $\varepsilon_d$  have different signs. A metal will directly satisfy this criterion since its  $\varepsilon_m$  is negative and complex. As a result of the higher momentum of SPPs than light, power will be prevented from propagating away from the surface. This is the fundamental principle behind surface plasmon waveguiding<sup>60</sup>.

The frequency,  $\omega_{sp}$ , of a surface plasmon on the flat surface of a nearly infinite piece of metal, can easily be determined from the frequency of a bulk plasmon in a metal,  $\omega_p$ , because it corresponds to:  $\text{Re } \varepsilon_m(\omega_{sp}) = -\varepsilon_d$ , where  $\varepsilon_d > 0$  is the dielectric constant of the dielectric medium. By solving the equations given for the dispersion relationship and the dielectric function, the maximum frequency of the surface plasmon is found to be:

$$\omega_{sp} = \frac{\omega_p}{\sqrt{1 + \varepsilon_d}} = \frac{\omega_p}{\sqrt{2}} \quad (4.4)$$

for a metal with free electrons in contact with a vacuum medium. Once light has excited a surface plasmon mode on a flat metal surface it will propagate but also gradually degrade because of losses arising from absorption in the metal. The degree of degradation depends on the dielectric function of the metal at the frequency at which the SP oscillates. Silver, which is the metal with the lowest loss in the visible spectrum, has typically propagation distances in the range of 10-100 $\mu\text{m}$ , and up to 1mm at wavelengths above 1.5 $\mu\text{m}$ <sup>61</sup>. Most often, the surface plasmon resonance frequency  $\omega_{sp}$  lies in the UV (ultra-violet) region for metals and the IR (infra-red) region for heavily doped semiconductors.

### Localized surface plasmons (LSPs)

Consider again a flat metal surface. Now introducing curvature or roughness to this surface, and hence more confinement to the geometries that the surface plasmons are bound to, will give rise to a different kind of plasmon excitation. While SPPs are propagating surface modes along the interface between a thin, flat metallic film and a dielectric, localised surface plasmons (LSPs) are confined to

---

<sup>60</sup> Stefan A. Maier, Paul E. Barclay, Thomas J. Johnson, Michelle D. Friedman, and Oskar Painter. Low-loss fiber accessible plasmon waveguide for planar energy guiding and sensing. Appl. Phys. Lett., 84(25):3990–3992, 2004.

32

<sup>61</sup> William L. Barnes, Alain Dereux, and Thomas W. Ebbesen. Surface plasmon sub-wavelength optics. Nature, 424:824 – 830, 2003. 7, 31, 32

curved metal objects, such as small metal particles or voids in metallic structures. These LSPs are characterized by frequencies which depend upon the size, shape and dielectric constant of the object to which the surface plasmon is confined. As described earlier, SPP modes can only be excited if both the frequency and wavevector of the exciting light match that of the SPP. In contrast, LSPs can be excited resonantly with light of appropriate frequency (and polarization), independent of the excitation light wavevector<sup>62</sup>.

Localized surface plasmons are assigned not only to small particles, but also to features on metal surfaces. For the LSPs to be excited, the geometry to which they are confined needs to be finite and within a certain size. Variations in size and shape will affect the intensity as well as the peak-shift of the scattering produced by the particles or surface-features. The treatments of LSPs are only valid if the characteristic dimension of the system is much smaller than the wavelength of the exciting light. By considering a small metal particle, the positive charges can be assumed to be fixed while the negative charges are moving under the influence of an external field. This external field will now give rise to a displacement of the positive and negative charges, as described introductory and shown in figure 4.2. Treating the electric field of the incoming light as constant, the problem can be treated with electrostatics rather than electrodynamics, the approximation is said to be quasistatic. This electric field,  $\sim E(t)$ , on a nanoparticle with dimensions much smaller than the wavelength of the light creating it and with a dielectric constant  $\epsilon_m$ , induces a dipole moment<sup>63</sup>.

$$\vec{p}(t) = \epsilon_0 \epsilon_m a \vec{E}(t) \quad (4.5)$$

where  $\epsilon_0$  and  $\epsilon_m$  is the dielectric constant of vacuum and is the polarizability of the particle. The internal field is given by<sup>64</sup>

$$E_i = E_0 \frac{3\epsilon_d}{\epsilon_m + 2\epsilon_d} \quad (4.6)$$

where  $\epsilon_d$  is the relative permittivity of the dielectric medium and  $\epsilon_m$  is the complex relative permittivity of the particle given by  $\epsilon_m = \epsilon'_m + i\epsilon''_m$ . This is again related to the index of refraction  $N = n + ik$  by  $\epsilon'_m = n^2 - k^2$  and  $\epsilon''_m = 2nk$ . The real term describes the polarizability, whereas

---

<sup>62</sup> Anatoly V Zayats and Igor I Smolyaninov. Near-field photonics: surface plasmon polaritons and localized surface plasmons. *Journal of Optics A: Pure and Applied Optics*, 5(4):S16, 2003. 32, 33

<sup>63</sup> David Blazquez Sanchez. The Surface Plasmon Resonance of Supported Noble Metal Nanoparticles: Characterization, Laser Tailoring, and SERS Application. PhD thesis, The University of Kassel, Germany, 2007. 33

<sup>64</sup> Leung Tsang, Jin Au Kong, and Kung-Hau Ding. Scattering of electromagnetic waves: Theories and applications. Wiley-Interscience, 2000. 33

the imaginary term is related to absorption and thereby dissipation of energy in the particle<sup>57</sup>. In fact, the imaginary term can be directly related to the absorption coefficient by  $\alpha = 4\pi k/\lambda$ <sup>65</sup>. Materials which have negative values for the real part of the dielectric function have high reflectance and a small dissipation (i.e.  $\epsilon'' = \epsilon' \ll 1$ ). Metals exhibit this property below its bulk plasma frequency and this is the reason for the high optical reflectivity of metals<sup>66</sup>. The polarization,  $\alpha$ , of a sphere can be found by

$$\alpha = 3V\epsilon_0 \frac{\epsilon_m - \epsilon_d}{\epsilon_m + 2\epsilon_d} \quad (4.7)$$

as given by Mie. Here, the dielectric constants are as given before, and  $r$  and  $V$  are the radius and volume of the particle. The polarizability is largest when the denominator in equation 2.2.7 equals to zero or is as small as possible, i.e. at the frequency where  $\epsilon_m = -2\epsilon_d$  or  $|\epsilon_m + 2\epsilon_d|$  is at its minimum. The solution to this is the frequency at which  $\epsilon' = 2\epsilon_m$  and  $\epsilon'' = 0$ , which is sometimes termed the *Frölich frequency*<sup>67</sup>. From equation 4.6 we see the same strong interaction of the spheres with the incident field at the same frequency. This frequency corresponds to the surface plasmon resonance, and is given by:

$$\omega_{lsp} = \frac{\omega_p}{\sqrt{1+2\epsilon_d}} \quad (4.8)$$

For a metal sphere in vacuum where  $\epsilon_d = 1$ ,  $\omega_{sp} = \omega_p/\sqrt{3}$ . In the case of voids in the bulk of a metal, the LSP frequencies of a particle and a void of the same shape can be estimated from each other as they are related like<sup>19</sup>

$$\omega_{particle}^2 + \omega_{void}^2 = \omega_p^2 \quad (4.9)$$

Since LSPs are confined to a particle, this can result in selective photon absorption, scattering and a significant enhancement of the electromagnetic field in the particle-vicinity when the volume to which it is localized gets very small. Enhancements of 100-10.000 times the incident field has been observed in the vicinity of small metal nanoparticles and with a spatial resolution in the order of 10-50nm. The spectrum of LSPs associated with an ensemble of particles depends significantly on the size and shape of these particles, the distance between them, and also the dielectric properties of the surrounding substrate and medium<sup>19</sup>.

<sup>65</sup> Martin Green. Silicon Solar Cells - Advanced Principles & Practice. Centre for Photovoltaic Devices and Systems, UNSW, Sydney, N.S.W. 2052m, Australia, 1995. 33

<sup>66</sup> Supriya Pillai. Surface plasmons for enhanced thin-film silicon solar cells and light emitting diodes. PhD thesis, School of photovoltaic and renewable energy engineering, University of New South Wales, Australia, 2007. 8, 33, 51, 52

<sup>67</sup> Craig F. Bohren and Donald R. Huffman. Absorption and scattering of light by small particles. John Wiley and Sons, Inc., Weinheim, Germany, 1983. 7, 31, 33, 34, 35, 36, 37, 73, 109, 115, 119

Most often one uses a dipole approximation where the electrons are driven to the surface of the particle as shown in figure 4.2. This is however, only applicable to very small particles, as higher order multipoles will influence the charge distribution when the particles grow bigger<sup>19</sup>. This will be explained in further details when dealing with the size and shape of the particles.

### 4.1.3 Extinction by metallic nanoparticles

Extinction is the sum of absorption and scattering of the incident light by the metallic nanoparticles. Ideally we want scattering processes to provide for all of the extinction, as the energy from the light is merely lost into heat when absorbed by the particles<sup>68</sup>. When the incident radiation is in the frequency range near that of the surface plasmon resonance, the polarizability of the particles increases and the field lines are more strongly affected in a larger distance from the particle. As a consequence, light may interact with the particle over a cross-sectional area larger than the geometrical cross-section of the particle. These cross-sections can be defined as follows<sup>69</sup>

$$C_{abs} = \frac{2\pi}{\lambda} \text{Im}(a) \quad (4.10)$$

$$C_{scat} = \frac{1}{6\pi} \left(\frac{2\pi}{\lambda}\right)^4 |\alpha|^2 \quad (4.11)$$

Where  $\alpha$  is here the polarizability of the particle, given by

$$\alpha = 3V \frac{\epsilon_m - \epsilon_d}{\epsilon_m + 2\epsilon_d} \quad (4.12)$$

---

<sup>68</sup> R. H. Ritchie. Plasma losses by fast electrons in thin films. Phys. Rev., 106(5):874–881, Jun 1957. 34

<sup>69</sup> R. H. Ritchie. Plasma losses by fast electrons in thin films. Phys. Rev., 106(5):874–881, Jun 1957. 34

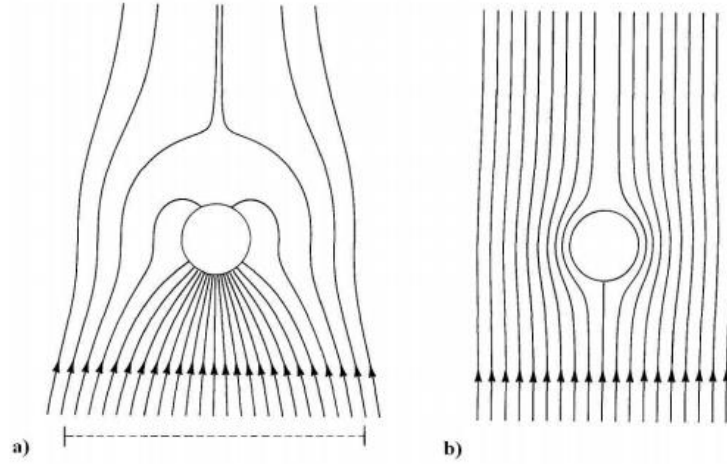


**Figure 4. 4** Field lines around a small aluminium sphere illuminated by light of energy 8.8eV (a) and 5eV (b). The dashed, horizontal line represents the effective radius of the sphere for absorption of light <sup>29</sup>

Figure 4.4 shows the field lines of the total pointing vector (shows the magnitude and direction of energy flow in an electromagnetic field) around a small Al sphere illuminated by light of energy 8.8 eV and 5 eV, respectively. The result is an absorption cross section 18 times greater than the geometrical cross-section of the particle in the case of 8.8 eV, which is the characteristic energy of the surface plasmon in aluminum.

A scattering efficiency,  $Q_{scat}$  can also be defined as the ratio between the scattering and geometric cross-section. This is a useful term which describes the contribution to cross-sections related to the excitation of surface plasmons.

$$Q_{scat} = \frac{C_{sca}}{\pi r^2} = \frac{8}{9} r^4 \left( \frac{2\pi}{\lambda} \right)^4 \left| \frac{\epsilon_m - \epsilon_d}{\epsilon_m + 2\epsilon_d} \right|^2 \quad (4.13)$$

For example, by considering Ag nanoparticles deposited on a substrate having a  $Q \approx 10$  at resonance, the substrate needs only to be covered with a 10% areal density to have the possibility to fully absorb and scatter the incident light of that frequency<sup>70</sup>.

Another popular term is the radiative efficiency  $Q_{rad}$ , which is the scattering efficiency divided by the total extinction. It is beneficial for understanding the relative significance of the processes for e.g. certain particle sizes and at certain wavelengths.

<sup>70</sup> K. R. Catchpole and A. Polman. Plasmonic solar cells. Opt. Express, 16(26):21793–21800, 2008. 8, 15, 35, 37, 41, 42, 61, 119

From the strong dependence upon the radius of the particle, it seems like the scattering efficiency will increase with increasing particle size. This is indeed true for particles within a certain order of size. Based on photocurrent measurements from metal islands of different sizes on SOI (silicon-on-insulator) devices, a strong size-dependance was observed on the scattering intensity of the particles<sup>71</sup>. Larger nanoparticles have larger polarizabilities and likewise higher radiative efficiencies, both factors increasing the effective cross-section and thereby the particle interaction with the incident light. For very small metallic particles, absorption dominates the extinction processes in the material. As the particles grow larger, scattering processes will prevail until it reaches a certain size where the external electric field is no longer able to polarize the whole particle homogeneously. The result is the excitation of higher order plasmon modes (quadrupole, octopole) and radiation damping which will constitute important corrections to the quasi-static expressions given for the polarizability and cross-sections. For particles larger than the wavelength, a large fraction of the light will be reflected rather than excite plasmons<sup>72</sup>.

#### **4.1.4 Tuning the plasmon resonance**

One big advantage of metal nanoparticles is that their optical properties depend strongly upon the material, size and shape of the particles, which in turn makes it possible to tune the resonance peak according to area of application. Apart from the characteristics of the single particles, the environment in which the particles are dispersed is also of relevance to the optical properties. The distance between neighbouring particles as well as the refractive index of the surrounding medium has been shown to influence the spectral properties, as will be described below.

#### **Choice of material**

The first discussions on surface plasmon modes concerned colloidal silver and gold, but in the more recent years many observations have been made on surface modes in various metals and metal-like materials. As the surface plasmon resonance frequency in a particle mainly depends on the density of free electrons in the particle, the resonance can be shifted by changing the material. The SPR frequency red-shifts with decreasing free electrons density, leading to a SPR in the UV region for aluminium (~8.8eV) and silver (~4eV) [15], whereas it is located in the visible part of the spectrum for copper (~2.1eV) and gold (~2.5eV). Experiments that have been done on making alloys of silver

---

<sup>71</sup> Howard R. Stuart and Dennis G. Hall. Enhanced dipole-dipole interaction between elementary radiators near a surface. *Phys. Rev. Lett.*, 80(25):5663–5666, Jun 1998.35, 40, 119

<sup>72</sup> Craig F. Bohren and Donald R. Huffman. *Absorption and scattering of light by small particles*. John Wiley and Sons, Inc., Weinheim, Germany, 1983. 7, 31, 33,34, 35, 36, 37, 73, 109, 115, 119

and gold show a linear dependence of the composition on the SPR frequency and may be a convenient way of controlling the resonances in between those of the pure materials<sup>73,74</sup>.

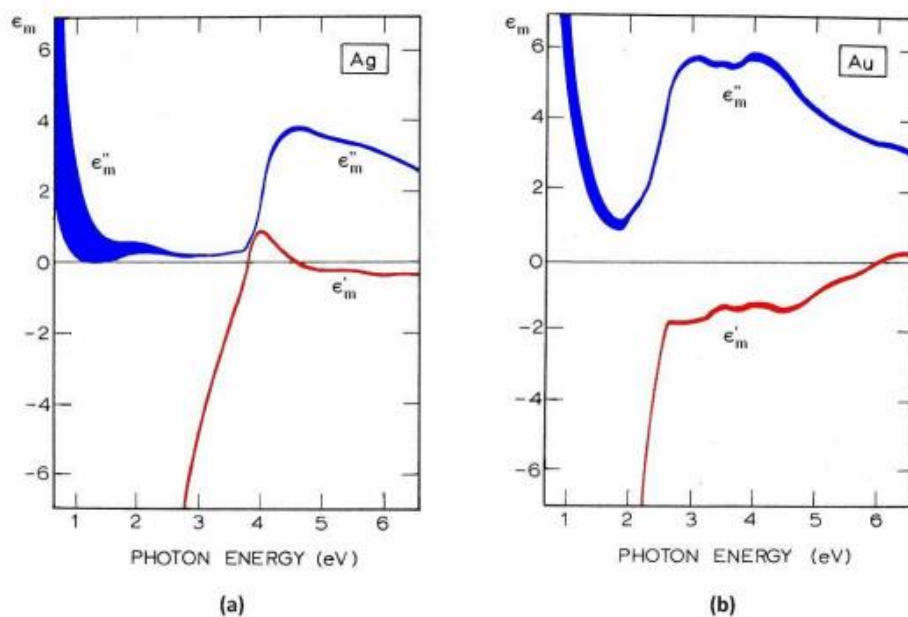


**Figure 4.5** The dielectric permittivity of silver and gold, showing the real part ( $\epsilon'_m$ ) with a red line and the imaginary part ( $\epsilon''_m$ ) with a blue line. The width of the curves represents the instrumental error of the measurements.<sup>75</sup>

Figure 4.5 shows the dielectric constants of silver and gold. Spherical silver and aluminium particles have intense surface plasmon absorption peaks because  $\epsilon''$  is small at the frequency at which  $\epsilon' = 2$ , whereas gold and copper are more absorbing because of much greater values of  $\epsilon''$ . This behaviour can be seen for silver and gold in the figure for photon energies most interesting for solar cell applications (1.12eV-  $\approx$  4eV). As pointed out earlier,  $\epsilon''$ , which is the imaginary term of the dielectric function, is related to the absorption and hence the dissipation of heat into the metal. Silver, due to its lower  $\epsilon''$ -value and lower cost is thus a better choice than gold, although possibly negative oxidation effects must be taken care of that are not present in gold<sup>76,77</sup>. As for copper it is cheaper than silver but the absorption is comparable to that of gold (has a high value for  $\epsilon''$ ) and there is also a big

<sup>73</sup> Kazutaka Baba, Toshiaki Okuno, and Mitsunobu Miyagi. Silver-gold compound metal island films prepared by using a two-step evaporation method. *Appl. Phys.Lett*, 62(5):437–439, 1993. 35

<sup>74</sup> S. Link, Z. L. Wang, and M. A. El-Sayed. Alloy formation of gold-silver nanoparticles and the dependence of the plasmon absorption on their composition. *The Journal of Physical Chemistry B*, 103(18):3529–3533, 1999. 35

<sup>75</sup> . B. Johnson and R. W. Christy. Optical constants of the noble metals. *Phys. Rev.* B, 6(12):4370–4379, Dec 1972. 7, 36, 73

<sup>76</sup> D. J. Nash and J. R. Sambles. Surface plasmon-polariton study of the optical di-electric function of silver. *Journal of Modern Optics*, 43:81–91, 1996. 35, 36

<sup>77</sup> M. D. McMahon, H. M. Meyer R. Lopez, L. C. Feldman, and R. F. Haglund. Rapid tarnishing of silver nanoparticles in ambient laboratory air. *Applied Physics B: Lasers and Optics*, 80(7):915–921, 2005. 36, 77, 116

concern regarding oxidation. Aluminium being cheaper, more abundant and having a small dissipation of heat seems like an even better alternative than silver for surface plasmon applications. Experiments have shown that nanodisks of Al support strong, long-lived excitations of localized surface plasmons that have good possibilities for tuning over the entire spectral range interesting for solar applications. However, an interband transition at around 1.5eV related to the specific band structure of Al gives rise to an enhanced instability of the LSPR at this frequency<sup>78</sup> and hence can be a problem regarding the use of aluminium in solar cell applications.

### **Size and shape of the particles**

The decrease of the particle size induces limitations to the mean free path of the electrons due to the particle boundaries<sup>79</sup>. This will result in a sharpening of the absorption peak, and as the particles grow larger they generally show a stronger resonance peak because of the increased extinction cross-section, but no significant shift of the resonance frequency is observed<sup>80</sup>. When the particles grow beyond a certain diameter depending on the dielectric properties of the material, the resonance peak will broaden and shift to lower energies because of retardation effects and the excitation of higher order multipoles. These multipole excitations are observed as shoulders or distinct peaks in absorption spectra<sup>81,82,83</sup>.

Experiments that have been done on nanosphere lithography with silver nanoparticles show that the normalized extinction can be tuned all the way from near UV, through the visible spectrum and far into the IR region (4000nm) by varying the size and shape of the particles<sup>84,85</sup>. The red-shift

---

<sup>78</sup> Langhammer C., Schwind M., Kasemo B., and Zoric´ I. Localized surface plasmon resonances in aluminum nanodisks. *Nano Letters*, 8(5):1461–1471, 2008. 36

<sup>79</sup> U. Kreibig and C. v. Fragstein. The limitation of electron mean free path in small silver particles. *Zeitschrift für Physik A Hadrons and Nuclei*, 224(4):307–323, 1969. 36

<sup>80</sup> F. J. Beck and K. R. Catchpole. Red-shifting the surface plasmon resonance of silver nanoparticles for light trapping in solar cells. In *Mater. Res. Soc. Symp. Proc.* Vol., volume 1101. Materials Research Society conference, San Francisco, 2008.36, 37, 40

<sup>81</sup> K. L. Kelly, E. Coronado, L. L. Zhao, and G. C. Schatz. The optical properties of metal nanoparticles: The influence of size, shape, and dielectric environment. *J Phys Chem B*, 107:668–677, 2003. 7, 30, 36

<sup>82</sup> Jack J. Mock, David R. Smith, and Sheldon Schultz. Local refractive index dependence of plasmon resonance spectra from individual nanoparticles. *Nano Letters*,3(4):485–491, 2003. 36, 37

<sup>83</sup> Johanna Jacoba Penninkhof. Tunable plasmon resonances in anisotropic metal nanostructures. PhD thesis, Utrecht University, Netherlands, 2006. 33, 36, 37, 38, 41

<sup>84</sup> A Haes, J. Haynes, C. L. McFarland, A. D. Schatz, G. C. Van Duyne, and R. P. Zou. Plasmonic materials for surface-enhanced sensing and spectroscopy. *MRS Bulletin - Materials research society*, 30(5):368 – 375, 2005. 33, 36

and broadening of the absorption peak would generally be an advantage for solar cell applications, since light trapping should happen over a large wavelength range and most importantly at long wavelengths where silicon absorbs poorly. Even though an increase of the particle size leads to a larger absolute scattering cross-section, it is in fact lowered when normalized by size.

Surface plasmons are unevenly distributed in non-spherical metallic nanoparticles and this is clear from the absorption spectra of such particles. Generally, different absorption bands correspond to oscillations along axes of different scales in the particles, each having its own polarizability. Besides spheres, silver nanoparticles have been synthesized in a wide variety of shapes including cubes, oblates, prisms, ellipsoids, rods and wires to name a few<sup>86,87,88,89</sup>. In the case of ellipsoids, going from spheres to needles as the extreme cases, the electric polarizability for an incident field direction parallel to the principle axis is given as

$$\alpha = V \frac{\epsilon_m - \epsilon_d}{\epsilon_d + L(\epsilon_m - \epsilon_d)} \quad (4.14)$$

where  $V$  is the volume of the ellipsoid ( $V = 4\pi/3 abc$ ) and  $L$  is a geometrical factor that may take any value from 0 to 1. As for spheres, the resonance occurs and a surface mode is excited when the denominator of  $\alpha$  vanishes. For ellipsoids this occurs when

$$\epsilon_m = \epsilon_d \left(1 - \frac{1}{L}\right) \quad (4.15)$$

and the surface plasmon frequency is given by

$$\omega_{sp} = \omega_p L \quad (4.16)$$

The number of distinct geometrical factors,  $L$ , depends on the number of principal axes in the particle. In a sphere ( $a = b = c$ ) there is only one, hence only one extinction peak is observed. For spheroids ( $a = b \neq c$ ) and ellipsoids ( $a \neq b \neq c$ ) there are two and three distinct peaks,

---

<sup>85</sup> Traci R. Jensen, Michelle Duval Malinsky, Christy L. Haynes, and Richard P. Van Duyne. Nanosphere lithography: Tunable localized surface plasmon resonance spectra of silver nanoparticles. *J. Phys. Chem. B*, 104(45):10549–10556, 2000. 36, 38

<sup>86</sup> Rongchao Jin, YunWei Cao, Chad A. Mirkin, K. L. Kelly, George C. Schatz, and J. G. Zheng. Photoinduced Conversion of Silver Nanospheres to Nanoprisms. *Science*, 294(5548):1901–1903, 2001. 12, 37, 111

<sup>87</sup> Yugang Sun and Younan Xia. Shape-controlled synthesis of gold and silver nanoparticles. *Science*, 298(5601):2176–2179, 2002. 37

<sup>88</sup> Y. Sun, B. Mayers, and Y. Xia. Metal nanostructures with hollow interiors. *Advanced Materials*, 15(7-8):641–646, 2003. 37

<sup>89</sup> Sang Hyuk Im, Yun Tack Lee, Benjamin Wiley, and Younan Xia. Large-scale synthesis of silver nanocubes: The role of hcl in promoting cube perfection and monodispersity. *Angewandte Chemie International Edition*, 44(14):2154–2157, 2005. 37

respectively, related to the number of different axes. Knowing that a deviation from a spherical shape will lower the value of the geometrical factor, the red-shift of the resonance frequency is clearly evident from equation 4.16. Similarly, metallic nanorods will give rise to a splitting of the plasmon resonance corresponding to electron oscillations along the major and minor axis of the rod. As the aspect ratio of the nanorods increases, the separation of the two resonance peaks will be more pronounced<sup>90</sup>.

### Effect of dielectric environment

As seen in the equations for the plasmon resonance and the polarizability of a metallic particle (equations 4.4 and 4.7), the dielectric constant of the surrounding medium plays a big role. An increase of the dielectric constant will lower the surface plasmon frequency and hence red-shift the resonance<sup>91,92,93,38,35</sup>. The plasmon peak of a particle in vacuum ( $\epsilon_d = 1$ ) will accordingly get redshifted when placed on a substrate and even get further redshifted by fully embedding it in a medium of higher dielectric constant. Remembering that the dielectric constant is simply the square of the (complex) refractive index, relevant work has been done that clearly shows the linear relationship between the refractive index of an underlying substrate and the surface plasmon resonance peak<sup>94</sup>. Modeling done in connection with the same work also shows the red shifting of the peak as a silver nanoparticle gradually sinks into a substrate of muscovite mica ( $n = 1.6$ ). To simplify, the permittivity of the surrounding medium can be taken as the average of the substrate and the external medium, written as  $\epsilon_d = (\epsilon_{sub} + \epsilon_{ext})/2$ . All in all, fully or partially changing the dielectric surroundings of metallic nanoparticles may enhance the tunability of the surface plasmon resonance wavelength significantly<sup>35</sup>. In fact, experiments have shown that introducing underlying substrates and overcoating mediums of different dielectric properties and thicknesses to silver islands, give rise to a wide tunable wavelength range of 506-1310 nm. A study done on coating identical nanoparticles with an oxide

---

<sup>90</sup> Eliza Hutter and Janos H. Fendler. Exploitation of localized surface plasmon resonance. *Adv. Mater.*, 16(19):1685–1706, 2004. 37

<sup>91</sup> G. Xu, M. Tazawa, P. Jin, S. Nakao, and K. Yoshimura. Wavelength tuning of surface plasmon resonance using dielectric layers on silver island films. *Appl. Phys. Lett.*, 82(25):3811–3813, 2003. 37, 38

<sup>92</sup> H. Mertens, J. Verhoeven, A. Polman, and F. D. Tichelaar. Low-loss fiber accessible plasmon waveguide for planar energy guiding and sensing. *Appl. Phys. Lett.*, 85(8):1317–1319, 2004. 37

<sup>93</sup> Jack J. Mock, David R. Smith, and Sheldon Schultz. Local refractive index dependence of plasmon resonance spectra from individual nanoparticles. *Nano Letters*, 3(4):485–491, 2003. 36, 37

<sup>94</sup> Michelle Duval Malinsky, K. Lance Kelly, George C. Schatz, and Richard P. Van Duyne. Nanosphere lithography: Effect of substrate on the localized surface plasmon resonance spectrum of silver nanoparticles. *J. Phys. Chem. B.*, 105:2343–2350, 2001. 37

overcoating, shows that the localized surface plasmon frequency can be shifted 4nm per nm thickness of the oxide.

### **Metal shell particles**

In the case of spherical core-shell particles composed of a dielectric core and a metal shell, plasmon modes can be excited on both the inner and outer surface of the metal shell. The plasmon resonances of these nanoshells are sensitive to the inner and outer radius of the metallic shell. Because of the finite thickness of the shell layer, the plasmons on each interface interact with each other depending on the thickness of the shell and the finite penetration depth of the exciting light. Coupling between these plasmon modes gives rise to a splitting of the plasmon resonances into two new resonances: one at lower energy, according to the symmetric polarization of the inner and outer surface, and one mode at higher energy related to the inner and outer surfaces being oppositely polarized<sup>95</sup>. The symmetric mode has a large net dipole moment and can interact strongly with incident electromagnetic radiation in the optical regime; the antisymmetric mode however, does not couple strongly and hence is not observed in the optical spectrum. The result of introducing a dielectric core to the bulk metal particles is a red-shift of the plasmon resonance and a further red-shifting as the thickness of the metallic shell-layer is reduced. The plasmon frequency can thus be tuned over a large wavelength range by changing the ratio between the inner and outer radius of the shell<sup>96</sup>.

#### **4.1.5 Utilizing surface plasmons in solar cells**

Surface plasmon effects offer a range of exciting possibilities for photovoltaics. In addition to increasing the absorption in thin films, by utilization of the reverse process, increased emission from thin films has been reported with the potential of increasing the efficiency of LEDs<sup>97,98,99</sup>. Surface plasmons also raise the possibility of absorbing photons that are normally lost by transmission using

---

<sup>95</sup> E. Prodan, C. Radloff, N. J. Halas, and P. Nordlander. A hybridization model for the plasmon response of complex nanostructures. *Science*, 302(5644):419–422, 2003.38

<sup>96</sup> S. J. Oldenburg, R. D. Averitt, S. L. Westcott, and N. J. Halas. Nanoengineering of optical resonances. *Chemical Physics Letters*, 288(2-4):243 – 247, 1998. 38

<sup>97</sup> W. L. Barnes. Electromagnetic crystals for surface plasmon polaritons and the ex-traction of light from emissive devices. *J. Lightwave Technol.*, 17(11):2170, 1999.41

<sup>98</sup> K. R. Catchpole, S. Pillai, and K. L. Lin. Novel applications for surface plasmons in photovoltaics. In *Photovoltaic Energy Conversion, 2003. Proceedings of 3<sup>rd</sup> World Conference on*, volume 3, pages 2714–2717 Vol.3, 2003. 8, 41, 42

<sup>99</sup> S. Pillai, K. R. Catchpole, T. Trupke, G. Zhang, J. Zhao, and M. A. Green. Enhanced emission from si-based light-emitting diodes using surface plasmons. *Applied Physics Letters*, 88(16):161102, 2006. 38, 39, 40, 41

the concept of up-conversion. It is the giant local field created by the excitation of surface plasmons that is responsible for this possible frequency conversion for photovoltaics. Also, utilizing surface plasmons in textured emitters have been proposed as a way of increasing the efficiency of thermos-photovoltaic systems. This way the waste radiant heat, which is mostly emitted by sub-bandgap radiation, can be trapped more efficiently inside the system before they can be converted into electricity.

Using light of a certain frequency may excite surface plasmons on metal nanoparticles which in turn scatters the light into the underlying substrate. This emitted light will travel along a longer path within the semiconductor or even be bound to a guided mode (experience total internal reflection), and hence the possibility of absorption is increased in the relatively poor absorbing silicon. A principle schematic can be seen in figure 4.6.

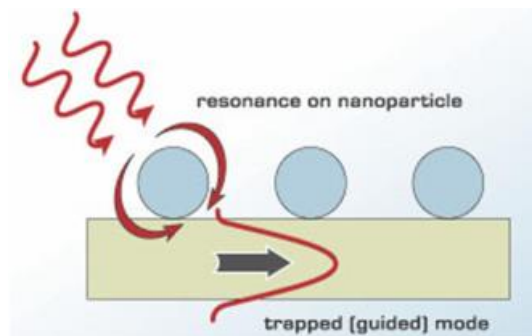


**Figure 4. 6** A surface plasmon is excited on a metal nanoparticle by light of suitable frequency, which then re-radiates the light into a trapped waveguide mode in the silicon<sup>100</sup>

The most popular way of looking at the situation is by considering a dipole located at an interface between air and silicon. The dipole mode can emit light into angles that should normally not be accessible when light goes from air into silicon. This can be related to the fact that light scattered with high in-plane wavevectors are evanescent in air but can propagate in silicon.

---

<sup>100</sup> K. R. Catchpole, S. Pillai, and K. L. Lin. Novel applications for surface plasmons in photovoltaics. In Photovoltaic Energy Conversion, 2003. Proceedings of 3<sup>rd</sup> World Conference on, volume 3, pages 2714–2717 Vol.3, 2003. 8, 41, 42

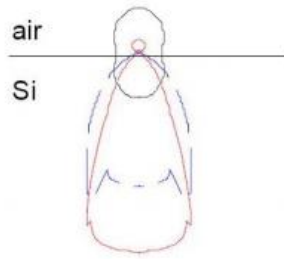


**Figure 4. 7** Shows radiation patterns for a point dipole at a distance of 20 nm from a Si substrate (blue dashed line), for the case of free space (black solid line) and for a point dipole 60 nm from the Si substrate (red line)<sup>27</sup>

Figure 4.7 depicts the radiation patterns for a point dipole located at and above a surface with index of refraction 3.5 together with that of a dipole in free space. It is clear that only a tiny fraction of the light is radiated into the air while the vast majority (96%) goes into the silicon. This is in good agreement with experiments showing the effective energy transfer from a dipole into a higher index substrate, and is related to the high density of optical modes in a semiconductor compared to air. As the dipole is placed at 60 nm above the same surface, a smaller but still significant fraction of the light (84%) is radiated into the silicon. The radiation is also directed less horizontally in the substrate as the distance to the dipole increases, as observed in the figure, possibly reducing the path that light travels inside the silicon. However, as the same distance is increased, the effective cross-section decreases, leaving us with a trade-off between increasing the cross-section and the fraction of light coupled into the silicon. It has been shown theoretically that the particle shape is of crucial importance in determining the light trapping efficiency, and for optimized shapes the path length in thin films were estimated to be enhanced up to a factor of 30<sup>101</sup>.

**Metallic nanoparticles as back reflectors** In the case of plasmonic light trapping, metallic nanoparticles can also be deposited on the rear of solar cells as this have been found to increase the reflectance back into the silicon<sup>102</sup>. This ensures short wavelength light to be absorbed in the silicon before reaching the particles, rather than being lost as it tends to be dissipated as heat in the metallic nanoparticles.

**Plasmonic light trapping by different mechanisms** The enhanced absorption in plasmonic solar cells is usually ascribed the increased optical path length inside the wafer, caused by the light being

<sup>101</sup> K. R. Catchpole and A. Polman. Design principles for particle plasmon enhanced solar cells. *Applied Physics Letters*, 93(19):191113, 2008. 42, 119

<sup>102</sup> K. R. Catchpole and A. Polman. Design principles for particle plasmon enhanced solar cells. *Applied Physics Letters*, 93(19):191113, 2008. 42, 119

reemitted in directions along the wafer after the interaction with small metal nanoparticles<sup>103</sup>. It is possible however, that the electric field created in the immediate vicinity of the particles can excite electron-hole pairs without phonon assistance<sup>104</sup>. As opposed to the former approach, this absorption mechanism is based on a direct generation where the conservation of momentum is preserved through a transfer of momentum to the metal particle instead of through phonons. However, as simulations have shown<sup>105,106</sup>, the near-field of the particle resides outside of the semiconductor volume when the particles are deposited on top of the surface. Hence, to get the biggest contribution from the direct carrier generation and to study the effects more thoroughly, the particles should be fully embedded inside the active region of the semiconductor, as shown in figure 4.8b. The direct absorption gives an extra contribution to the indirectly generated electron-hole pairs. This effect may constitute important corrections to the total absorption in plasmonic solar cells.

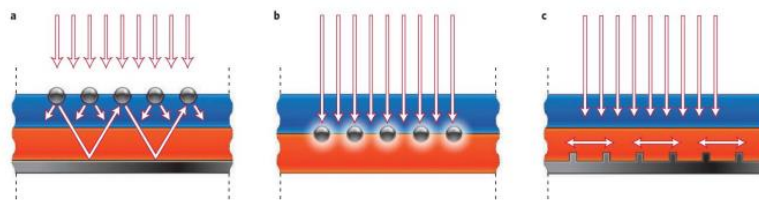


**Figure 4. 8** Different geometries for plasmonic light trapping in thin-film solar cells - (a) scattering from metal nanoparticles into high angles in the semiconductor, causing increased optical path lengths in the cell. (b) The near-field of the excited metal nanoparticles causes the direct generation of electron-hole pairs. (c) Excitation of surface plasmon polaritons at the metal/semiconductor interface ensures the coupling of incident light to photonic modes propagating in the semiconductor layer plane.<sup>107</sup>

<sup>103</sup> S. Pillai, K. R. Catchpole, T. Trupke, and M. A. Green. Surface plasmon enhanced silicon solar cells. *Journal of Applied Physics*, 101(9):093105+, 2007. 8, 15, 38, 39, 42, 43, 44, 51, 119, 121

<sup>104</sup> M. Kirkengen, J. Bergli, and Y. M. Galperin. Direct generation of charge carriers in c-si solar cells due to embedded nanoparticles. *Journal of Applied Physics*, 102(9):093713, 2007. 43

<sup>105</sup> S. H. Lim, W. Mar, P. Matheu, D. Derkacs, and E. T. Yu. Photocurrent spectroscopy of optical absorption enhancement in silicon photodiodes via scattering from surface plasmon polaritons in gold nanoparticles. *Journal of Applied Physics*, 101(10):104309, 2007. 43

<sup>106</sup> D. Derkacs, S. H. Lim, P. Matheu, W. Mar, and E. T. Yu. Improved performance of amorphous silicon solar cells via scattering from surface plasmon polaritons in nearby metallic nanoparticles. *Applied Physics Letters*, 89(9):093103, 2006. 43, 119, 120, 122, 123

<sup>107</sup> Harry A. Atwater and Albert Polman. Plasmonics for improved photovoltaic devices. *Nat Mater*, 9:205–213, 2010. 8, 28, 43

## Chapter 5

### Experimental Procedures

In this chapter, the process of manufacturing of BHJ plasmonic organic photovoltaic devices will be described and analyzed. The preparation of materials used, the fabrication and characterization procedures are presented.

#### 5.1 Materials Preparation

##### Preparation of the P3HT:PCBM Active Layer blend

Regioregular P3HT was purchased from Rieke Metals and PCBM was purchased from Nano-C. Regioregular P3HT and PCBM were dissolved in 1,2-dichlorobenzene (*o*-DCB) in a 1:1 ratio and stirred continuously overnight at 75°C. Then the metallic NPs were blended into the P3HT:PCBM solution at different weight ratios (wt%) just before the deposition of the active layer so as to have a fresh solution. Composite blends with many different concentration (wt%) of Au NPs and Al NPs were prepared.

##### Preparation of PCDTBT:PC<sub>71</sub>BM Active Layer blend

PCDTBT and PC<sub>71</sub>BM were purchased from Solaris Chem. PCDTBT:PC<sub>71</sub>BM were dissolved in 1,2-dichlorobenzene:Chlorobenzene(3:1) (*o*-DCB:CB) in a 1:4(4mg:16mg) ratio and stirred for at least 72 hours at 80 °C before used.

##### Preparation of PTB7:PC<sub>71</sub>BM Active Layer blend

PTB7 and PC<sub>71</sub>BM were purchased from 1-Materials and Solene B.V. respectively. PTB7: PC<sub>71</sub>BM were dissolved in CB:DIO (97:3 v/v) in a 1:1.5 (10mg:15mg) ratio and stirred overnight before used.



**Figure 5.1** Processes of solutions preparation: (a) materials used (b) chemical weighing with balance (c) solution stirring

#### Surfactant-free NPs preparation

The generation of NPs was performed by ultrafast laser ablation of metallic targets (Au/99.99% ,Al/99.99%). This technique provides the possibility of generating a large variety of NPs that are free of both surface-active substances and counter-ions<sup>108</sup>. The targets were placed into a Pyrex cell and covered by a layer of absolute ethanol (Figure 5.2) A femtosecond (pulse duration  $\approx 100$  fs and repetition rate  $\approx 1$  kHz) laser beam was focused onto the target through the ethanol layer. The cell was mounted on a computer-driven XY stage and translated during laser exposure. More experimental details can be found elsewhere<sup>109</sup>. Laser irradiation gives rise to a high temperature gradient in the metal bulk and melting of a thin layer of the target. A fraction of the molten layer of the target is dispersed into the liquid as NPs. The morphology of NPs was characterized with high-resolution transmission electron microscopy (HRTEM).

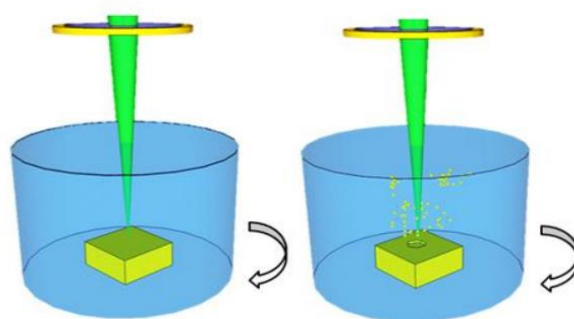


**Figure 5.2** Schematic illustration of laser-assisted production of surfactant-free NPs

### Ligand coated NPs fabrication

Gold nanorods with an aspect ratio of  $\sim 2.6$  were prepared by an optimized one step seed mediated growth method. Briefly, a seed solution was prepared by mixing aqueous solutions of hexadecyltrimethylammonium bromide (CTAB, 2 M, 1 mL) and sodium tetrachloroaurate (III) dehydrate (5 mM, 1 ml) at 40°C. Then, an ice-cold solution of sodium borohydride (0.01 M, 0.5 mL) was added drop-wise to the solution under rapid stirring, resulting in a colour change from dark yellow through to colourless and finally light brown. After the addition, the solution was stirred for an additional two minutes and used immediately after.

A growth solution containing aqueous solutions of CTAB (0.2 M, 14.24 ml), sodium tetrachloroaurate (III) dehydrate (5 mM, 2 ml) and silver nitrate (5 mM, 0.21 ml) was prepared with gentle stirring at 40°C. After that, a freshly prepared solution of L-ascorbic acid (0.0788 M, 0.16 ml) was added, resulting in a colour change from deep yellow to colourless. After 30 s, the gold seeds

<sup>108</sup> E. Stratakis , M. Barberoglou , C. Fotakis , G. Viau , C. Garcia , G. A. Shafeev  
*Opt. Express* 2009 , 17 , 12650 .

<sup>109</sup> E. Stratakis , V. Zorba , M. Barberoglou , C. Fotakis , G. A. Shafeev , *Nanotechnology* 2009 , 20 , 105303 .

solution (16  $\mu\text{L}$ ) was injected to the growth solution. The solution was left unstirred overnight at 40°C. A colour change from colourless to blue/green indicated the formation of AuNRs. Excess of CTAB was subsequently removed by centrifugation (16400 rpm, 15 min, 25°C 2x) and re-dispersion in Milli-Q water.

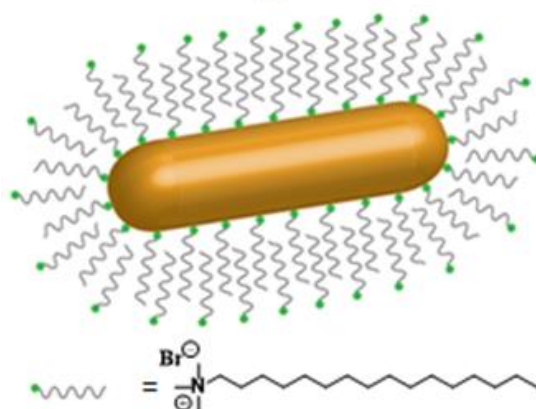


**Figure 5.3** Schematic illustration of Au NRs synthesized via chemical means

## 5.2 Device Fabrication

There are six critical steps which lead from the substrate to the integrated device:

1. Cleaning of ITO coated substrates
2. Deposition of PEDOT: PSS layer
3. Active Layer Deposition
4. Deposition of Cathode
5. Deposition of  $\text{TiO}_x$  Layer(Optional)
6. Thermal annealing (Optional)
7. Vacuum drying (Optional)

In general it is desirable to fabricate OPV devices in a cleanroom to produce results with as high a consistency as possible. However, OPVs are relatively tolerant to dust, as it is insulating and generally only stops the device working where the dust has landed on the surface (leading to dead spots for OPVs). As this is typically a small fraction of the active area it is therefore possible to fabricate outside of a cleanroom so long as some care is taken. However, one particular problem is that dust can change the surface wetting properties where it has landed on the substrate leading to pinholes and therefore shorting of devices. This is particularly relevant when spin coating of PEDOT:PSS on the ITO which needs to be in pristine condition.



**Figure 5.4** Nitrogen filled glove box for OPVs fabrication

Processing without a glovebox is also possible but does cause some issues which need to be considered. Thin films of PEDOT:PSS are hygroscopic and absorb water very easily from the atmosphere which leads to phase separation of the PEDOT from the PSS which degrades performance rapidly. The active layer can also be degraded by oxygen and water, especially in the presence of light. Processing under low intensity red light significantly improves stability of thin films of active layers but it is still essential to minimize the exposure time. Reactive interface layers such as calcium must also be avoided when processing in air. One of the most important factors in a fabrication run is the handling of the substrates. Substrates should in general only be handled with tweezers and care must be taken to avoid touching the active areas as this will scratch the films and cause failures due to shorting of the anode and cathode. The diagram below shows the active areas in red which must not be touched by the tweezers as well as the safe handling zone.

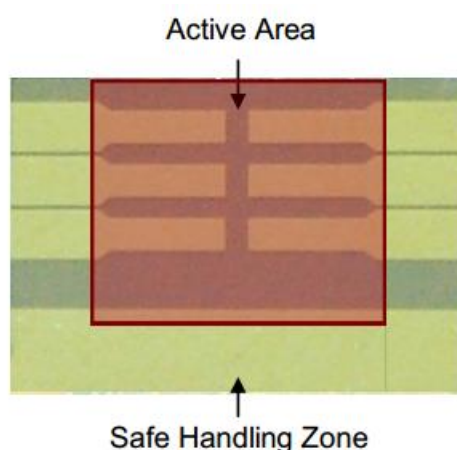


**Figure 5.5** Illustration of safe handling zone and active area of an OPV device

It is also essential the substrates should be kept the right way up. Even though a surface can look clean this is not the same as a surface being chemically clean. Where the active surface has been in contact

with other surfaces (even clean surfaces such as cleanroom tissues) this typically leads to device defects. As such, substrates that have been dropped and landed active face down should be discarded for best device data.



**Figure 5.6** Tweezer for device safe handling

### Substrate Cleaning

Glass substrates coated with ITO and 20x15x1.1 mm size were purchased by Luminescence Technology Corp. The ITO layer has about 100nm thickness and a surface resistance of  $\sim 20 \Omega/\text{sq}$ .

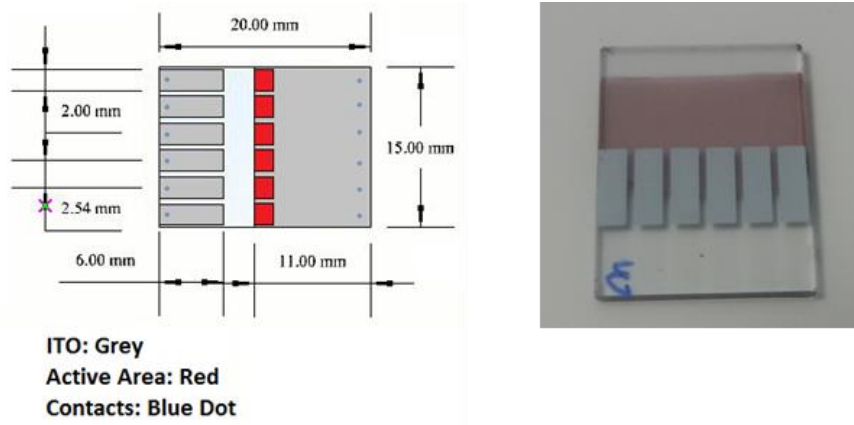


**Figure 5.7** Schematic drawing shows physical dimensions of patterned ITO glass and (b) photograph of the ITO pattern design on the glass for device fabrication.

The cleaning procedure of ITO-coated glass substrates from any surface contamination is constituted by seven steps:

1. Placement of the substrates in the holder and immersion in a solution of soap (10%)-deionized water in a beaker. Ultrasonic bath for 10 minutes.
2. Rinse with deionized water.
3. Immersion in acetone into a beaker. Ultrasonic bath for 10 minutes.
4. Rinse with Isopropanol (IPA).
5. Immersion in IPA in a beaker. . Ultrasonic bath for 10 minutes.

6. Transfer the samples in a Petri dish. Placement of the dish in oven at 120°C for 10 minutes for drying. The right side is easy found by using a multimeter as such the ITO layer is not visible to the naked eye.
7. Place the substrates inside a vacuum ozone cleaner chamber for 15 minutes at  $\sim 1\text{mW}/\text{cm}^2$  in order to remove any residual organic contamination.



**Figure 5.8** Preparation for substrate cleaning



**Figure 5.9** Substrates in ultrasonic bath



**Figure 5.10** Placement of the substrates in oven

### **Deposition of PEDOT: PSS**

As mentioned above PEDOT: PSS performs three functions-smoothing the surface of ITO, produces a better interlayer with P3HT («energy match») and most importantly, acts as the transport layer only holes («electron blocking»). Ensuring a good layer of PEDOT: PSS is of great importance for an efficient layout. PEDOT: PSS requires a very clean and hydrophilic surface in order to make the best quality of coating layer, which can be achieved by the cleaning referred above.

PEDOT: PSS was purchased by Heraeus. Afterwards it was filtered with filters 0.45 micron PVDF, before a deposition, to remove any imperfection.

The deposition occurred by spin coating. Spin coating is a very useful technique for deposition of thin uniform films on planar substrates. It's a very simple process, illustrated in Figure 5.11. A solution is placed on the substrate; the substrate is rotated at an adjustable angular velocity resulting to the spreading of the liquid due to centripetal force. The rotation continues for an adjustable time. The time and the speed of rotation determine the amount of solution that will remain on the substrate (and hence the layer thickness) as shown by the formula 5.1 with layer thickness ( $t$ ), the ( $\eta$ ) the viscosity of material in connection with the concentration and angular rotational velocity. Once the rotation terminates the sample is allowed to dry and the procedure repeated with another solution for the manufacture of multilayer.

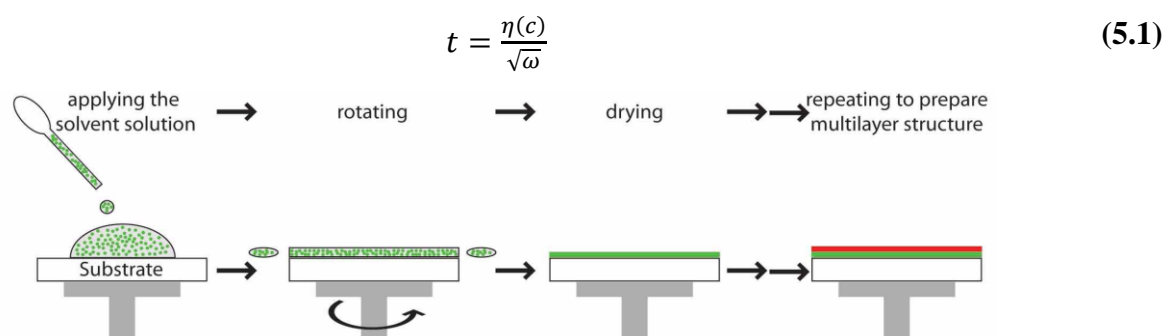


Figure 5.11 Spin coating Procedure

Studies have shown that this type of PEDOT: PSS layer is optimal at 5000rpm for 30sec to achieve layer thickness  $\sim 40\text{nm}$  (and surface resistance  $< 800/\text{sq}$ ) for P3HT:PCBM and 6000rpm for 60 sec to active layer thickness of  $\sim 30\text{nm}$  for PCDTBT:PC<sub>71</sub>BM and PTB7:PC<sub>71</sub>BM system. To minimize the use of material (and therefore the cost) deposition can be done by pipetting, leaving only 30 $\mu\text{l}$  at the center of the substrate. To maximize the performance, the samples with imperfections that can be observed by the naked eye, rejected.

Following the spin coating process, a stripe of PEDOT: PSS layer at one of the edges of the square substrate, swabbed with a cotton bud wetted with deionized water. This strip is removed in order to ensure the contact of the electrode with the ITO layer and not with PEDOT: PSS. The PEDOT: PSS removal is very easy, since it is water soluble.

The whole process carried out outside glovebox since there was no infrastructure. Finally, the substrates were placed in an oven at 120°C for 15 minutes in order to remove any humidity residues.

It is extremely important to note that the exposure time of PEDOT: PSS in the air should be minimized because the performance deteriorates rapidly. The humidity of the atmosphere is a negative factor because can lead to morphological changes due to the creation of an insulating layer on the surface, which is rich in PSS and deteriorate the performance.

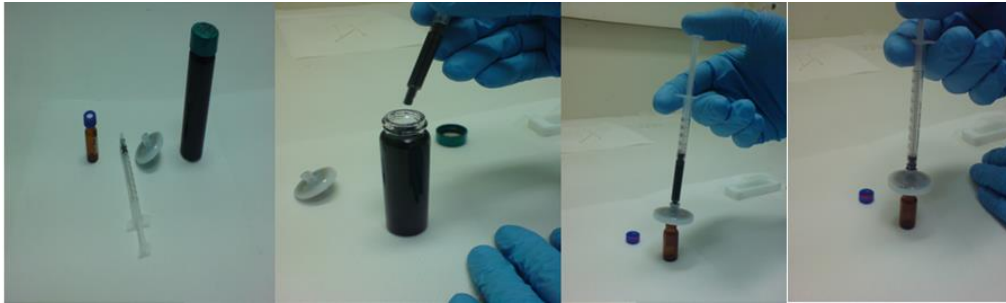


**Figure 5.12** PEDOT:PSS filtering process

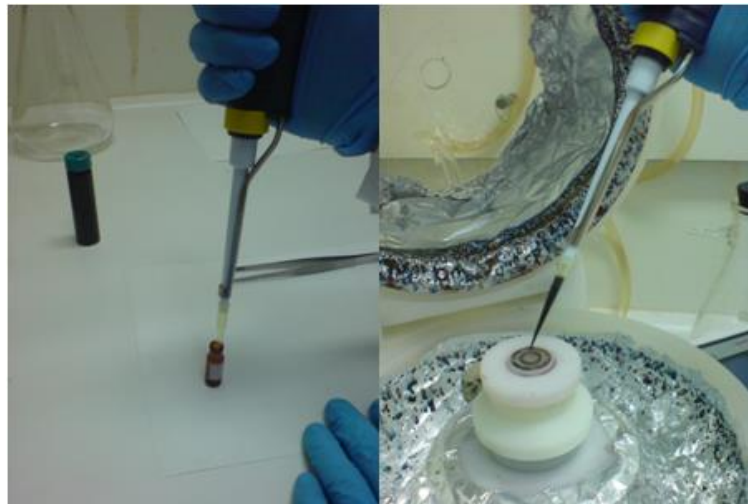


**Figure 5.13** Spin coating of filtered PEDOT:PSS

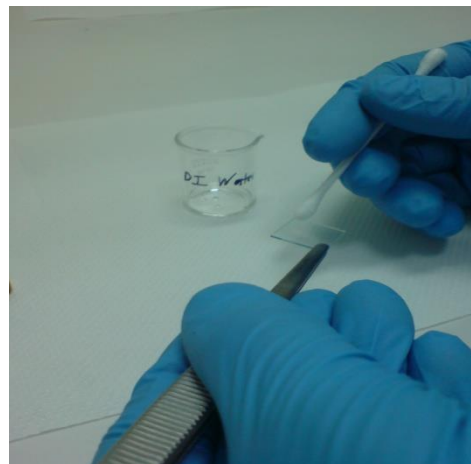


**Figure 5.14** Cleaning PEDOT:PSS with a cotton swab



**Figure 5.15** Second production step of a device. In this figure is illustrated a microscopic view of spin coated PEDOT:PSS film on etched ITO

### Deposition of Photoactive layer

The third step during the manufacturing of an organic solar cell is the deposition of the most important element in the device, the photoactive layer. After the preparation of active blend (5.1) layers of approximate thickness 200nm for P3HT:PCBM and approximate thickness of 80nm and 100nm for PCDTBT:PC<sub>71</sub>BM and PTB7:PC<sub>71</sub>BM respectively were deposited by spin coating method. The most efficient device was observed at 1000rpm until the drying of the device for each case.

Afterwards, the stripe of photoactive layer that is above the removed PEDOT:PSS stripe, was swabbed by the same procedure and chloroform.

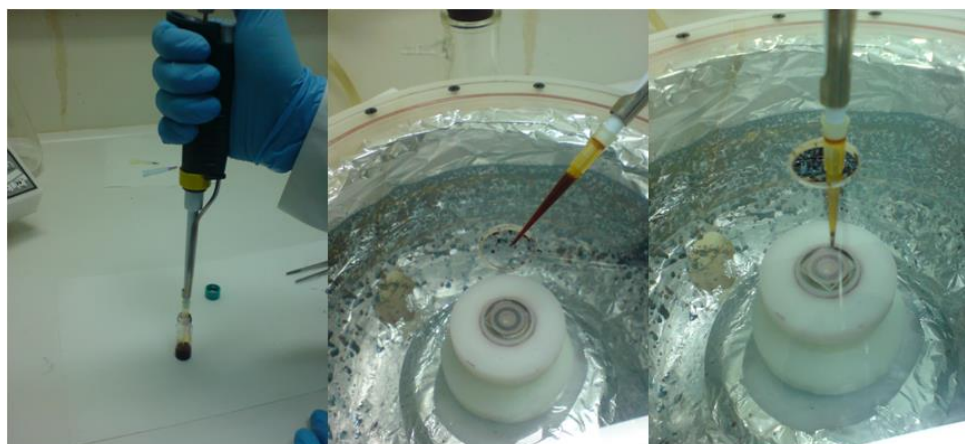


**Figure 5.16** Spin Coating of Active Layer

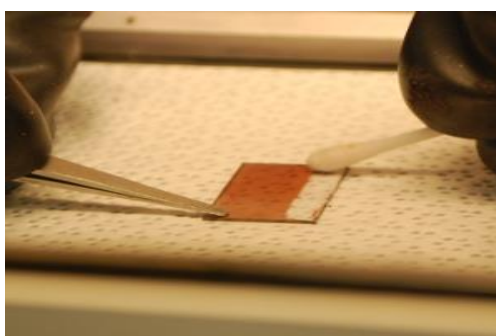


**Figure 5.17** Cleaning with a cotton swab

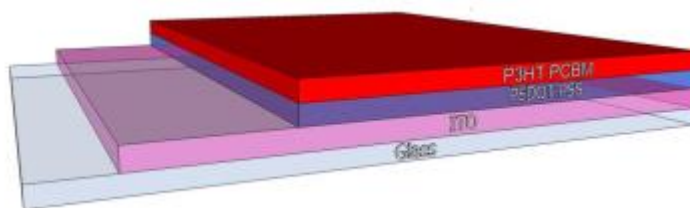


**Figure 5.18** Third production step of a device. Microscopic view of spin coated active layer film

### Deposition of TiO<sub>x</sub> Layer (Only for PCDTBT:PC<sub>71</sub>BM based devices)

TiO<sub>x</sub> solution preparation: Titanium(iv) isopropoxide ( $\text{Ti}[\text{OCH}(\text{CH}_3)_2]_4$ , 5 ml), 2-methoxyethanol ( $\text{CH}_3\text{OCH}_2\text{CH}_2\text{OH}$ , 20ml) and ethanolamine ( $\text{H}_2\text{NCH}_2\text{CH}_2\text{OH}$ , 2ml) were added to a three-necked flask in a nitrogen atmosphere. The solution was then stirred for 1 hr at room temperature, followed by heating at 80°C for 1 hr and 120°C for 1 hr. The solution was then cooled to room temperature and 10 ml of isopropanol (IPA) was added. The TiO<sub>x</sub> interlayer was dissolved in methanol (1:200) and then spin-coated to a thickness of approximately 10 nm (6000 rpm, 40 s) in air.

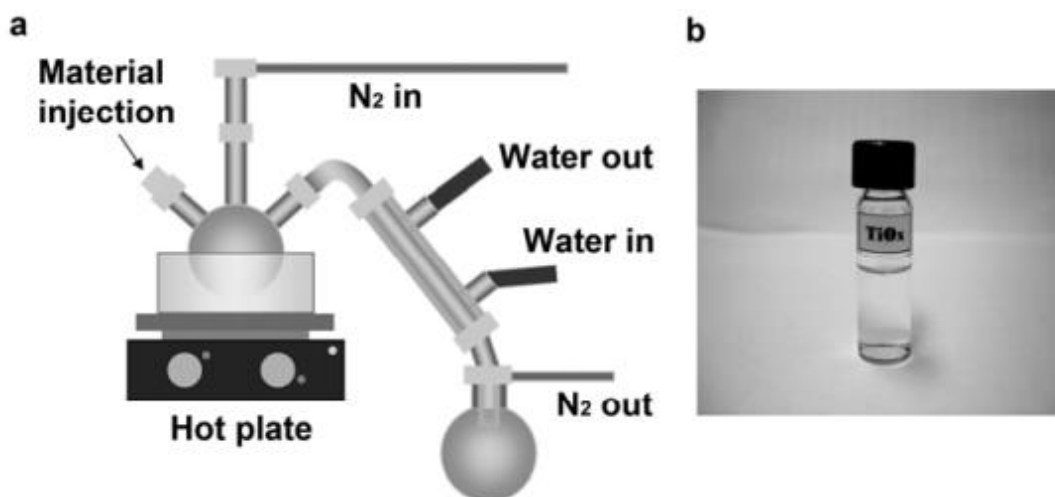


**Figure 5.19** Preparation of the TiO<sub>x</sub> precursor solution. a. Schematic drawing of the sol-gel processing apparatus. b. Photo of the TiO<sub>x</sub> sol-gel precursor diluted by 1:200 in methanol ( $\text{CH}_3\text{OH}$ ). The solution is transparent and colorless.



**Figure 5.20** Setup used for the for the preparation of  $\text{TiO}_x$  Layer

### **Deposition of Cathode**

A different deposition technique is the vacuum thermal evaporation (VTE). In this process, small pieces of material, which we want to deposit, are placed in a cavity enclosed within a vacuum chamber. The substrate that is to become the coating is placed on a special base, which is known as the boat, over the cavity. The cavity is supplied with current, due to its Ohmic resistance is heated and the material pieces melt and evaporate. The vaporized molecules of the material overlay on the substrate and form the coating. The coating thickness depends on the distance of the substrate from the cavity (source evaporation) and the time of supply with electricity. The overlay can be made on specific parts of the substrate with the use of masks, leaving uncovered the points we want cover with the material.

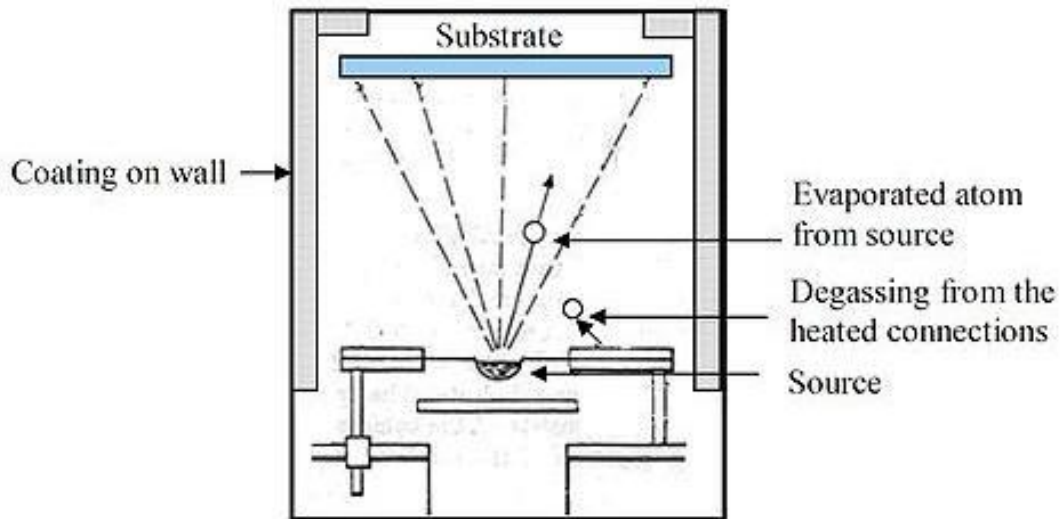


**Figure 5.21** Procedure inside the vacuum chamber

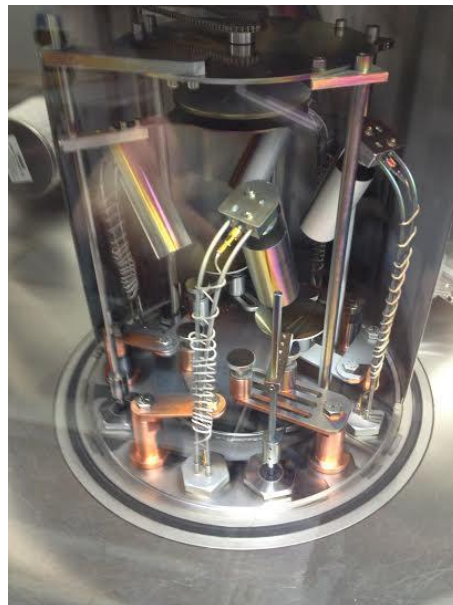


**Figure 5.22** Thermal Evaporator Chamber

### **Thermal annealing (Only for P3HT:PCBM based devices)**

Thermal treatment can be applied either to the final device (post-annealing), or the device prior to deposition of the cathode (pre-annealing). In our device fabrication, we apply only post-annealing. Time and temperature are the two main factors during this process. However, the most important factor to decide these factors' values is the materials which will be used during the OPV manufacturing.

The device's efficiency depends strongly on the manufacturing conditions, which affect the self-organization of the polymer and the related optical and electrical properties. It has been shown that the P3HT crystallinity may be increased by thermal annealing, forming crystallites with conjugated chains parallel to the substrate. The improved crystallinity increases the absorption of light in the near infrared range, holes' mobility and reduces carrier recombination due to improved refining pathways. All of the above contribute to a better cell performance. Kim et al. reported the importance of regioregularity to self-organization of P3HT, and to increment of crystallinity through thermal treatment.

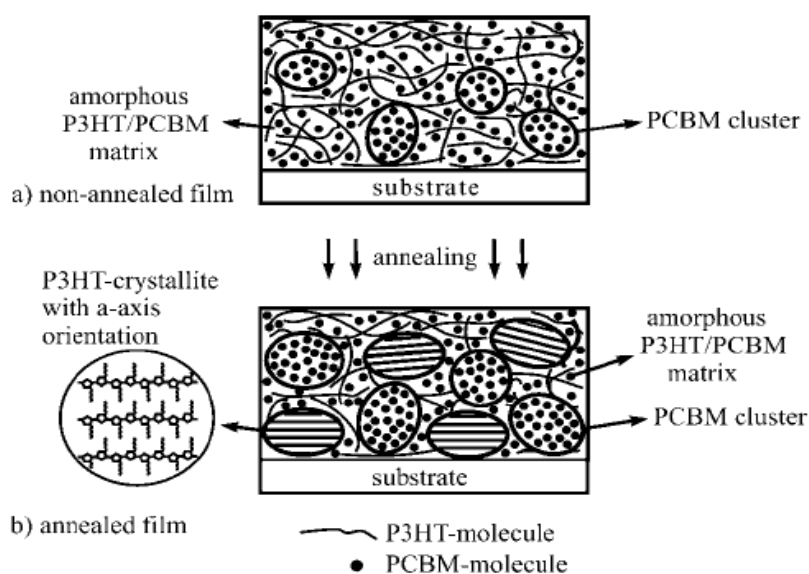


**Figure 5.23** Illustration of the microscopic reorganization during the thermal treatment of the active layer. The clusters of PCBM (after the thermal treatment) grow, thus there is more space for self-organization, crystallization of P3HT chains

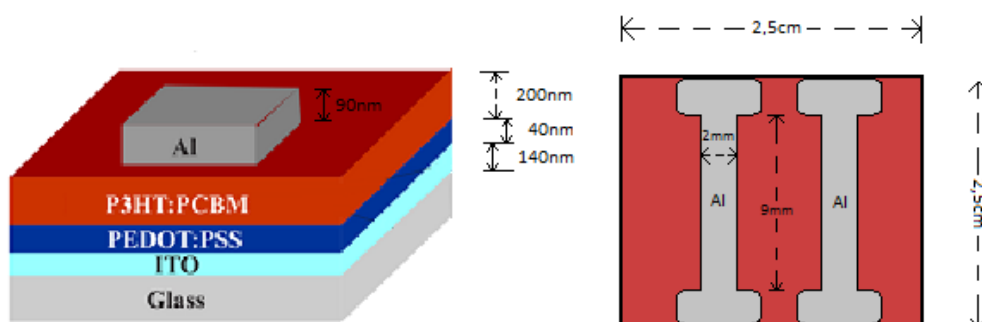


**Figure 5.24** Schematic Illustration of the fabricated device

### **Vacuum drying (Only in PTB7:PC<sub>71</sub>BM based devices)**

In the case of temperature sensitive polymers the use of thermal annealing or thermal drying of polymer:fullerene blends should be avoided. One choice is the drying of photoactive blends inside a nitrogen filled glove box at room temperature for several hours. A more useful approach in this issue is the placement of the as cast films inside a vacuum anti-chamber in order to accelerate the drying process to several minutes not affecting the PV performance of the devices.

In our case PTB7:PC<sub>71</sub>BM based films were placed inside a vacuum anti-chamber for ~15 minutes. The PV characteristics obtained with this method and as well as with natural drying (several hours) were almost the same.

### **5.3 Device Characterization**

The basic characterization of solar cells, includes measurements of the device's current as a function of applied voltage under conditions of darkness and light. A computer controlled voltage and current sources provide the voltage difference and the current across the device. The software that is used is the Easy EXPERT. A lamp that simulates the solar spectrum illuminates (under AM 1.5 conditions) the OPV device under characterization. The OPV device is placed in a specific direction such as the , the ITO side to face the illumination lamp.

#### *Voltage-current*

After the device placing into the characterization set-up, the necessary wiring follows. Initially, we bring together the two electrodes to the device. The one electrode contacts the coated with ITO surface, while the other electrode contacts to the cathode (aluminum metal). The electrodes were rimmed with rounded edges, in order to limit the risk of etching the samples.

Afterwards, the whole layout is covered with a black cloth to start the measurement process under dark conditions. We launch the Easy EXPERT software, select solar cell mode, set the range & step voltage and the time that will elapse between the measurements and finally we obtain the corresponding current-voltage curve in the dark. The algorithm of the program calculates important values for solar cells like current density (J) and short circuit current density ( $J_{sc}$ ), open circuit voltage ( $V_{oc}$ ), maximum efficiency ( $P_{max}$ ), fill factor (FF), cell efficiency (PCE%).

The lamp is turned on and the power is set in order to act as sun simulator ( $100\text{mW}/\text{cm}^2$ ). A reference monocrystalline silicon solar cell from Newport was used to calibrate the lamp in 1 sun. Then, a similar procedure occurs to obtain the current-voltage curve under illumination.

Finally the curves and the values which obtained by Easy Expert software are processed by Origin Pro 9. Where, useful curves also are designed (logarithmic, zoomed curves from  $J_{sc}$  to  $V_{oc}$ ).

### *Aging effect*

Aging effect is called the decay of the device as a function of time. It is important, for understanding the quality of a solar cell to be examined under illumination. The measurements carried out under illumination relates to the change made by time in all major values, such as  $J_{sc}$ ,  $V_{oc}$ , FF and PCE%.

The same wiring is kept by examining current-voltage under illumination. We launch the Easy EXPERT, and using the same options as described above we get a current-voltage curve at a time. After completion of the process, diagrams of short circuit current-time, open circuit voltage-time, fill factor and efficiency-time are made. In these graphs can be seen the reduction of these factors in relation to the time and essentially assume the life of the solar cell.

The timing of measurements varies depending on the technology of the photoactive layer. Optimized cells with photoactive layers without nanoparticles were measured for 45 hours, plasmons solar cells with gold nanoparticles, were measured for about 65 hours and with aluminum nanoparticles for about 150 hours.

### *Other techniques*

The external quantum efficiency measurements were conducted immediately after device fabrication using an integrated system (Enlitech, Taiwan) and a lock-in amplifier with a current preamplifier under short-circuit conditions. The light spectrum was calibrated using a monocrystalline photodetector of known spectral response. The OPV devices were measured using a Xe lamp passing through a monochromator and an optical chopper at low frequencies ( $\sim 200$  Hz) in order to maximize the signal/noise (S/N) ratio. The photoluminescence (PL) measurements of the devices were carried out at room temperature and resolved by using a UV grating and a sensitive, calibrated liquid nitrogen cooled CCD camera, in the wavelength range from 600 to 950 nm using a He-Cd CW laser, at 325 nm with a full power of  $P_0 = 35$  mW, as the excitation source. UV-vis absorption and reflectance spectra were recorded using a Shimadzu UV-2401 PC spectrophotometer over the wavelength range of 300-

800 nm. The cross-section images were collected by field emission scanning electron microscopy (FESEM JEOL-JSM7000F). The size distribution and the morphology of the as fabricated Au NRs were characterized with High Resolution Transmission Electron Microscopy (JEM 2100 Microscope).



## Chapter 6

### Results and Discussion

Organic photovoltaic technology is one of the most up-and-coming sections of solar energy conversion technologies. The introduction of bulk-heterojunction (BHJ) architecture acquired a potentiality because combines the high absorption coefficient of the organic materials and the efficient generation of photo-induced charge carriers under the condition of using a thin film<sup>110</sup>. However, the further increase of efficiency of a BHJ device demands reduction of layer thickness in order to exploit the dissociation of carriers, but that of course would also lead to a decrease of absorption of the BHJ film<sup>111</sup>.

Metallic NPs can vitiate this balance by interesting properties, such as LSPR, SPP and scattering of light as was reported in Chapter 4. Based on this theoretical background previous research has been implemented with the use of different metallic nanostructures (e.g nanowires, nanoparticles) in electrodes, in buffer layer or active layer and between interfaces. Below, the milestones of plasmonic organic photovoltaic cells are represented.

### 6.1 Current state of the art plasmonic OPVs

#### Incorporation of metallic nanostructures in active layer

The first report on the addition of small amounts of metal NPs such as Au and Ag into the photoactive layer was by Kim and Carroll<sup>112</sup>. NPs had 5–6 nm diameters and were stabilized with a ligand shell of dodecyl amine. A performance enhancement of more than 70% was mainly attributed to the introduction of dopant states in the active layer or the interfaces, which improves electrical conductivity and series resistance. The enhancement of absorption due to scattering was reported to be a minor effect.

Improvements in OPVs efficiency due to enhanced scattering by large truncated octahedral 70 nm Au NPs<sup>113</sup> and 40 nm Ag NP clusters<sup>114</sup> embedded in a PCDTBT:PC<sub>70</sub>BM photoactive layer have recently been reported with efficiency enhancements of 13% and 16%, respectively. In case of Au NPs, the efficiency improvement was attributed to the enhanced light absorption due to scattering from NP

---

<sup>110</sup> C. J. Brabec, S. Gowrisanker, J.J.M. Halls, D. Laird, S. Jia, S.P Williams, *Adv. Mater.* **22**, 3839 (2010).

<sup>111</sup> S. H. Park, A. Roy, S. Beaupr., S. Cho, N. Coates, J. S. Moon, D. Moses, M. Leclerc, K.Lee, A. J. Heeger, *Nat. Photonics*, **3**, 297 (2009).

<sup>112</sup> K. Kim, et al. *Appl. Phys. Lett.* **87** (2005) 203113.

<sup>113</sup> D.H. Wang, et al. *Angew. Chem.* **50** (2011) 5519.

<sup>114</sup> D.H. Wang, et al. *Adv. Energy Mater.* **1** (2011) 766.

LSPR modes. On the other hand, the improved charge transport was the reason for the enhanced efficiency of Ag NP-based OPV cells. Moreover, the NP shape is reported to influence the performance of plasmonic OPV cells. In particular, a direct comparison between Ag NPs and NWs was performed<sup>115</sup> with efficiency enhancements of 18% and 7.5%, respectively. Metallic NWs can provide greater enhancement than NPs due to improved electron transport exhibited by the respective devices. In other work, the effect of NP shape has been investigated and Ag NPs were compared with Ag nanoplates as additives in P3HT-PC71BM OPV devices. Results showed an efficiency enhancement of 25% and 37.5% for the NPs and nanoplates, respectively. The superiority of the nanoplates is attributed to their shape, which favors both efficient scattering and light trapping<sup>116</sup>. Theoretical simulations of metallic NPs dispersed in BHJ active layer can estimate the effect of different light trapping mechanisms in the respective conversion efficiency. In this concept, the absorption enhancement in OPVs induced by incorporating Al, Ag, and Au NPs into the active layer was modelled<sup>117,118,119</sup>. Finite element method simulations were employed to study the influence of Ag NPs on light absorption in P3HT:PCBM OPVs<sup>120</sup>. Indeed, absorption enhancements in the order of 1.5 for devices featuring an array of 23 nm diameter NPs with a spacing of 40 nm were predicted. Using a Finite Difference Time Domain method, the role of period, diameter and position of Ag NPs in enhancing the optical absorption of MEH-PPV:PCBM can be performed<sup>121</sup>. An, up to three-fold, increase in absorption is observed due to the localized SPP and scattering<sup>113</sup>. The model was successfully extended to cases of mixed NP types. In addition, a recent study suggested that Al NPs have the potential to yield significantly greater enhancement than Ag or Au, due to the much higher plasma frequency of Al, which ensures a better overlap between plasmon resonance and the absorption band of organic semiconductors<sup>112</sup>. Finally, most recently Kakavelakis et. al. showed that Al NPs lead to better PCE and device stability compared to Au NPs<sup>122</sup> in agreement with the previous studies.

## **Incorporation of metallic nanostructures in buffer layer**

---

<sup>115</sup> C.-H. Kim, et al. *ACS Nano* 5 (2011) 3319.

<sup>116</sup> D.H. Wang, et al. *RSC Adv.* 2 (2012) 7268.

<sup>117</sup> V. Kochergin, et al. *Appl. Phys. Lett.* 98 (2011) 133305.

<sup>118</sup> N. Lagos, et al. *Appl. Phys. Lett.* 99 (2011) 063304

<sup>119</sup> S. Vedraïne, et al. *Sol. Energy Mater. Sol. Cells* 95 (2011) S57–S64

<sup>120</sup> H. Shen, et al. *J. Appl. Phys.* 106 (2009) 073109.

<sup>121</sup> D. Duche, et al. *Sol. Energy Mater. Sol. Cells* 93 (2009) 1377.

<sup>122</sup> G. Kakavelakis, et. al. , *RSC Adv.*, 2013, 3, 16288–16291

The first report on performance enhancement via the incorporation of Au NPs into the PEDOT:PSS layer was by Chen et al.<sup>123</sup>. The addition of Au NPs increased the exciton generation rate and the probability of exciton dissociation, thereby enhancing Jsc and fill factor (FF). An improvement of 20% was observed and was attributed to the local enhancement in the electromagnetic field due to the excitation of LSPR. More information was recently provided by Fung et al., who studied the electrical and optical properties of OPV cells with PEG-capped Au NPs embedded in the PEDOT:PSS layer<sup>124</sup>. It was shown that the absorption enhancement due to incorporation of Au NPs is insignificant and provides only a minor contribution to efficiency enhancement. This was postulated to be due to the lateral distribution feature of the strong near-field of plasmonic resonance around the metallic NPs. Considering electrical characteristics, they showed that the incorporation of an appropriate amount of Au NPs reduces the resistance of the PEDOT:PSS layer. Moreover, there is an increase in the interfacial roughness between P3HT:PCBM and PEDOT:PSS after incorporation of Au NPs. The roughened interface contributes to the improvement of hole collection efficiency and leads to Jsc and FF enhancements.

In another relevant study, monodispersed octahedral 45 nm Au NPs, synthesized by a hydrothermal process<sup>125</sup>, were blended in the PEDOT:PPS of P3HT:PCBM devices<sup>126</sup>. Steady state and dynamic photoluminescence (PL) measurements revealed interplay between the LSPR absorption enhancement and the LSPR induced reduction of exciton lifetime facilitated the charge transfer process. In this way an efficiency enhancement of 19% was observed.

The effect of size of chemically synthesized Au nanospheres (NSs) embedded in PEDOT:PSS was also investigated<sup>127</sup>. It was shown that the efficiency enhancement strongly depends on NP size. Furthermore, Au nanostructures of various sizes and shapes (nanospheres (NSs) and nanorods (NRs)) were mixed with the PEDOT:PSS buffer layer<sup>128</sup>. It was shown that the presence of a combination of NSs and NRs increased the efficiency by 24%. Since NSs and NRs exhibited different absorption bands, efficient light absorption as a result of LSPR and scattering effects was achieved.

Besides this, Au NPs were successfully incorporated into a PEDOT:PSS film, which played the role of the interconnecting layer, which connects the two subcells in an inverted tandem OPV device. The addition of Au NPs improved both the top and bottom subcells' efficiency at the same time via

---

<sup>123</sup> F.-C. Chen, et al. *Appl. Phys. Lett.* 95 (2009) 013305.

<sup>124</sup> D.D.S. Fung, et al. *J. Mater. Chem.* 21 (2011) 16349.

<sup>125</sup> C.C. Chang, et al. *Chem. Mater.* 20 (2008) 7570.

<sup>126</sup> J.-L. Wu, et al. *ACS Nano* 5 (2011) 959.

<sup>127</sup> L. Qiao, et al. *Appl. Energy* 88 (2011) 848

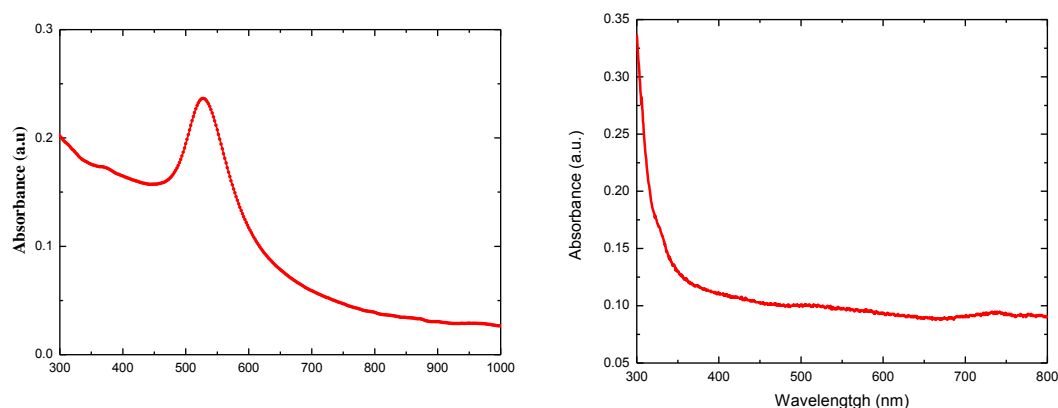
<sup>128</sup> J.Y.S. Hsiao, et al. *J. Phys. Chem. C* 116 (2012) 20731.

LSPR enhancement of their optical absorption. As a result, a 20% improvement of efficiency was attained<sup>129</sup>.

The causes of the improved optical absorption based on a cylindrical Ag-NP optical model, simulated with a 3D FDTD method were recently investigated. The model is able to explain the optical absorption enhancement due to LSPR modes, and provides a greater understanding of Ag-NP shape parameters that play a significant role towards determining broadband absorption phenomena in plasmonic OPVs. An increase of 60% was predicted, due to the strong optical field intensity associated with LSPR<sup>130</sup>.

## 6.2 Surfactant free Nanoparticles

The absorption spectrum of the colloidal Au NPs and Al NPs solution in ethanol is shown in Figure 6.1 with the distinct peak at ~530 nm and ~300 nm respectively, which correspond to the theoretically



predicted enhanced absorption due to plasmon resonance. The respective size distribution determined from a series of TEM images (figure 6.2) indicates that the majority of Au NPs exhibit sizes ranged from 1.5 to 20 nm with an average of ~10 nm. However, a small fraction of NPs with sizes larger than 40 nm is present as well. On the other hand the majority of Al NPs exhibit sizes ranged from 20 to 40 nm with an average of ~30nm. All the colloids prepared were stable against sedimentation for at least several months with no addition of any surface-active substances. The remarkable stability of both types of NPs is further indicated by the slow evolution of the absorption spectrum upon exposure to air.

**Figure 6.1** The measured optical densities of the two types of NPs produced namely Au(left) and Al(right). Reference is absolute ethanol<sup>122</sup>.

<sup>129</sup> J. Yang, et al. *ACS Nano* 5 (2011) 6210.

<sup>130</sup> R.S. Kim, et al. *Opt. Express* 20 (2012) 12649

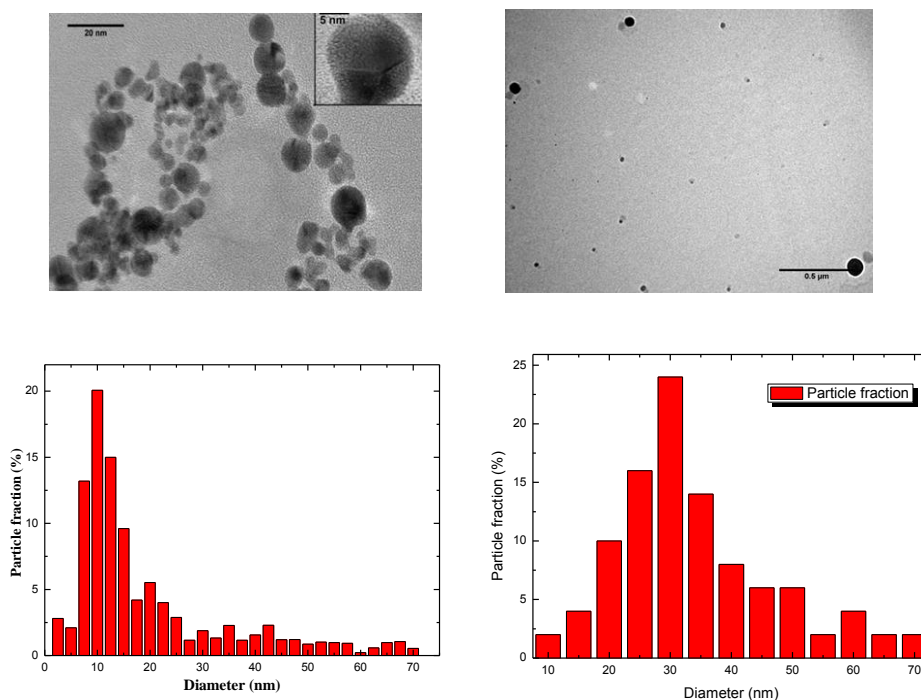


**Figure 6.2** TEM images (Top) of Au (left) and Al (right) NPs generated via ablation of a bulk targets in ethanol using fs laser radiation. (Bottom) Distributions of Au (left) and Al (right) NPs size calculated from the respective TEM images<sup>122</sup>

### 6.3 Ligand Coated NRs

The as prepared Au NRs, were fabricated via the previously described method, had relatively uniform diameters (width and length). Fig. 6.3a shows the transmission electron microscopy (TEM) image of synthesized Au NRs, in which we observe that the NRs were 30 nm in length and 10 nm in width on average as shown also in the histograms in Fig. 6.3b,c. The absorption spectrum of the colloidal Au NRs in aqueous solution is shown in Fig. 6.3d with two distinct peaks, at ~ 510 nm and ~650nm, which corresponds to the theoretically predicted enhanced absorption due to transverse and longitudinal surface plasmon resonance<sup>131</sup>.

<sup>131</sup> Kymakis E., Spyropoulos G.D., Fernandes R., Kakavelakis G., Kanaras A.G., Stratakis E., (2015), ACS Photonics, 2 (6), 714–72

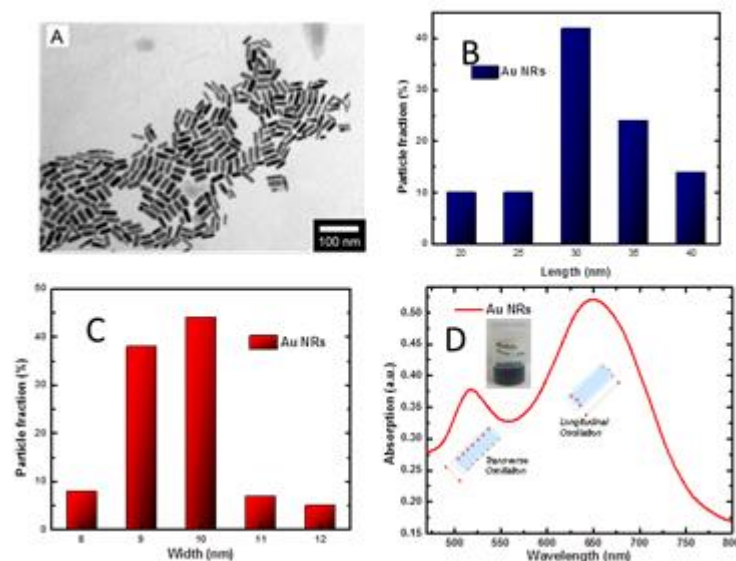


**Figure 6.3** (a) TEM image of the as fabricated Au NRs, (b) length and (c) width distributions of Au NRs and (d) absorption spectra of Au NRs solution.

#### 6.4 Incorporation of surfactant free nanoparticles in P3HT:PCBM active layer

In the present work, surfactant free Au and Al NPs with various diameters are embedded in the poly(3-hexylthiophene) (P3HT):phenyl-C61-butyric acid methyl ester—(PCBM) active layer of OPV devices for enhanced device performance. An improvement in power conversion efficiency by 23% for Au doped devices and by 30% for Al doped devices compared to the pristine device without NPs was achieved. For the Au doped devices, the spectral ranges of both the enhanced light absorption and quantum efficiency comply with the individual LSPR region of the Au NPs used. The efficiency is postulated to be enhanced by exploiting increased absorption around the small diameter NPs integrated into the active layer as well as strong light scattering from the large diameter NPs, both effects stemming from the excitation of the LSP waves at the NP/photoactive layer interface. For the Al doped devices, the PCE enhancement is due to improved absorption caused mainly by scattering effects due to the presence of NPs and due to improvement in the active layer morphology.

The technique of laser ablation generates a large variety of NPs that are free of both surface-active substances and counter-ions. More details for the experimental setup can be found elsewhere<sup>103,104</sup>. The concentration of the initial colloidal solution, determined from gravimetric measurements of the target before and after the completion of the ablation process. OPV devices based on the ITO /PEDOT:PSS/P3HT :PCBM/Al structure with Au and Al NPs embedded in the active layer at different concentrations were fabricated and characterized. The active layers were fabricated by mixing respective solutions of P3HT and PCBM at 1:1 ratio and Au, Al NPs, in dichlorobenzene and spin-coated on top of PEDOT :PSS/ITO. The corresponding volume ratios of the P3HT :PCBM and the Au NPs solutions were ranged from 4%–6% and 8%-10% for the Al solutions. The devices were

post-annealed at 160°C for 15 min in a glove box under nitrogen atmosphere. In all cases, the final active layer thickness, determined from cross-sectional SEM images, is measured to be  $(220 \pm 5)$  nm.

### Au Doped Devices

The UV-Vis absorption spectra of the BHJ devices with Au NPs embedded in the active layer in various concentrations are shown in Figure 6.4. The red shoulder at 602 nm indicates the effective self-organization of the regioregular P3HT.<sup>132</sup> In the spectral region between 450 and 650 nm where the P3HT:PCBM absorbs, an increase in the percentage of absorbance is occurred proportionally to the volume ratio of Au NPs. Notably, the absorption enhancement for 5% and 6% Au NPs concentrations exhibits maximum at 610 nm, which fairly coincides with the extinction peak of the Au NPs, indicating that an LSPR effect does indeed improve the absorption.

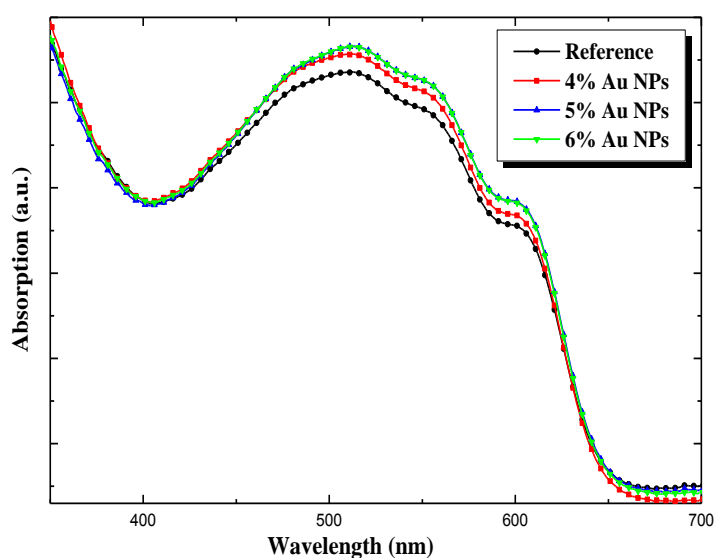


**Figure 6.4** Absorption spectrum of the pristine and Au doped devices

Figure 6.5 displays the current voltage (J-V) characteristics of the pristine and OPV devices with different NPs fractions, under illumination with  $100 \text{ mW/cm}^2$  power intensity. The respective averaged photovoltaic characteristics are summarized in Table I. It is shown that the incorporation of Au NPs in the active layer induces a significant improvement of the device short-circuit current ( $J_{SC}$ ), by 22%, whereas the open-circuit voltage ( $V_{OC}$ ) and the fill factor (FF), remain constant. As a result, a 22% increase in the device efficiency ( $\eta$ ) is obtained for the device with the optimum Au NPs

<sup>132</sup> E. Kymakis, E. Stratakis, E. Koudoumas, and C. Fotakis, *IEEE Trans. Electron Devices* 58, 860 (2011).

concentration of 5%. An increase at concentrations higher than 6% has negative effect on the device performance, probably due to the fact that the excessive content of the NPs may disturb the formation

	$J_{sc}$ (mA/cm <sup>2</sup> )	$V_{oc}$ (V)	FF (%)	$\eta$ (%)
Pristine	$8.27 \pm 0.12$	0.6	$53.22 \pm 0.30$	$2.64 \pm 0.05$
4 % Au	$8.90 \pm 0.20$	0.6	$61.03 \pm 0.40$	$3.26 \pm 0.09$
5 % Au	$9.77 \pm 0.24$	0.6	$63.38 \pm 0.54$	$3.71 \pm 0.12$
6 % Au	$9.60 \pm 0.15$	0.6	$61.32 \pm 0.48$	$3.53 \pm 0.08$

of P3HT and PCBM domains leading to an inhomogeneous surface morphology and to lower carrier mobility. Furthermore, it can be attributed to the occurrence of local shunts due to NPs aggregates directly bridging the ITO or Al electrode.

Table I: Photovoltaic characteristics of OPVs with various concentrations of Au NPs solutions into the photoactive P3HT: PCBM layer.

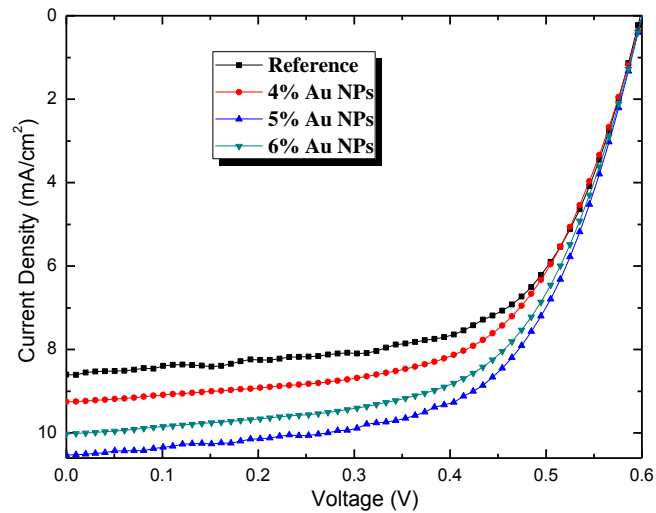
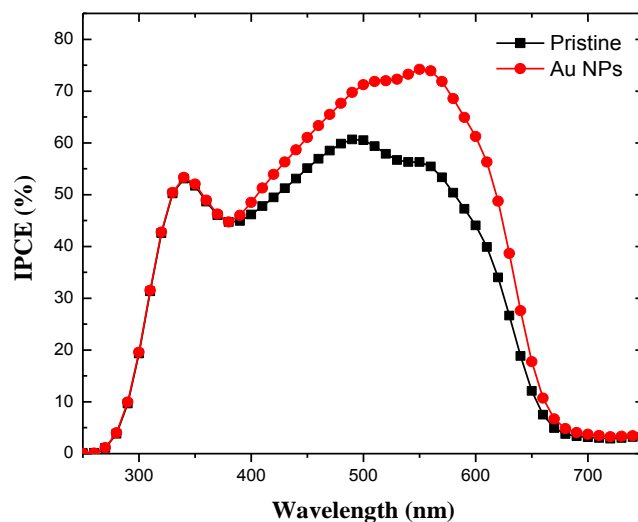


Figure 6.5 J-V characteristics of the OPV devices with Al NPs embedded in the active layer.

In order to investigate the underlying mechanism responsible to the enhanced performance of the devices, the incident photon-to-electron conversion efficiency (IPCE) curve of the device exhibited the best efficiency is measured and compared with the pristine one. As shown in Figure 6.6, the IPCE increases remarkably upon the incorporation of Au NPs, which complies with the enhanced  $J_{SC}$  observed. In particular, compared to the pristine cell, the IPCE of the device with 5% Au NPs, becomes enhanced in a broad spectral range (400 to 700 nm), while it maximizes at 570 nm. This wavelength regime practically coincides with the spectral range in which the optical absorption of the Au-NPs embedded in P3HT:PCBM medium is enhanced due to the LSPR effect and the secondary to

multiple scattering effects by the larger diameter NPs. Therefore, the performance enhancement can be also attributed to the improvement of the photoactive layer morphology due to the presence of NPs.



**Figure 6.6** Corresponding IPCE curves of the Au doped OPV devices

The use of surfactant-free NPs appears to be an efficient way to suppress exciton quenching via elimination of recombination pathways taking place on the capping layer of chemically synthesized NPs<sup>133</sup>. Besides this, the laser production method employed gives rise to a rather broad NPs distribution, so that small-sized NPs will contribute to LSPR, while higher-sized ones to multiple scattering effects, respectively.

In conclusion, it was demonstrated that the incorporation of surfactant-free Au NPs in the active layer of OPV devices can enhance the device performance by 22% due to LSPR and scattering effects. The spectral range of IPCE enhancement was found to comply with the theoretically predicted extinction spectra of Au NPs embedded in the active medium, indicating that LSPR effects are primarily responsible for the efficiency enhancement.

### Al Doped Devices

On the other hand for Al NPs doped devices, as the LSPR of Al NPs is in the UV region, the improvement of the absorption can be attributed only due to light scattering of the Al NPs. Therefore, the Al NPs can act as an effective “optical reflector” for solar light; multiple reflections will cause the light to pass through the BHJ film several times. The UV-Vis absorption spectra of the BHJ devices with Al NPs embedded in the active layer in various concentrations are shown in Figure 6.7.

<sup>133</sup> K. Topp, H. Borchert, F. Johnen, A. V. Tunc, M. Knipper, E. von Hauff, J. Parisi, and K. J. Al-Shamery, *J. Phys. Chem. A* 114, 3981 (2010).

	$J_{sc}$ (mA/cm <sup>2</sup> )	$V_{oc}$ (V)	FF (%)	PCE (%)
Reference	8.59	0.6	61	3.14
8 % Al NPs	10.60	0.6	60	3.82
9 % Al NPs	11.31	0.6	59	4.00
10 % Al NPs	10.06	0.6	58	3.50

Table II: Photovoltaic characteristics of OPVs with various concentrations of Al NPs solutions into the photoactive P3HT:PCBM layer.

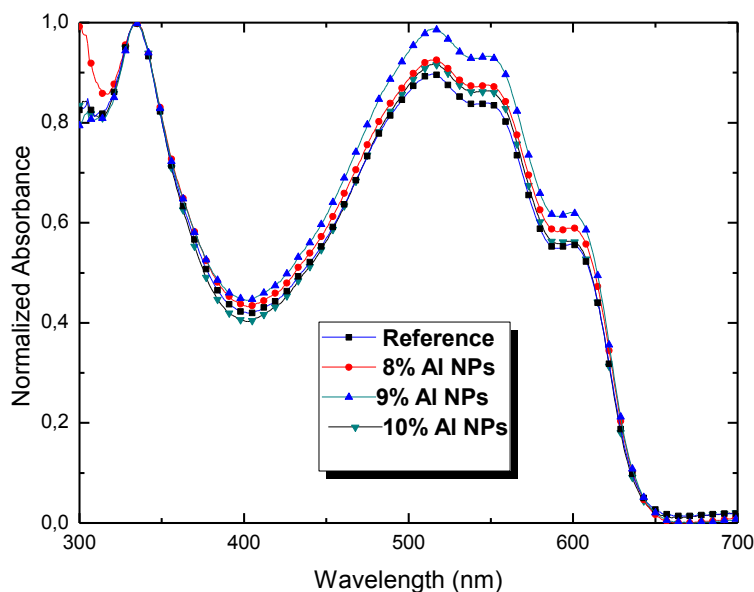
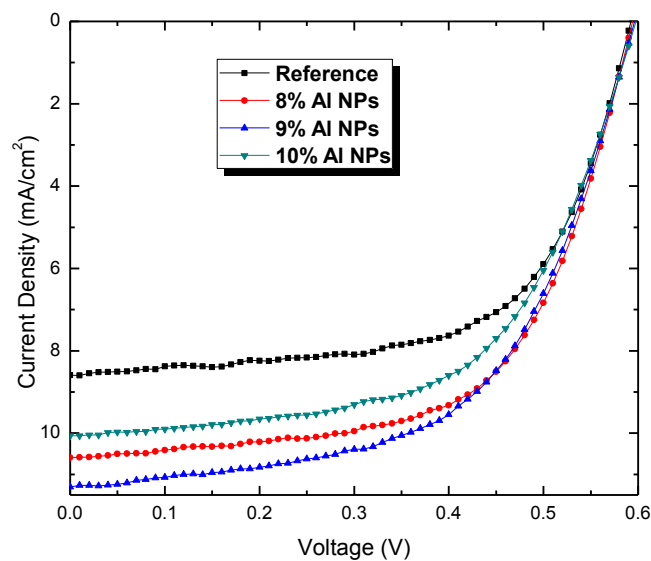


Figure 6.7 Absorption spectrum of the pristine and Al doped devices<sup>122</sup>

Moreover, it is shown that the incorporation of Al NPs in the active layer induces a significant improvement of the device short-circuit current ( $J_{sc}$ ), by 32%, whereas the open-circuit voltage ( $V_{oc}$ ) and the fill factor (FF), almost remain constant. As a result, an increase of 30% in the device efficiency (PCE) is obtained for the device with the optimum Al NPs concentration of 9 %. The optimum 9% Al NPs device exhibits a power conversion efficiency of 4.00% ( $V_{oc}=0.6$  V, short-circuit current:  $J_{sc}=11.3$  mA/cm<sup>-2</sup>, fill factor:  $FF=0.59$ ). An increase at concentrations higher than 10%, has negative effect on the device performance, probably due to the occurrence of local shunts due to degradation of the film morphology. As a result, an increase of 30% in the device efficiency (PCE) is obtained for the device with the optimum Al NPs concentration of 9 %. The respective averaged photovoltaic characteristics are summarized in Table II. Figure 6.8 displays the current voltage (J-V) characteristics of the pristine and OPV devices with different NPs fractions, under illumination with 100 mW/cm<sup>2</sup> power intensity.



**Figure 6.8** J-V characteristics of the OPV devices with Al NPs embedded in the active layer<sup>122</sup>.

In order to get an insight for the responsible mechanism to the enhanced performance of the devices, the incident photon-to-electron conversion efficiency (IPCE) curve of the device exhibited the best efficiency is measured and compared with the pristine one. As shown in Fig. 6.9, the IPCE increases remarkably upon the introduction of Al NPs, which complies with the enhanced  $J_{SC}$  observed. The pristine device exhibits a maximum IPCE of 60.66%, while the Al doped device exhibits an enhanced maximum of 72.56%. The IPCE enhancement is broad and almost uniform ranging from 400 to 650 nm, which can be directly attributed to multiple scattering by the large diameter Al NPs<sup>134</sup>. Moreover, since the insertion of Au and Al NPs produced by the same method, give rise to enhanced structural stability; it is more than possible that this will be the case in the Al NPs as well. The embedded Al NPs act as performance stabilizers, giving rise to enhanced structural stability, and therefore clarify the observed disparity between the absorption and IPCE enhancement can also be explained by structural stability. Therefore, the IPCE enhancement results from the Al NPs, from efficient light scattering and improved charge transport due to better structural stability.

<sup>134</sup> Se-Woong Baek, Jonghyeon Noh, Chun-Ho Lee, BongSoo Kim, Min-Kyo Seo & Jung-Yong Lee, *Scientific Reports*, Plasmonic Forward Scattering Effect in Organic Solar Cells: A Powerful Optical Engineering Method

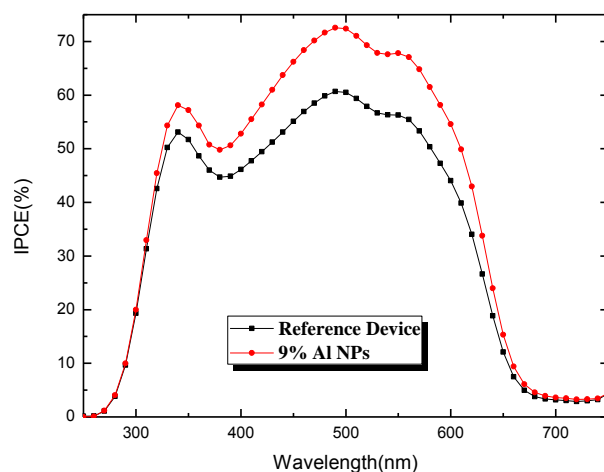


**Figure 6.9** Corresponding IPCE curves of the Al doped OPV devices<sup>122</sup>

In order to confirm that the  $J_{SC}$  is increased due to better light harvesting in the active layer, caused by multiple scattering, the diffuse reflectance of the devices was recorded. Fig. 6.10 shows the diffuse reflectance spectra of the devices fabricated with and without Al nanoparticles in P3HT/PCBM. The lower reflectivity of the devices with Al NPs in the whole spectrum clearly indicates stronger absorption of the incident light due to scattering. Hence, the P3HT/PCBM BHJ device with Al NPs (9 wt%) has a higher level of optical absorbance than the pristine P3HT/PCBM BHJ device. The scattering effect of the Al NPs increases the effective length of the optical path, which in turn increases the generation of electron–hole pairs.<sup>135</sup> This enhanced optical absorbance is directly related to the improved  $J_{SC}$  and PCE levels in the Al doped BHJ devices.

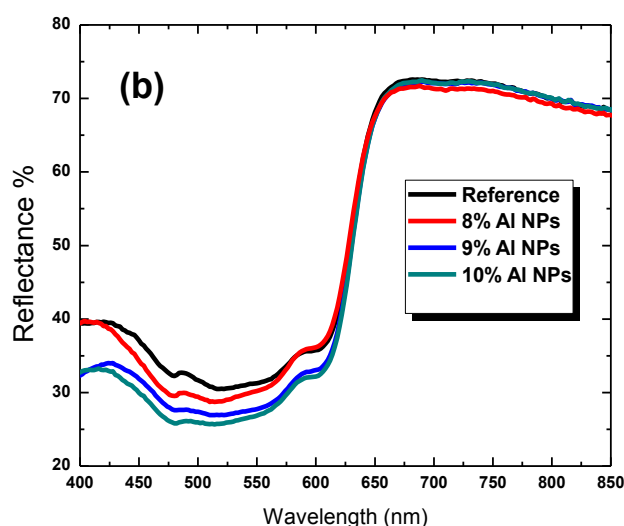


**Figure 6.10** Reflectance spectra of the devices fabricated with the addition of different concentrations of Al nanoparticles<sup>122</sup>

<sup>135</sup> D. H. Wang, K. H. Park, J. H. Seo, J. Seifert, J. H. Jeon, J. K. Kim, J. H. Park, O. O. Park, and A. J. Heeger, *Adv. Eng. Mater.* 1(5), 766–770 (2011).

To summarize, we demonstrated highly efficient plasmonic OPVs that incorporate Al NPs into the photoactive layer. In particular, the PCE was enhanced by 30% via incorporation of 30 nm Al NPs into a P3HT:PCBM based OPV device. Such efficiency enhancement is due to improved absorption caused by scattering effects due to the presence of NPs.

### The Effect of Nanoparticle on the Optical and Electrical Characteristics of Photovoltaic Cells

To further expand the potential of use Au and Al NPs in the active layer of BHJ OPVs, we investigated their impact on the prolong of the OPV devices lifetime stability when exposed to continuous solar illumination in air in comparison with the pristine devices. In order to have a better understanding of the NPs affect in the devices stability we carry out this experiment to both annealed and non annealed devices. In order to monitor the stability in conditions similar to outdoor, the experiments were performed with the devices being unencapsulated and exposed to ambient air during operation. The normalized PCE of a pristine reference, Au and Al NPs doped and annealed reference Au and Al NPs doped devices measured as a function of exposure time are shown in Fig 6.12 & 6.13. In each case a complete  $J-V$  curve is obtained Fig 6.11. Between successive measurements, devices were continuously irradiated in the open circuit mode. The respective averaged photovoltaic characteristics are summarized in Table III.

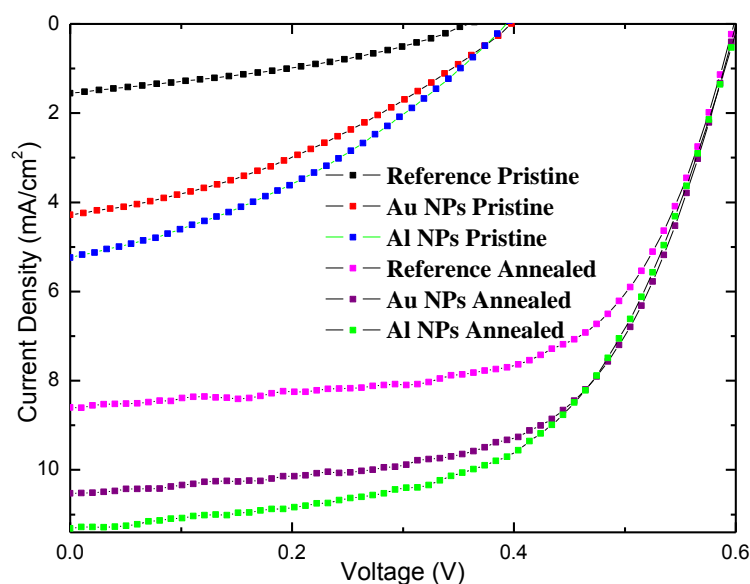
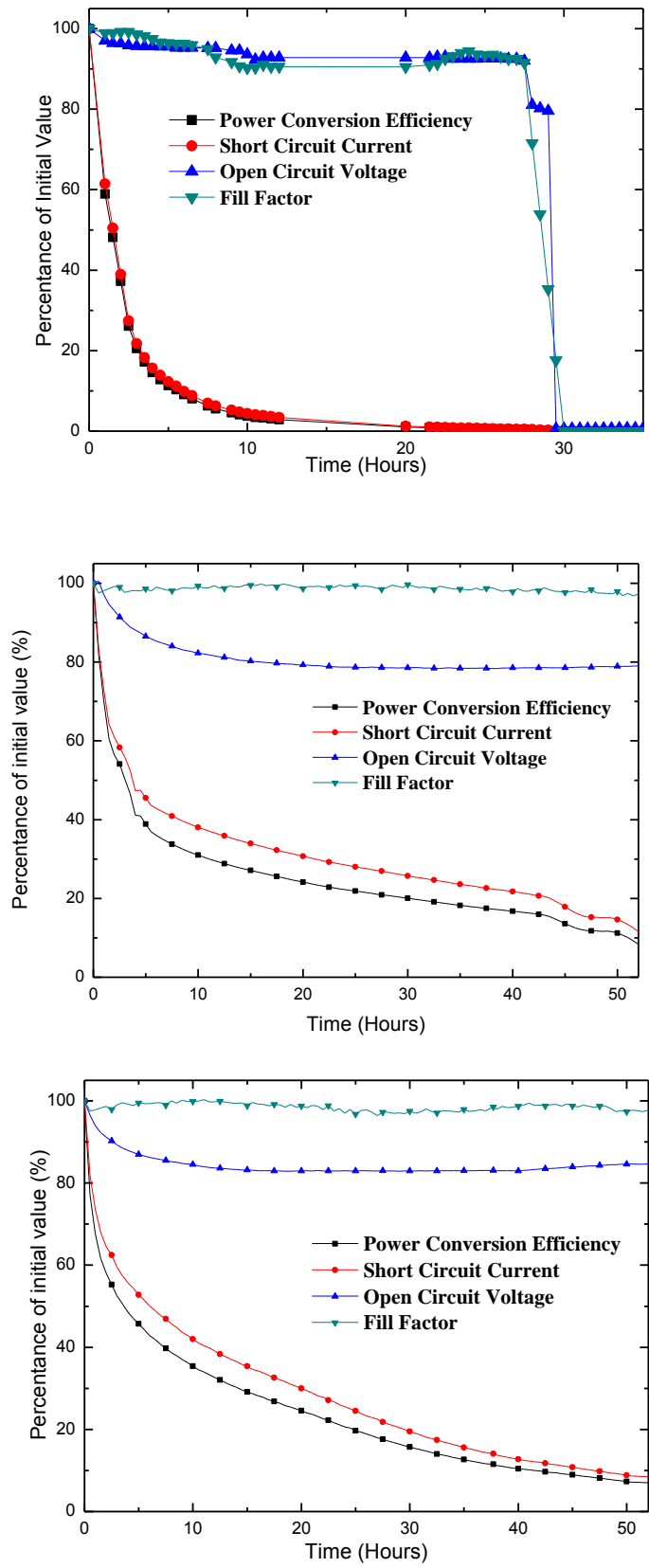


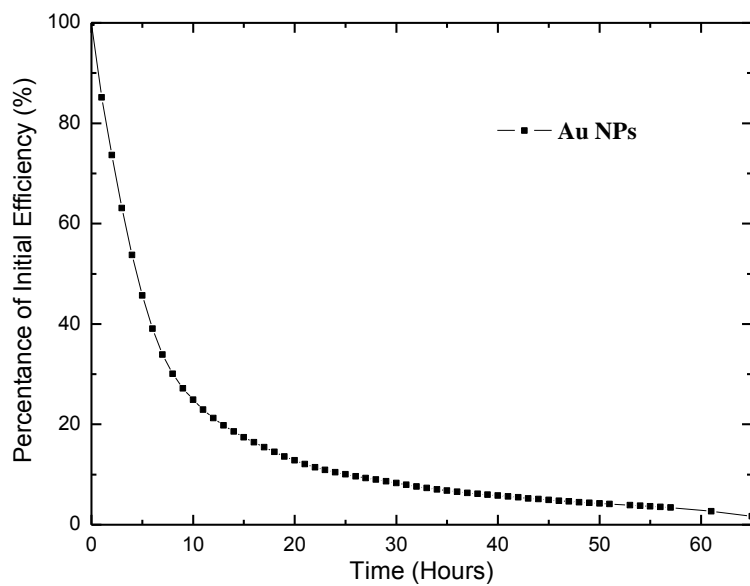
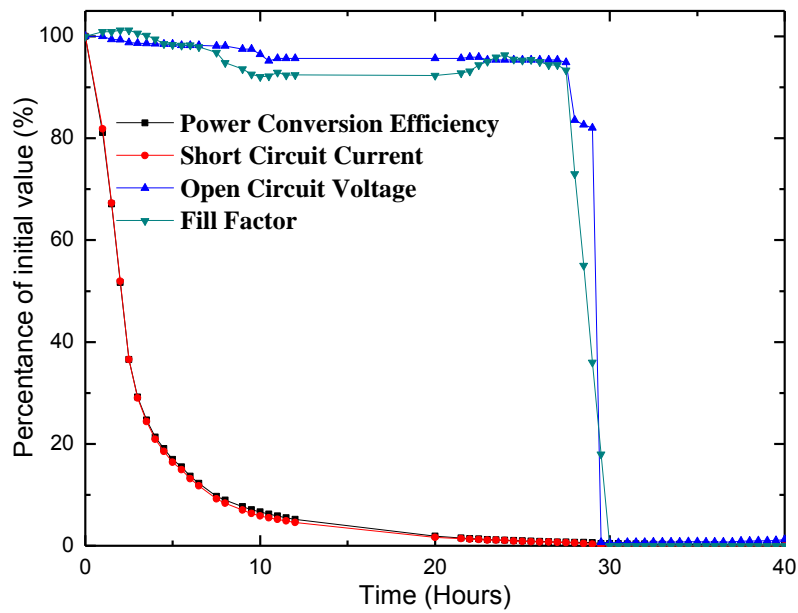
Figure 6.11 I-V curves of the annealed and non annealed devices

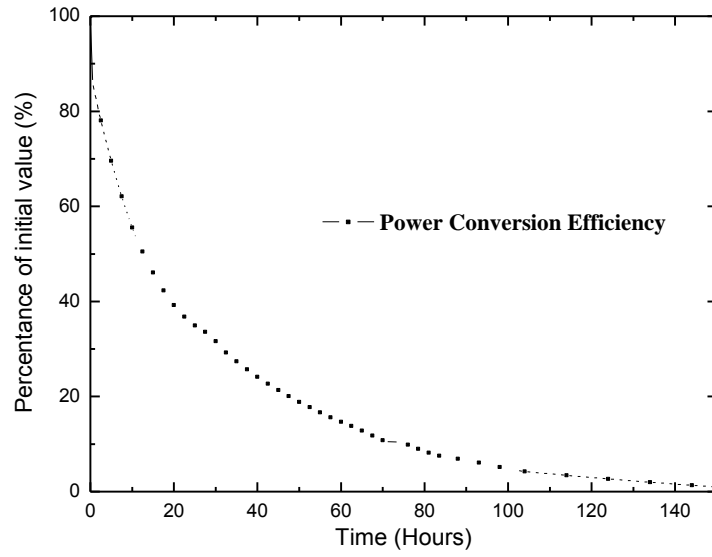


**Figure 6.12** Degradation measurements of the pristine devices: a) reference, b) Au doped, c) Al doped

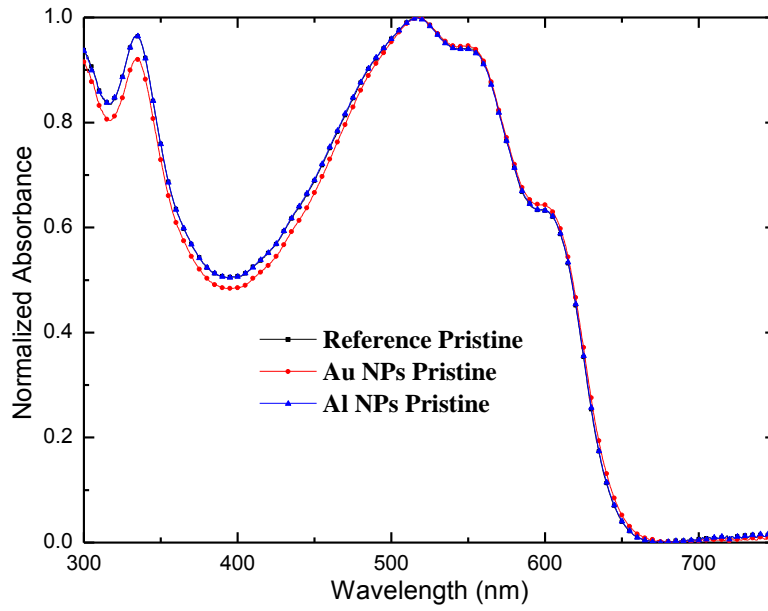
Devices	$J_{sc}$ (mA/cm <sup>2</sup> )	$V_{oc}$ (V)	FF (%)	PCE (%)
Reference Pristine	1.55	0.36	36	0.20
Au NPs Pristine	4.28	0.39	36	0.6
Al NPs Pristine	11.31	0.39	36	0.74
Reference Annealed	8.61	0.6	60	3.09
Au NPs Annealed	10.58	0.6	60	3.78
Al NPs Annealed	11.30	0.6	59	4.00

Table III: Photovoltaic characteristics of NPs doped OPVs with and without annealing process





**Figure 6.13** Degradation measurements of the annealed devices: a) reference, b) Au doped, c) Al doped



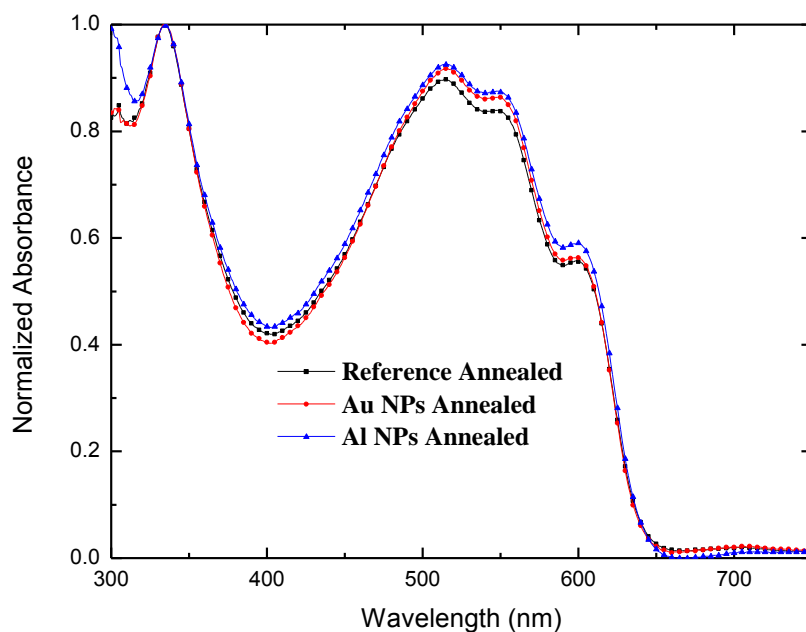


**Figure 6.14** UV-Vis of the Pristine Devices (a) and of the Annealed Devices (b)

Taking into consideration all the above results we understand that the effect of the NPs in the stability of the devices is mainly observed in the annealed devices and this is because of the crystallization of the regioregular P3HT. We can observe this crystallization from the difference in the absorption spectrum Fig 6.14 in both cases (broad shoulder in 602 nm). Due to this crystallization the annealed devices appeared to be more stable against degradation and as it is shown the incorporation of the Au and Al NPs into the photoactive layer of the devices gives rise two times the Au doped device lifetime and 5 times for the Al doped devices. On the other hand we can observe that the highest enhancement appears in the non annealed devices due to the inhomogeneous morphology of the pristine reference cell which optimized with the incorporation of the Au and Al NPs.

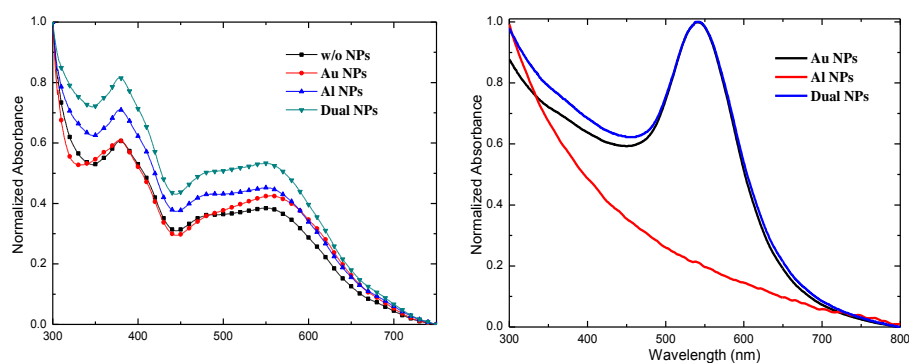
## 6.5 Incorporation of Dual metallic Plasmonic nanoparticles in PCDTBT:PC71BM active layer

In the present work, surfactant free, of various diameters, Au and Al NPs are embedded in the PCDTBT:PC<sub>71</sub>BM active layer of OPV devices to enhance device performance<sup>136</sup>. Because of the better-demonstrated stability against degradation we can easier identify the contribution of the plasmonic effect in the better device performance. Dual metallic nanostructures that are composed of

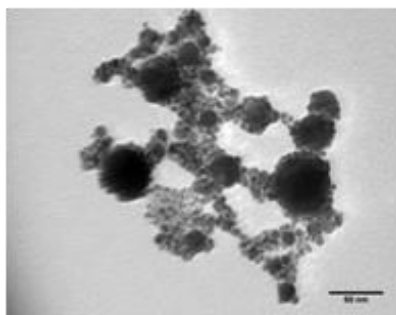
<sup>136</sup> G. Kakavelakis et. al. Chem. Comm. 50 (40), 5285 – 5287, 2014

Au NPs (for LSPR) and Al NPs (for scattering) are embedded in the active layer in order to utilize the plasmonic properties of both NPs. We have achieved a PCE of 6.12% and an enhancement of 15% for the dual doped device, a 5.76% PCE and 8% enhancement for Au doped device and 5.84% PCE and 10% enhancement for Al doped device, compared to pristine device. The active layers were fabricated by mixing respective solutions of PCDTBT and PC<sub>71</sub>BM at 1:4 ratio and Au, Al NPs, in DCB:CB (3:1) and spin-coated on PEDOT :PSS/ITO. OPV devices based on the ITO/PEDOT:PSS/PCDTBT:PC<sub>71</sub>BM/TiO<sub>x</sub>/Al structure. In all cases, the final active layer thickness, determined from cross-sectional SEM images, is measured to be (80 ± 5) nm.

Figure 6.15a shows UV-Vis absorption spectra of pristine, Au doped, Al doped and Dual doped devices. The Au doped device has a primarily enhanced absorption compared to pristine device at the wavelengths of 500-600 nm, precisely coinciding with the location of the LSPR of the AuNPs, as revealed from the Fig. 6.15b. In the case of Al doped device as the LSPR of Al NPs is in the UV region, the improvement of the absorption can be attributed only due to light scattering of the Al NPs. Therefore, the Al NPs can act as an effective “optical reflector” for solar light; multiple reflections will cause the light to pass through the BHJ film several times. As expected in the Dual doped device we observe an obvious shift to the wavelengths of 500-600 nm compared with the pristine device and across the entire spectrum we observed an obvious enhancement in the absorption which can be attributed to scattering phenomena because of the presence of the Al NPs.



**Figure 6.15** Absorption Spectrum of all the fabricated devices (left) and all the colloidal NPs solutions(right)<sup>136</sup>



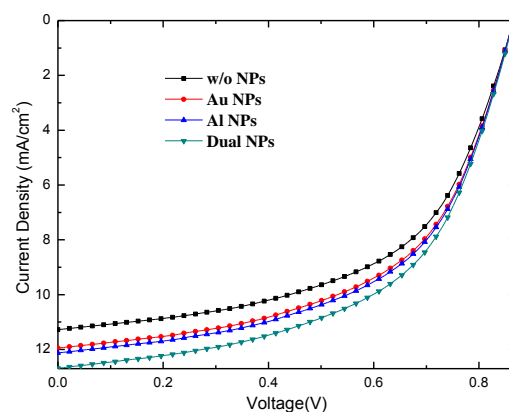
**Figure 6.16** TEM image of the Dual fabricated NPs<sup>136</sup>

Fig. 6.17 shows the current voltage (J-V) curves of the pristine and OPV devices doped with Au, Al, Dual NPs, under illumination with 100 mW/cm<sup>2</sup> power intensity. The respective averaged photovoltaic characteristics are summarized in Table IV. It is shown that the incorporation of Au NPs in the active layer induces a slight enhancement of 6% to the short-circuit current ( $J_{SC}$ ), whereas the open-circuit voltage ( $V_{OC}$ ) remain constant and the fill factor had an enhancement of 2%. The incorporation of Al NPs in the active layer induces an enhancement of 8% to the short-circuit current ( $J_{SC}$ ), whereas the open-circuit voltage ( $V_{OC}$ ) remain constant and the fill factor had an enhancement of 2%. On the other hand in case of dual doped device was observed a significant enhancement of 13% compared to the pristine device, whereas the open-circuit voltage ( $V_{OC}$ ) remain constant and the fill factor had an enhancement of 2%, and of the above we can understand that we had a combination of the plasmonic effect in this case. As a result, an increase of 15% in the dual plasmonic device efficiency (PCE) is obtained. The dual NPs device exhibits a power conversion efficiency of 6.12% ( $V_{OC}=0.86$  V, short-circuit current:  $J_{SC}=12.71$  mA cm<sup>-2</sup>, fill factor:  $FF=0.56$ ). However, the incorporation of the NPs in the PCDTBT:PC<sub>71</sub>BM photoactive layer does not give such a big enhancement in the PCE compared to our previous research<sup>23,28</sup> and this is because of the stability and durability of the PCDTBT:PC<sub>71</sub>BM against to oxygen and humidity<sup>137</sup>. The respective averaged photovoltaic characteristics are summarized in Table IV.

NPs	$J_{sc}$ (mA/cm <sup>2</sup> )	$V_{oc}$ (V)	FF (%)	PCE (%)
No	11.27	0.86	55	5.33
Au	11.95	0.86	56	5.76
Al	12.12	0.86	56	5.84
Au-Al	12.71	0.86	56	6.12

TableIV: Photovoltaic characteristics of NPs doped OPVs devices

<sup>137</sup> D. H. Wang, J. K. Kim, J. H. Seo, O. O. Park, J. H. Park, *Solar Energy Materials & Solar Cells* 2012, **101**, 249–255



**Figure 6.17** I-V curves of all the fabricated devices<sup>136</sup>

In order to get an insight for the responsible mechanism to the enhanced performance of the devices, the incident photon-to-electron conversion efficiency (IPCE) curve of the dual NPs device is measured and compared with the pristine one. The pristine device exhibits a maximum IPCE of 68.90%, while the Dual doped device exhibits an enhanced maximum of 81.34%. As shown in Fig.6.18, the IPCE enhancement is broad and almost uniform ranging from 400 to 700 nm, which can be directly attributed to multiple scattering effects by the large diameter Al NPs<sup>138</sup>. The IPCE increases remarkably upon the introduction of Au and Al NPs, which complies with the enhanced  $J_{SC}$  observed. This can be mainly attributed to scattering effects as the enhancement in the IPCE spectrum is broad and uniform. As the Al NPs plasmon resonance is in the UV region of the solar spectrum this enhancement can be attributed to scattering effects. On the other hand, the enhancement caused by Au NPs is a contribution of scattering effects and LSPR. Au NPs form clusters bigger than ~40nm as we can observe from the TEM image so we can presume that scattering effects takes place. Also as the plasmon resonance of the ~10nm Au NPs is in ~510nm LSPR effect takes place. It can be confirmed from the shift of the peak in the IPCE curve to 510nm in the dual doped device. So, we can conclude that we have a synergetic effect of LSPR and scattering from Au and Al NPs.

<sup>138</sup> S.W. Baek, J. Noh, C.H. Lee, B.S. Kim, M.K. Seo and J.Y. Lee, *Scientific Reports*, 2013, **3**, 1726

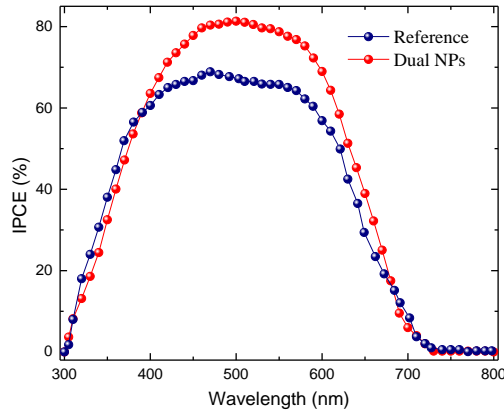


**Figure 6.18** IPCE curves of the OPV devices<sup>136</sup>

In order to confirm that the  $J_{SC}$  is increased due to more light harvesting in the active layer, caused by multiple scattering effects due to Al NPs and LSPR due to Au NPs, the diffuse reflectance of the devices was recorded. Fig. 6.19 shows the diffuse reflectance spectra of the devices fabricated with Au, Al and dual nanoparticles in PCDTBT:PC<sub>71</sub>BM photoactive layer. The lower reflectivity of the devices with NPs in the whole spectrum clearly indicates stronger absorption of the incident light due to scattering. The scattering effect of the Al NPs increases the effective length of the optical path, which in turn increases the generation of electron–hole pairs<sup>183</sup>. This enhanced optical absorbance is directly related to the improved  $J_{SC}$  and PCE levels in the Al doped BHJ devices. Also in the Au doped devices we observe a lower reflectivity compared to the pristine device but on the other hand reflectivity is lower compared the Al doped device and dual doped device and this is because of the smaller particle diameter compared to Al NPs.

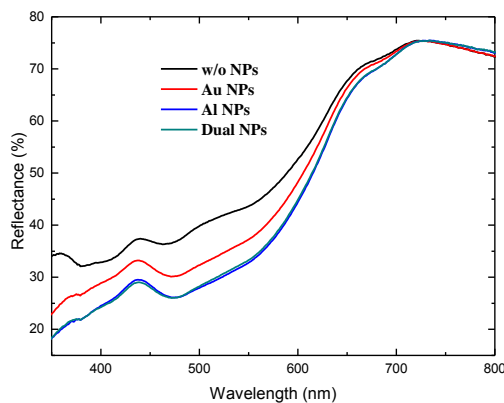


**Figure 6.19** Reflectance spectrum of all the fabricated devices<sup>136</sup>

To conclude we propose and demonstrate a novel way to trap the incident light into the photoactive layer of a plasmonic OPV device in order to enhance the absorption and hence the power

conversion efficiency of the devices. To accomplish this enhancement we incorporate small diameter Au NPs (for LSPR) and large diameter Al NPs (for scattering) into the PCDTBT:PC<sub>71</sub>BM to take advantage simultaneously of both plasmonic effects.

## 6.6 In Situ Spectroscopic analysis of performance stability of Al NPs doped devices

Using complementary analytical techniques for in-situ studies, in this section we have explored the underlying mechanisms behind the observed stability improvement in the case of P3HT:PCBM and PCDTBT:PC<sub>71</sub>BM BHJ blends. In particular, Laser Induced Fluorescence (LIF), Photoluminescence decay and Fourier Transform InfraRed (FTIR) spectroscopy experiments were performed and complemented with device degradation electrical measurements.

The J-V characteristics of the pristine and Al doped devices are summarized in chapter 6.4 for P3HT and in 6.5 for PCDTBT based devices. Following the fabrication and initial measurement of photovoltaic characteristics, the stability of the devices (in optimum conditions) against degradation is measured via performing successive J-V recordings. In order to simulate outdoor conditions, the degradation experiments were performed with the devices being unencapsulated and exposed to ambient air during operation. Results are presented for two different measurement procedures related to sample storage conditions among measurements. In particular, between two successive J-V recordings, devices were either stored in the dark or were continuously illuminated in the open circuit mode. Figures 6.20(a) and 6.20(b) depict the evolution of the respective normalized PCEs (aging curves) over exposure time for the reference and Al NPs-doped devices following continuous operation under illumination. For each data point of the curves, a complete J-V characteristic was recorded and PCE values were subsequently calculated. It is clear that for both BHJ systems PCE can be better preserved due to the presence of Al NPs. Indeed, for the P3HT:PCBM and P3HT:PCBM:Al NPs active layers 2.5 and 13.5 hours of continuous illumination are required for a 50% reduction of PCE with respect to its initial value. The situation is similar for the PCDTBT:PCBM and PCDTBT:PCBM:Al NPs systems required 14.5 and ~45 hours respectively for the same PCE reduction to be attained. The above results indicate that incorporation of Al NPs into the BHJ active layer significantly mitigates performance deterioration due to photodegradation. On the contrary, as depicted in Figure 6.20(c), there is practically no difference in the corresponding PCE evolutions between the reference and Al NPs doped P3HT:PCBM-based devices stored in dark. Similar observations were made for the device hosting a PCDTBT:PC<sub>71</sub>BM active layer (not shown). It can be concluded that the observed stability enhancement phenomenon takes place only under

illumination, suggesting that Al NPs strongly affect the OPVs photodegradation pathways<sup>139</sup> while their effect is not related to ageing mechanisms occurring in the dark<sup>140</sup>.

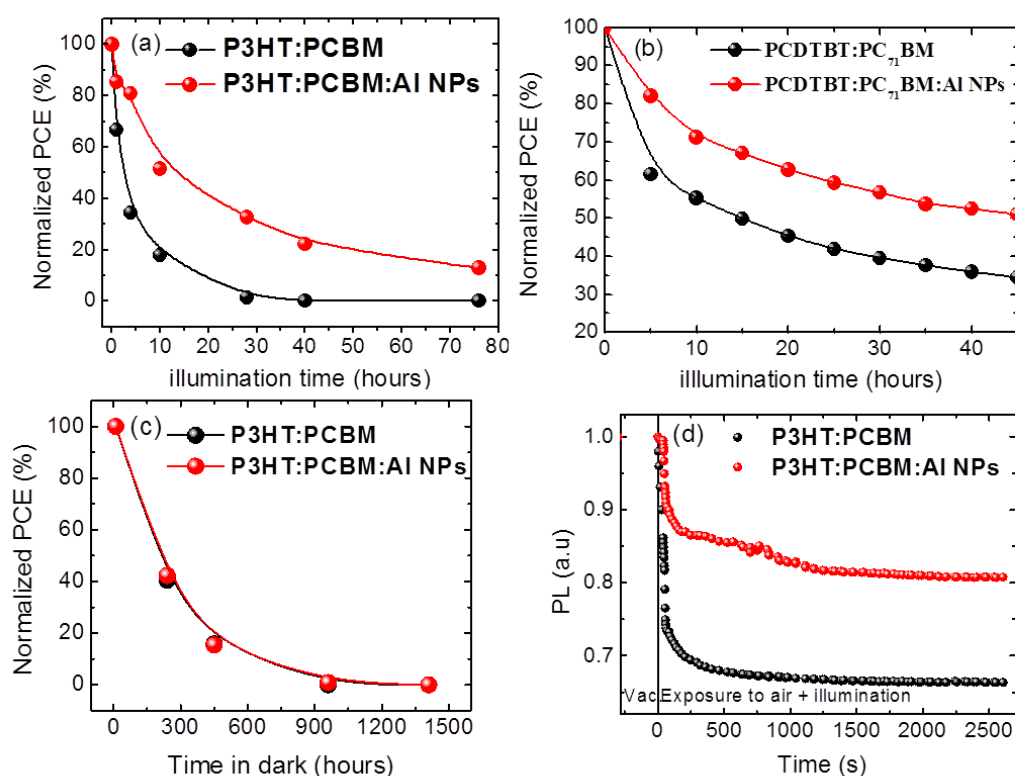


**Figure 6.20** Normalized PCE values vs. illumination time for the reference and Al NPs-doped OPV devices using the P3HT:PCBM (a) and PCDTBT:PC<sub>71</sub>BM BHJ blends (b). The respective PCE dependence on dark storage time for the P3HT:PCBM based devices is shown in Figure (c); (d) Photoluminescence decay of reference (black spheres) and Al NPs doped (red spheres) P3HT:PCBM based devices

In order to probe the underlying mechanism behind the observed effect of Al NPs against photodegradation, we have proceeded to optical spectroscopy studies of the pristine and doped P3HT:PCBM blends. The reason is that it is the best characterized BHJ system, but more importantly it is highly reproducible, thus enables a quantitative spectroscopic study. In a first step, we have considered, based on the above results, that the presence of Al NPs may hinder the process behind photoinduced oxidation of the conjugated polymer component in the blend<sup>141</sup>. As presented in Scheme 1, during photo-oxidation of semiconducting polymers, singlet oxygen, formed via energy transfer

<sup>139</sup> Paci, B.; Generosi, A.; Rossi Albertini, V.; Perfetti, P.; de Bettignies, R. The Role of C60 Barrier Layer in Improving the Performances of Efficient Polymer-Based Photovoltaic Devices: An AFM/EDXR Time-Resolved Study *J. Phys. Chem. C* 2009, 113, 19740

<sup>140</sup> Grossiord, N.; Kroon, J.; Andriessen, R.; Blom, P.; Degradation Mechanisms in Organic Photovoltaic Devices *Org. Electron.* 2012, 13, 432–456

<sup>141</sup> Lim, Y. T.; Lee, T.-W.; Lee, H.-C.; Park, O.O. Impediment of Photo-Oxidation in PPV Nanocomposites Doped by Metal Coated Silica Nanoparticles *Synthetic Met.als* 2002, 128, 133-137

from the polymer triplet exciton, reacts with the polymer to generate exciton traps (paths 6a and b in Figure 6.21).

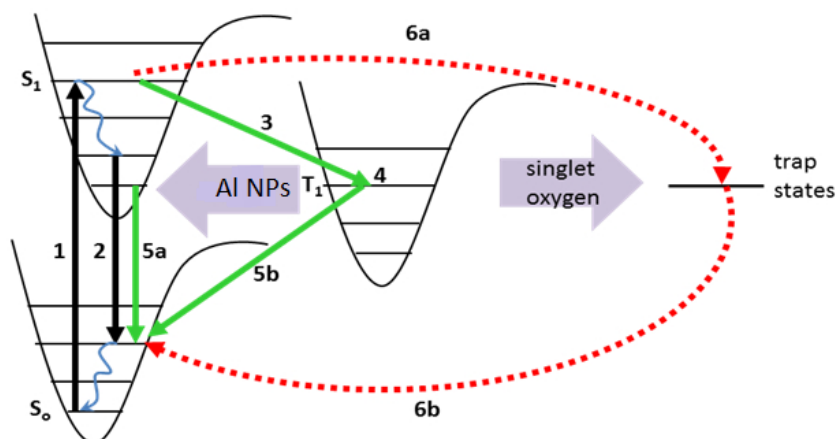


**Figure 6.21** Schematic of the photo-oxidation process in polymer: Al NPs active layer. Energy from the polymer triplet excitons excites singlet oxygen, which reacts with the polymer chains to form exciton trap states. The Al NPs embedded into the blend act as quenchers of the triplet excitons and in this way the photooxidation process can be impeded. 1: Absorption; 2: Luminescence 3: System Intercrossing; 4: Triplet State; 5a: Fluorescence; 5b: Triplet quenching; 6a, 6b: Exciton recombination via trap states. This process is limited in the presence of a triplet quencher.

Such traps are topological defects comprised of carbonyl groups formed on the ends of polymer chains and provide an additional nonradiative channel for the polymer singlet excitons. As a result, quenching of polymer luminescence is induced. In Donor:Acceptor (D:A) blends, the charge transfer from polymer to fullerene is the dominant process and therefore it partially prevents intersystem crossing to a triplet state. Under certain conditions, the formation of triplets in polymer:fullerene blends is also possible as it depends on the relative energy positions of polymer triplet excitons and the fullerene LUMO level. Formed triplet excitons located on the polymer can then nonradiatively relax to the ground state. Additional reactions emerge upon introduction of molecular oxygen, which has a triplet ground state configuration ( $3O_2$ ). The polymer triplet excitons can undergo energy transfer to the triplet oxygen to generate excited singlet oxygen ( $1O_2^*$ ). It can be concluded that the mechanisms described in Scheme 1 are valid and present in polymer:fullerene blends as well. In the present case Al NPs may play the role of a stabilizer that blocks the action of oxygen. In particular, as shown in Scheme 1, we postulate that the triplet excitons may be quenched as a result of the overlap of their energy levels with the plasmon resonance of the embedded Al NPs (paths 3,4,5b in Figure 6.21).

To investigate this possibility, PL decay measurements, which are a proper mean to quantify singlet quenching in P3HT under oxygen exposure, were performed. Figure 6.20d presents the results for the reference compared to the Al NPs-doped blend. These measurements correspond to

the evolution of the first emission peak values, at 635 nm, following laser excitation at 325 nm. It is clear that the addition of NPs into the blend significantly retards its PL intensity decay rate. Indeed, the absorption spectrum of Al NPs in ethanol comprises a characteristic broad peak corresponding to the NPs' plasmon resonance. This peak centers at ~340 nm, however it is expected to be substantially red-shifted when the NPs are embedded into the higher-refractive index, compared to ethanol, polymer matrix. Such redshift combined with the broadband nature of NPs' absorption peak may give rise to partial overlap with the triplet excitons band lying in the range [800-1300] nm for both polymer donor systems used in this study. Considering that the NPs resonance has an excitation lifetime of a few picoseconds, the donor-acceptor interaction between the comparatively long-lived triplet excitons of P3HT and the Al NPs will result in a strong quenching of the triplet state and, thus, the photo-oxidation rate. Alternatively, the photoexcited excitons are highly mobile along the conjugated polymer backbone and may hop between chains towards lowest-energy areas of the film. It is possible that the Al NPs dispersed in the polymer blend will give rise to variations in the local energy environment of the triplet excitons, attracting them towards Al NPs, where the triplet exciton-Al NPs interaction can easily take place. Specifically, as the size of particles decreases to the nanometer scale, the surface area of the particles increases dramatically, and the NPs act as an effective scavenger of the polymer triplet state.

In order to further study the degradation process, fluorescence experiments were additionally performed. For this purpose reference and Al NPs doped devices were submitted to long-term degradation process in air and the decay of their fluorescence signal was recorded both under dark storage and during illumination (three pairs of samples for each case). In this way it was possible to discriminate the aging processes related to light exposure from those due to ambient environment only (air). Moreover, we were able to examine the contribution of the Al NPs to the photovoltaic effect and the stability of the device. The collected fluorescence spectra are presented in Figure 6.22, while Figure 6.23 compares the normalized fluorescence intensity, calculated using the peak values of such spectra, at 635 nm, following laser excitation at 532 nm, as a function of the dark storage and illumination times respectively. As can be seen in Figure 6.23b, the fluorescence signal of the reference device degrades rapidly upon illumination, following a first order exponential decay. On the contrary, the Al NPs based device is more stable under illumination, especially in the first 10 hours of illumination where the PCE photodegradation rate is significant (Figure 6.20c). In this case the fluorescence decay is well fitted by a sigmoidal curve, indicating the fluorescence decay mitigation effect. On the contrary, there is no evidence of any mitigation effect when the same blends are monitored, while the samples were stored in dark in ambient air (Figure 6.23a). These results are in accordance with the PCE degradation experiments presented in Figure 6.20 and further confirm the

NPs mediated preservation effect of the polymer optical properties, evident only under prolonged illumination.

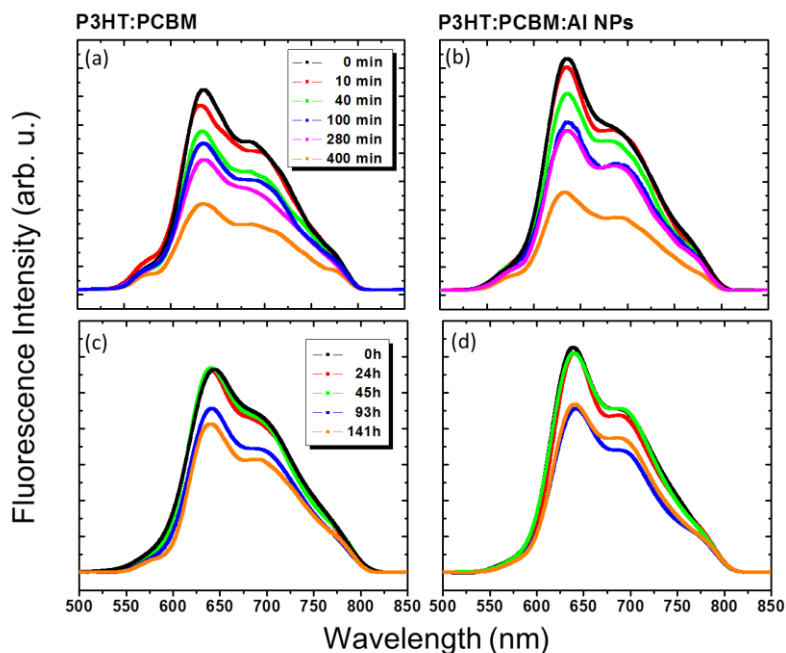


**Figure 6.22** Laser induced Fluorescence spectra of: reference (a) and AI NPs-doped devices (b) after illumination at certain time intervals shown in the inset, reference (c) and AI NPs-doped (d) devices stored in dark. Excitation wavelength at 532 nm, Nd:YAG ns laser.

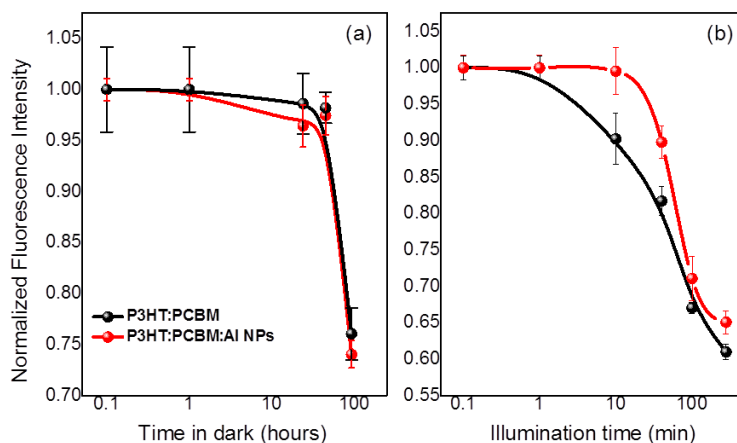


**Figure 6.23** (a) Normalized fluorescence decay of reference and AI NPs doped devices stored in the dark. (b) Normalized fluorescence decay of reference and AI NPs doped devices that were illuminated at certain time intervals. Excitation wavelength at 532 nm, Nd:YAG ns laser. The normalized values corresponding to the peak emission wavelength at 635 nm are plotted.

The different dynamics observed for the fluorescence decay signal between light and dark conditions imply the presence of two separate degradation pathways affecting the BHJ system. Our results above suggest that incorporation of AI NPs affects only the pathway under light exposure. To further explore

these phenomena, FTIR spectroscopy is used providing an insight on the chemical bonding changes taking place under illumination or dark storage of the reference and Al NPs doped devices.

As shown in Figure 6.24, the FTIR spectra of the reference and Al NPs devices in its pristine state exhibit remarkable differences. In particular, the reference device shows a broad band at  $1530\text{ cm}^{-1}$ , being the convolution of the two resonant quinoidal and benzoic structures of the thiophene ring in PEDOT, which are equally represented in the as-deposited film. This broad band also includes the C=C stretching of P3HT aromatic ring positioned at  $1515\text{ cm}^{-1}$ . In the pristine state of the Al NPs doped sample, however, two sharp and distinct bands are evidenced at  $1515\text{ cm}^{-1}$  and  $1548\text{ cm}^{-1}$  respectively. This may be an indication that the Al NPs interfacing the PEDOT:PSS buffer layer could modify the balance between the two resonant structures of PEDOT and consequently its packing structure. Furthermore, the band at  $(1292\text{-}1314)\text{ cm}^{-1}$  in the reference sample red shifts towards  $1263\text{ cm}^{-1}$  in the Al NPs doped sample. This region is generally associated to the acyl- or phenol- C-O stretching corresponding to the ethylene-dioxy group in PEDOT. The red shift is a further hint of a structural rearrangement occurring in the buffer layer due to Al NPs doping. Finally, in the reference sample the following PSS characteristic bands are visible: asymmetric S-O stretching vibrations at  $1120\text{ cm}^{-1}$  and S=O stretching due to  $\text{SO}_3^-$  band at  $1388\text{ cm}^{-1}$ . These bands are red shifted towards  $1059\text{ cm}^{-1}$  and  $1330\text{ cm}^{-1}$  respectively, in the Al NPs doped system. The latter band is a shoulder convolved to the stronger ethylene-dioxy signal. The above observations comply with partial Al NPs diffusion at the active layer/buffer layer interface, causing modification of the PEDOT:PSS chain motion.

Figures 6.24b and c presents the FTIR data for reference and NPs based layers following dark storage for three weeks in air. A general observation is that the characteristic bands intensities decrease after storage, indicating degradation of the buffer layer. For the reference system, the bands showed the most remarkable modifications are discussed in the following. First, there is a red shift of the C=C stretching thiophene ring vibration from  $1530\text{ cm}^{-1}$  to  $1515\text{ cm}^{-1}$ , the final value almost approaching the characteristic band of pure P3HT, while a less intense band at  $1548\text{ cm}^{-1}$  is detected after dark storage. This is an indication that exposure to ambient conditions has modified the balance between the resonant quinoidal and benzoic structures of the thiophene ring in PEDOT, characterizing the as-deposited films. As a result, the (less conductive) benzoic contribution of PEDOT becomes dominant over the quinoidal (conductive) one. An additional spectrum modification is related to the band including the  $1292$  and  $1314\text{ cm}^{-1}$  modes red shifting towards  $1270\text{ cm}^{-1}$ . This region is associated to the ethylene-dioxy group in PEDOT and the red shift observed implies structural rearrangement occurring during ambient storage. In addition, the PSS characteristic bands at  $1118\text{ cm}^{-1}$  (asymmetric

S-O stretching vibrations) and at  $1388\text{ cm}^{-1}$  (S=O stretching due to  $\text{SO}_3^-$ ) are strongly reduced, indicating that PSS modification occurs upon dark storage, possibly due to ambient moisture (PSS is highly soluble in water). Such degradation may affect the bond between  $\text{SO}_3\text{H}$  group and the insulating chains of PSS, inducing a reduced interaction between PEDOT and PSS.

Similar to the reference sample, sample the band intensities of the FTIR spectrum of Al NPs doped system decreased after storage (Figure 6.24c) indicating degradation of both the structure of the PEDOT:PSS and P3HT polymeric components. However, on the contrary to the reference system, the characteristic peaks of PEDOT and P3HT were not shifted. The only remarkable effect is the suppression of the PSS characteristic bands at  $1059\text{ cm}^{-1}$  and at  $1263\text{ cm}^{-1}$ , suggesting that the contribution to buffer layer degradation is limited to its hygroscopic component as a consequence of exposure to ambient moisture.

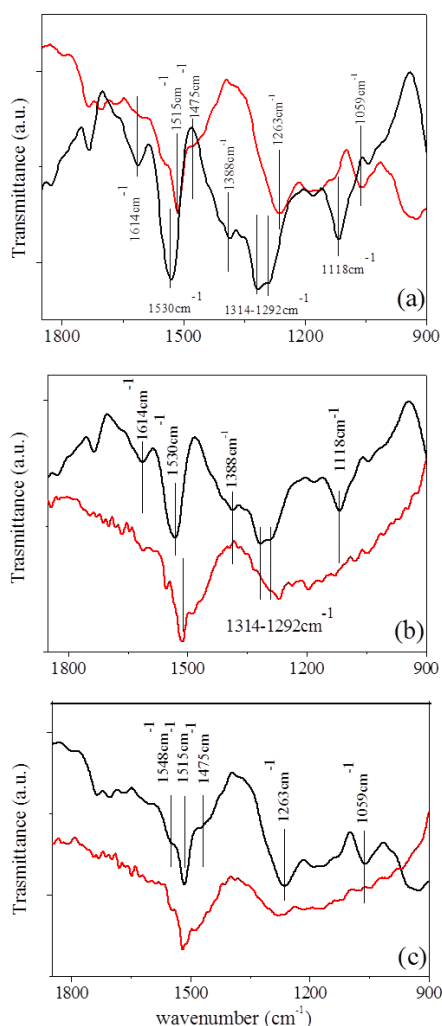


**Figure 6.24** (a) FTIR measurements of pristine samples; Reference sample: black line; AlNPs sample: red line. FTIR measurements of reference (b) and (c) Al-doped devices; black line: pristine state, red line: dark storage state.

The comparison of the FTIR spectra of the reference sample in its pristine vs illuminated states, presented in Figure 6.25, does not evidence any shift of the buffer layer vibrational bands, indicating that the PEDOT:PSS layer remains stable upon light exposure. However, there is a prominent decrease of the  $1530\text{ cm}^{-1}$  peak intensity, attributed to both PEDOT and P3HT. However, since no variation was observed for the rest of PEDOT and PSS vibrational modes, we may assume that the  $1530\text{ cm}^{-1}$  intensity loss is a fingerprint of P3HT photo oxidation, as previously reported in the literature. Further information of the BHJ degradation under light exposure can also be deduced from the strong reduction of the band at  $1190\text{ cm}^{-1}$ , related to C-C-O stretching in PCBM. This suggests that illumination may favour diffusion of the water molecules into the BHJ and PCBM esters hydrolysis spontaneously occurs. This is also confirmed by the appearance of the broad band at  $3550\text{ cm}^{-1}$  (inset of Figure 6.25a), which is the spectral marker of the stretching mode of (OH) groups (being alcohol the secondary product of the ester hydrolysis). On the contrary, the FTIR bands of the NPs doped system remains unchanged after prolonged illumination. Only a band intensity decrease was observed, indicating a general degradation of the structure of the PEDOT:PSS and P3HT polymeric components. The above data suggest that no structural modifications occur in the Al NPs doped system upon prolonged illumination.

Summarizing the FTIR results, we can state that the following aging processes are evidenced under dark storage of the reference sample: PEDOT degradation (favouring of a less conductive structure) and PSS modification. The former process is inhibited when Al NPs are introduced in the BHJ and only PSS modification, related to its hygroscopic nature, persists. This effect may be due to the presence of some Al NPs in contact with the hole transporting layer that may hinder the PEDOT:PSS chain motions leading to an effective increase of the conformational stability. It should be mentioned here that the identical dark lifetime degradation measured for both types of cells, namely reference and Al NPs doped, indicate that the dark IV characteristics may not be sensitive to such changes in the PEDOT:PSS structure. This is in accordance to the literature, stating that the dark current is typically not a figure of merit of solar cell devices. Conversely, all aging processes evidenced in the reference sample under illumination, are inhibited upon incorporation of Al NPs into the BHJ blend.

The FTIR results complemented with the PL and fluorescence studies presented above provide us with important information on the different degradation pathways occurring upon illumination. In particular, our results show that P3HT photo-oxidation, which is the primary pathway, is significantly mitigated in the Al NPs doped OPV cells possibly due to the reason that Al NPs function as triplet quenchers (Figure 6.21). Besides this, a second degradation pathway present upon illumination is related to PCBM hydrolysis, which gives rise to the creation of trap states acting as fluorescence quenchers and thus influence exciton generation. We postulate that solar illumination could mediate

the formation of an aluminium-oxide ( $\text{Al}_2\text{O}_3$ ) coating on the NPs surface. In particular, due to exposure to air and moisture conditions, water molecules diffusing in the BHJ will react under illumination with the NPs surface leading to  $\text{Al}_2\text{O}_3$  corrosion, which is well known as a spontaneous reaction process. Such process is facilitated by the absence of any surfactant coating on the Al NPs surface, since the NPs used here were produced by a physical synthetic method. As a result of this process, the availability of water molecules promoting PCBM hydrolysis is limited. Finally the third aging process identified by FTIR analysis is associated to a degradation of the PEDOT:PSS layer. This aging pathway is always present upon exposure to air, while the presence of Al NPs at the active layer/buffer layer interface partially influences the PEDOT:PSS chain motion.

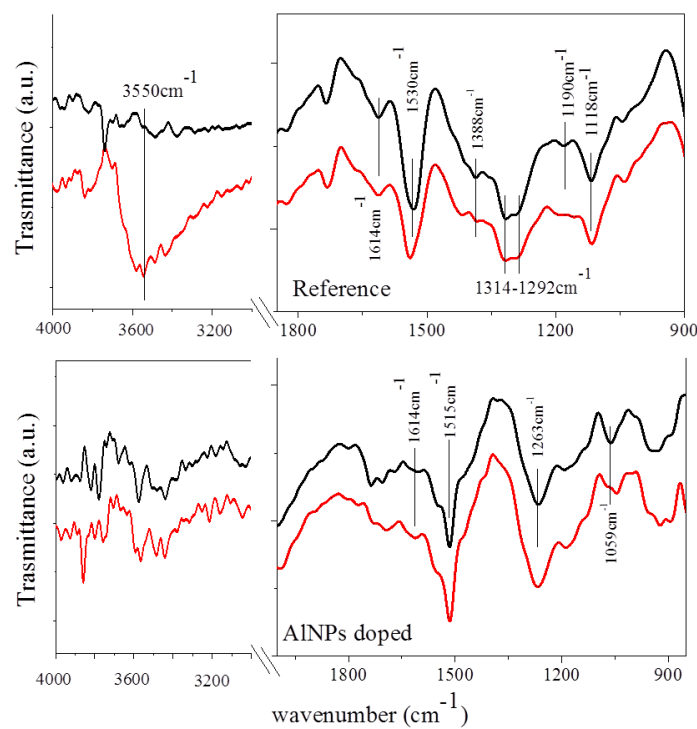


**Figure 6.25** FTIR measurements of reference (top) and Al-doped devices (bottom); black line: pristine state, red line: illuminated state.

Wavenumber (cm <sup>-1</sup> )	Functional group
1059	-SO <sub>3</sub> <sup>-</sup> sym. stretch.
1118	S-O asym. stretch.
1190	C-O stretch. in esters
1263	Red shift of 1292 vibration
1292-1314	C-O stretch. Ethilendioxy group
1388	S=O stretch.
1475	Red shift of 1515
1515	C=C sym. Stretch. in aromatic
1530-1548	Tiophene stretch.
1614	C=C asym. Stretch. in aromatic
3550	O-H stretch.

Table V Vibrational modes corresponding to the wavenumbers labeled in Figures 6.24 and 6.25

We have reported on a remarkable enhancement of OPV devices lifetime upon incorporation of Al NPs into the BHJ active layer. This significant improvement in stability of the devices is presented for two different, widely used, BHJ systems. FTIR complemented with PL and fluorescence spectroscopy measurements revealed the mitigation of two different photodegradation pathways attributed to the presence of Al NPs. Firstly, NPs incorporation blocks the polymer donor photooxidation via oxygen-assisted formation of triplet excitons, possibly due the overlap of such excitonic levels with the plasmon resonance of the embedded Al NPs. Secondly, it inhibits the PCBM hydrolysis, possibly due to the light mediated corrosive reaction with water molecules leading to Al<sub>2</sub>O<sub>3</sub> surface layer formation. This work proposes the application of Al NPs doping as an efficient way to enhance the lifetime of other types of polymer devices as well, including light emitting diodes, detectors and sensors.

## 6.7 The role of nanoparticles ligand coating

In order to have an insight for the NPs and their surrounding environment, we demonstrate strong evidence of the critical importance of the NPs ligand shell on the device performance<sup>142</sup>. In particular, we have shown that the plasmonic effect accountable for the performance enhancement takes place only in the case, in which the NPs core is in direct contact with the active layer polymer donor. This can be achieved with the utilization of ligand-free NPs or NPs

<sup>142</sup> E. Kymakis et al. ACS Photonics, 2 (6), 714, 2015

terminated with the same polymer donor as the active layer. On the contrary, devices with ligand-terminated Au NPs show lower performance, even compared with the pristine device due to the deteriorated active layer morphology attained, which leads to exciton quenching. All the experiments were performed using the P3HT as electron donor material since one of the ligands used in this work was P3HT polymer and as electron acceptor material was used the well studied PCBM fullerene derivative in the case of air processed OPVs and ICBA fullerene derivative with optimized energy levels (shifted lowest unoccupied molecular orbital by 0.17eV towards the vacuum level) in the case of high efficient OPVs processed under inert atmosphere.

Initially, gold nanoparticles synthesized by the Brust method<sup>143</sup> and coated with tetraoctyl ammonium hydroxide (Au:TOAB) were incorporated in both BHJ systems as light-harvesting components. In such polymer-nanoparticle blends, although the light absorption was monotonically increased with incorporating increasing amounts of metal NPs into the active layer, at the same time the short circuit current ( $J_{sc}$ ), open circuit voltage ( $V_{oc}$ ) and fill factor (FF) of the ensuing devices monotonically decreased (results not shown). The observed decrease can be attributed to the NPs acting as recombination centers within the device, in essence creating internal short-circuits throughout the photoactive layer.

To further examine the influence of plasmonic NPs on OPV device performance and clarify the observed Au:TOAB NPs deterioration effect, incorporation of two additional NPs types were investigated; a) surfactant-free, ion-terminated Au NPs prepared by physical synthetic means and b) P3HT-terminated Au NPs (Au:P3HT). Both NPs types (made chemically and by ablation) exhibit similar size distributions. Practically both systems allow direct contact of NPs with the active layer components and potentially improved exploitation of the plasmon absorption enhancement process. At the same time, the different termination coatings among the three types of NPs used enable the investigation of the effect of ligand molecules on plasmonic enhancement. Figure 6.26 presents a schematic of the different OPV cells set up discussed in this work.

---

<sup>143</sup> Brust, M.; Walker, M.; Bethell, D.; Schiffrin, D. J.; Whyman, R. Synthesis of thiol derivatised gold nanoparticles in a two-phase liquid/liquid system. *J. Chem. Soc., Chem. Commun.* 1994, 801.

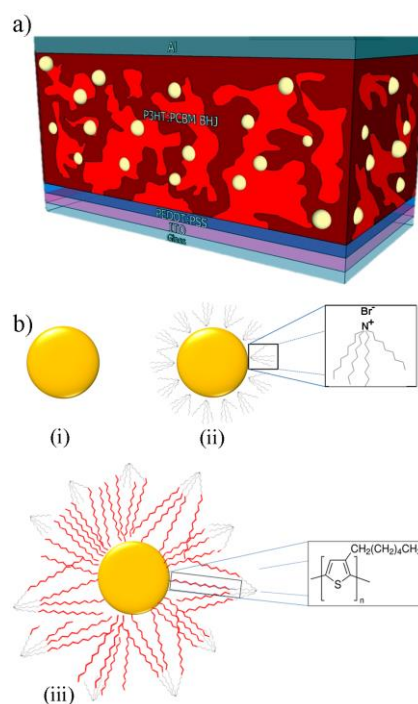


**Figure 6.26** a) Schematic representation of the BHJ OPV cell architecture; b) the three types of NPs embedded into the active layer, namely bare (i) TOAB- (ii) and P3HT-terminated (iii).<sup>142</sup>

These cells are based on the configuration ITO/PEDOT:PSS/P3HT:Fullerene/interlayer(optional)/Al with three different types of Au NPs embedded into the active layer. The corresponding UV-Vis absorption spectra of the optimized P3HT:PCBM-based devices in each case are shown in Figure 6.27a. The red shoulder at 602nm indicates the effective self-organization of the regioregular P3HT. In the spectral region between 450 and 650nm where the P3HT:PCBM absorbs, an increase in the percentage of absorbance is occurred for all NPs based OPVs. Figure 6.27b presents the respective absorption enhancement (ratios of the absorption spectra of the Au NPs-based devices to that of the pristine one), together with the extinction (scattering plus absorption) spectra for 8 nm Au NPs embedded in P3HT:PCBM media, as calculated using Mie theory. For the calculation of these extinction spectra the optical constants of P3HT:PCBM were used<sup>28</sup> leading to a red-shift of the resonance peak with respect to that recorded in ethanol. Notably, the absorption enhancement for bare as well as Au:P3HT NPs doped devices exhibits maximum at 610 nm, which fairly coincides with the extinction peak of the Au NPs, indicating that absorption improvement is due to the LSPR effect. The long tail to the absorption enhancement curves towards lower wavelengths suggests efficient scattering from larger diameter Au NPs aggregates formed during the spin coating process. On the contrary, for the Au:TOAB doped devices the absorption enhancement is lower and the LSPR effect is weaker; this is probably due to the adverse effect of TOAB ligand, which acts like an optical spacer between the NPs and polymer absorber, giving rise to a decreased plasmon optical field at the donor chains in the vicinity of NPs.

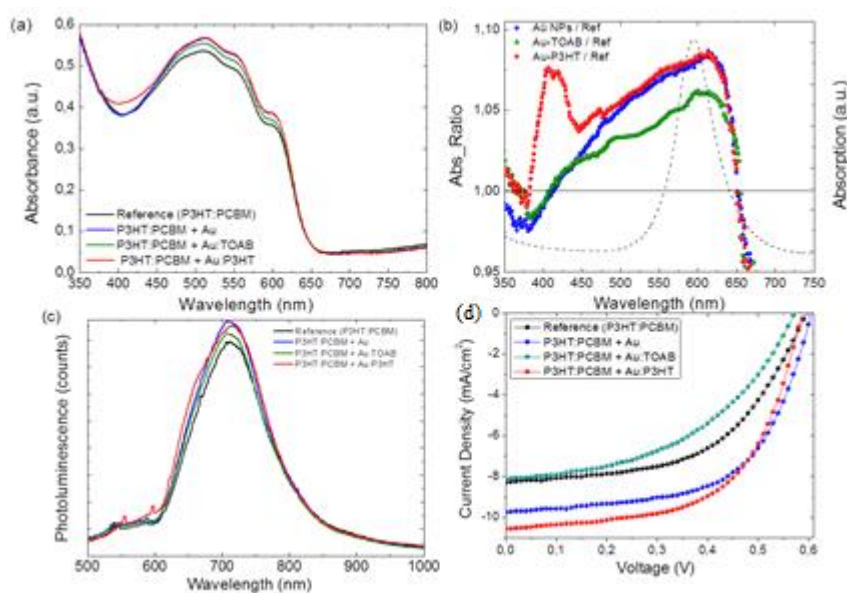


**Figure 6.27** a) Absorption spectra of the BJJ OPV devices with different types of Au NPs embedded into the active layer (the absorbance is baseline corrected with the PEDOT:PSS/ITO/glass substrate as a reference). b) Absorption enhancement factor of the devices (relative ratios of the absorption spectra of NPs-embedded devices to that of the pristine one). The calculated extinction spectrum of Au NPs embedded in the P3HT:PCBM medium is plotted for comparison (dashed line). The dielectric constants of P3HT:PCBM were obtained from Ref. c) Normalized PL spectra of reference and P3HT:PCBM active layers blended with different types of Au NPs. Each spectrum is normalized by the respective active layer absorption at the excitation wavelength. d) J-V characteristics of reference and OPV devices of the configuration ITO/PEDOT:PSS/P3HT:PCBM/Al, incorporating different types of Au NPs into the active layer.<sup>142</sup>

The photoluminescence (PL) spectra of the P3HT:PCBM-based devices with Au NPs embedded in the active layer in various concentrations are shown in Figure 6.27c. In all cases, the incorporation of Au NPs, leads to broader PL spectra and an increase of the PL. Such enhancement can be attributed to the fact that the LSPR excitation increases the light absorption and, thereby, enhances the exciton generation rate. Moreover, the enhanced PL intensity can arise from the strong coupling between the excitonic state of P3HT and the plasmonic field of the NPs, which is due to the propagating oscillation of the surface plasmon dipole plasmonic field and excitons. To verify that the enhancements presented in Figure 6.27 are a fair representation of the light absorbed into the active layer and subsequent exciton generation, we have fabricated a series of OPV devices. Figure 6.267 shows the current-voltage (J-V) characteristics for a series of eight different cells in each case for the P3HT:PCBM photoactive blend. The respective averaged photovoltaic characteristics are summarized in Table VI. It is observed that the incorporation of Au:P3HT NPs in both active layers induces a significant improvement of both the device short-circuit current ( $J_{SC}$ ) and the fill factor (FF), whereas the open-circuit voltage ( $V_{OC}$ ) remains constant. As a result, a 37.2 % increase in PCE is obtained compared to the reference device. The situation is similar to the case of devices doped with ablated Au NPs, where a 20.3% increase in PCE is attained. On the contrary, the Au:TOAB doped devices

exhibited inferior performance compared to either of the above cases as well as to the reference device.

Table VI. Photovoltaic characteristics of solar cells of the configuration ITO/PEDOT:PSS/P3HT:PCBM/Al, incorporating different types of Au NPs into the photoactive P3HT: PCBM layer.

	$J_{sc}$ (mA/cm <sup>2</sup> )	$V_{oc}$ (V)	FF (%)	PCE (%)	$\mu_h$ (cm <sup>2</sup> /Vs)
P3HT:PCBM	8.30 ± 0.12	0.60±0.02	53.83 ± 0.30	2.66 ± 0.05	8.98x10 <sup>-4</sup>
P3HT:PCBM + Au	9.45 ± 0.21	0.60±0.03	56.65 ± 0.32	3.20 ± 0.09	1.17x10 <sup>-3</sup>
P3HT:PCBM + Au:TOAB	8.15 ± 0.11	0.57±0.03	46.74 ± 0.21	2.18 ± 0.04	7.83x10 <sup>-4</sup>
P3HT:PCBM + Au:P3HT	10.54 ± 0.26	0.59±0.02	58.90 ± 0.34	3.65 ± 0.11	1.26x10 <sup>-3</sup>

In order to investigate the underlying mechanism responsible for the enhanced performance of the devices, the incident photon-to-electron conversion efficiency (IPCE) curves of the respective devices were recorded (Figure 6.28a). The corresponding increase in IPCE (DIPCE) is presented in 6.27 inset. It can be observed that IPCE increases considerably upon the incorporation of bare and Au:P3HT NPs, which complies with the enhanced  $J_{SC}$  observed in both cases, indicating photocurrent generation from light harvested by the NPs. In particular, IPCE of both types of devices, becomes enhanced in a broad spectral range (480 to 700nm), while it maximizes at 580 nm. This wavelength regime practically coincides with the spectral range in which the optical absorption of the Au-NPs embedded in P3HT:PCBM medium is enhanced due to the LSPR effect. On the contrary in the Au:TOAB doped devices although an absorption enhancement factor was obtained, IPCE decreases compared to the reference cell. Considering that DIPCE for bare and Au:P3HT NPs becomes maximum close to the plasmon absorption peak, IPCE enhancement can be attributed to the local enhancement of the incident electromagnetic irradiation field in the vicinity of small sized NPs, due to LSPR effects. An effect, that explains the observed disparity between the absorption and the IPCE enhancement. In this context we postulate that the reason for the IPCE substantial decrease observed for Au:TOAB NPs, despite the absorption enhancement, may be due to the deterioration of the active layer morphology, as a result of the interaction of the TOAB surfactant molecules with the active polymer chains. This further suggests that in the presence of P3HT ligands, the blend morphology is not disturbed.

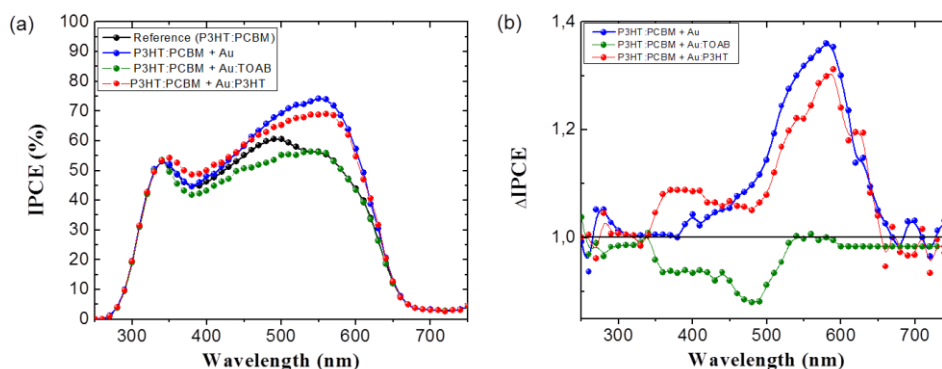


**Figure 6.28** a) IPCE curves of reference and OPV devices incorporating different types of Au NPs into the active layer. b)  $\Delta$ IPCE curves (relative ratios of the IPCE spectra of NPs-embedded devices to that of the pristine one) of the respective plasmonic devices<sup>142</sup>

In a first attempt to investigate the effect of NPs ligand shell on active layer morphology, atomic force microscopy (AFM) studies of the surfaces of the different blends were conducted. As shown in Figure 6.29, the BHJ layer of the best OPV devices showed increased roughness compared to the reference and Au:TOAB NPs doped ones. Besides this, the Au:P3HT NPs doped blend showed much coarser texture with broad hill-like features, compared to the other BHJ layers. It has been suggested that a rough P3HT:PCBM surface indicates enhancement of the ordered structure that assists exciton dissociation.

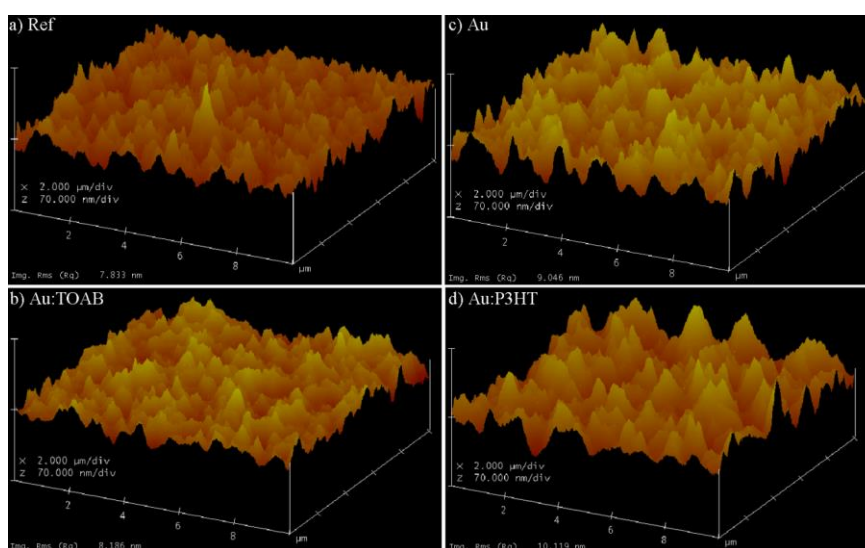


**Figure 6.29** AFM images of the reference-(a), bare NPs doped-(b), Au:TOAB NPs doped-(c) and Au:P3HT NPs doped-(d) BHJ layers. The rms roughness of the respective surfaces is indicated.<sup>142</sup>

Moreover, it has been reported that increase of blend roughness will give rise to a corresponding increase of the interface area between the anode and the active layer, providing shorter routes for holes to travel to the anode and thus enhancing hole mobility. To test this in our case, hole-only devices were fabricated for all different types of devices. As shown in Table VI the hole mobilities of the reference device as well as those blended with surfactant-free Au, Au:TOAB and Au:P3HT NPs

respectively are calculated from the currents in the square law region to be  $8.98 \times 10^{-4}$ ,  $1.17 \times 10^{-3}$ ,  $7.83 \times 10^{-4}$  and  $1.26 \times 10^{-3} \text{ cm}^2 \text{V}^{-1} \text{s}^{-1}$  respectively. Therefore, it is clear that the hole mobility decreases for the Au:TOAB NPs doped cells due to inferior hole transport. Finally, the reduced mean distance between generated holes and PEDOT:PSS occurring in rough blends could weaken the dependence of holes collection on the external field and thus explain the FF improvement of the respective devices. An additional direct evidence for the inferior transport properties of the Au:TOAB NPs-based blends compared to those incorporating surfactant-free and Au:P3HT NPs is provided by time-resolved PL (TRPL) spectroscopy.

TRPL measurements are widely used to determine the exciton lifetime and in our case could provide insight into the dynamics of the photogenerated excitons. Figure 6.30 displays the PL intensity decay profiles obtained for the different blends onto PEDOT:PSS layers. The PL decay data were adequately fitted using a double exponential function and the associated fitting parameters are listed in Table below.

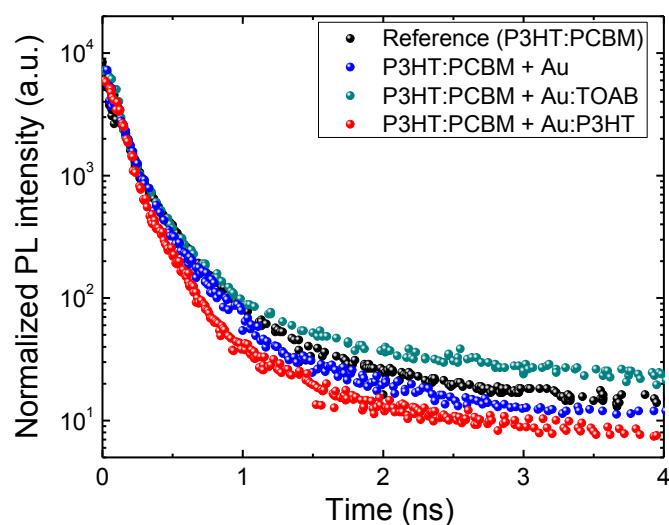


**Figure 6.30** TRPL decay profiles for the reference (P3HT:PCBM) and plasmonic blends incorporating Au NPs terminated with different ligands<sup>142</sup>

**Table VII:** TRPL decay fitting parameters

Sample	I <sub>1</sub> (%)	$\tau_1$ (ns)	I <sub>2</sub> (%)	$\tau_2$ (ns)	$\tau_{exc}$ (ns)
P3HT:PCBM	86.7	0.100	13.3	0.400	0.140
P3HT:PCBM + Au:P3HT	84.0	0.095	16.0	0.350	0.116
P3HT:PCBM + Au	89.1	0.100	10.9	0.390	0.132
P3HT:PCBM + Au:TOAB	74.9	0.130	25.1	0.780	0.293

The corresponding effective exciton lifetimes,  $\tau_{exc}$ , were calculated to be 140 ps, 116 ps, 132ps and 293 ps for the reference, Au:P3HT, bare Au, and Au:TOAB based blends respectively. The exponential fitting of the PL decay can provide insight on the timescale of the excitons dissociation into charge pairs within the blend. Accordingly, the almost twice slower decay time measured in Au:TOAB based blends can be attributed to a deficient exciton dissociation and thus charge separation. This qualitatively suggests that in this blend the fullerene regions may not be in close proximity to the polymer and that excitons need to diffuse for longer time to reach a donor/acceptor interface compared to the blend with Au:P3HT NPs. The TRPL results above further support the inhibition of the charge transfer process due to the inferior morphology of the Au:TOAB-based blend. Our results above suggest that the closer the proximity of the NPs metallic core to the active layer polymer components, as occurs in the cases of bare and Au:P3HT NPs, appears to be an efficient way to suppress disruption of the active layer morphology and thus recombination pathways via NPs induced subgap traps.

In summary, we have revealed the strong impact of NPs ligand shell on the performance of plasmonic BHJ organic solar cells. In particular, we identified that for our OPV systems, improved PCE can be only be obtained when the NPs metallic core is in direct contact with the active layer polymeric components. In particular, it is found that the effect of NPs coating is two-fold. A minor effect is that the ligand group may act as an optical spacer between the NPs and polymer absorber, giving rise to a decreased plasmon optical field. The major effect, however, is that the morphology of the BHJ blend and in series the OPV performance are substantially influenced by the NPs' terminating coating. We envisage that this work brings about a new thinking and practices in the effort to maximize PCE via plasmonic nanostructures' mediated light harvesting effects.

## 6.8 Incorporation of ligand coated Au NRs in ETL

In the final part of this thesis, is presented our study regarding the further trapping and the exploitation of the photons that are transmitted through the active layer of a bulk heterojunction organic photovoltaic device towards the further improvement of the device performance. A significant enhancement in power conversion efficiency of PCDTBT:PC<sub>71</sub>BM and PTB7:PC<sub>71</sub>BM by ~13 and ~8% respectively with a record efficiency of 8.25% for the latter, was observed which can be attributed both to the high scattering efficiency of gold nanorods that were embedded inside the titanium sub oxide back contact electron transport layer as well as to the gold nanorods that partially protruded inside the active layer, where the incident light initiate localized surface plasmon resonance effect at the vicinity of NRs. We have performed a comprehensive optical and electrical characterization of our devices to clarify the influence of gold nanorods on exciton generation, dissociation, and charge recombination and transport inside the thin film devices.

Fig. 6.31a shows UV-Vis absorption spectra of pristine and Au NRs doped PTB7:PC<sub>71</sub>BM based devices. The addition of Au NRs inside the back contact ETL, result in a broad enhancement of the active layer absorption that can be attributed to light scattering of the transmitted photons by the Au NRs for both photoactive blends based devices. Therefore, the Au NRs can act as an effective “optical reflector” for solar light; multiple reflections will cause the light to pass through the BHJ film, which would otherwise be lost and will not contribute to exciton generation. On the other hand, the LSPR effect cannot be clearly observed since the NRs are located outside the active layer in which the near field effect can only be observed if the metal NPs are embedded inside the photoactive layer.

A series of BHJ photovoltaic devices were fabricated with structure of ITO/PEDOT:PSS(30 nm)/PCDTBT or PTB7:PC<sub>71</sub>BM/TiO<sub>x</sub>/Al(100 nm) by using Au NRs as back contact reflectors. Specifically, different volume ratios of Au NRs (0, 1.5% (v/v)) were incorporated in the TiO<sub>x</sub> ETL. The device structure is schematically shown in Fig.6.31b, while Fig.6.31c displays the respective current density-voltage (J-V) characteristics for PCDTBT and PTB7-based devices. with and without Au NRs, under illumination with 100 mW/cm<sup>2</sup> power intensity. The respective averaged photovoltaic characteristics are summarized in Table VIII.

Device	Jsc(mA/cm <sup>2</sup> )	Calculated Jsc (EQE)	Voc (V)	FF(%)	PCE (%)	Rs (Ω cm)	Rsh (Ω cm)
PCDTBT (TiO <sub>x</sub> )	10.87±0.21	10.61±0.32	0.890±0.02	61.7±0.4	5.96±0.18	8.13	555
PCDTBT (TiO <sub>x</sub> :AuNRs)	12.03±0.26	11.69±0.36	0.89±0.04	62.9±0.5	6.75±0.22	4.60	769
PTB7 (TiO <sub>x</sub> )	16.27±0.22±	15.75±0.38	0.760±0.03	60.1±0.5	7.43±0.19	10.15	472
PTB7 (TiO <sub>x</sub> :AuNRs)	17.17±0.29	16.71±0.41	0.760±0.02	61.4±0.6	8.01±0.24	5.71	609

Table VIII: Average photovoltaic characteristics for OPV devices with (optimum) and without Au NRs back reflectors. To account for experimental errors, the reported averages for each case are taken for 10 identical devices, consisting of six photovoltaic cells each.

It is shown that the incorporation of Au NRs inside the  $\text{TiO}_x$  on top of the active layer induces an enhancement of  $\sim 11\%$  and  $\sim 6\%$  to the short-circuit current ( $J_{sc}$ ) for PCDTBT and PTB7 respectively, and an enhancement of  $\sim 2\%$  to the fill factor (FF) for both blends, whereas the open-circuit voltage ( $V_{oc}$ ) remain constant. As a result, an increase of  $\sim 13\%$  and of  $\sim 8\%$  for PCDTBT and PTB7 respectively is observed in the plasmonic device efficiency after the incorporation of Au NRs. The Au NRs doped device exhibits a power conversion efficiency (PCE) of 8.25% for PTB7 based devices ( $V_{oc}=0.76$  V, short-circuit current:  $J_{sc}=17.46$  mA/cm<sup>2</sup>, fill factor: FF=0.62). The lower enhancement in the case of PTB7 compared to PCDTBT based devices can be attributed to the fact that PTB7:PC71BM photoactive blend has higher extinction coefficient compared to PCDTBT:PC71BM, and as a result absorbs more incident photons allowing less to transmit and reach the Au NRs based reflectors. This significant performance enhancement can be attributed to the high scattering efficiency of the Au NRs, which traps the transmitted photons inside the photoactive layer in order to increase absorption probability.

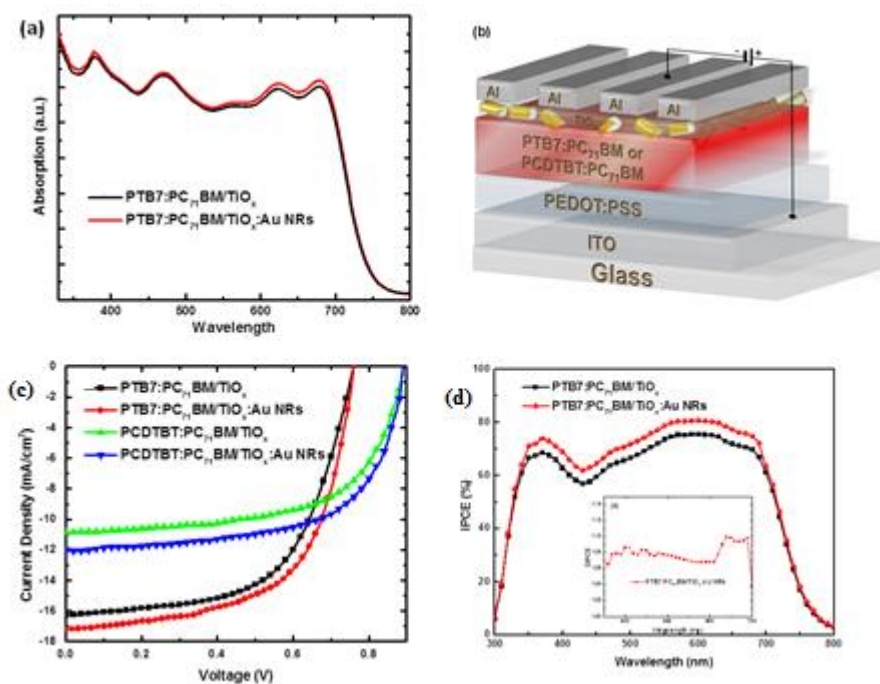


**Figure 6.31** (a) UV-Vis absorption spectra of pristine and Au NRs doped PTB7:PC71BM based devices, (b) Schematic illustration of the fabricated plasmonic BHJ OPV device, (c) Current density-voltage (J-V) curve for PTB7 based active layer, (d) IPCE and DIPCE (inset) spectra for the devices with and without Au NRs

In order to get an insight for the responsible mechanism of the enhanced device performance, the incident photon-to-electron conversion efficiency (IPCE) curves (Fig. 6.31d) of the plasmonic device was measured and compared with the pristine one. The pristine device exhibits a maximum IPCE of

~69% and ~75%, while the Au NRs doped devices exhibit an enhanced maximum of ~75% and ~81% for PCDTBT and PTB7 respectively. As shown in Fig.4c,d, the IPCE enhancement is broad and almost uniform ranging from 350 to 600 nm, showing also a distinct peak at ~650 nm which can be directly attributed to the longitudinal surface plasmon resonance of Au NRs. Thus, we can suppose that the NRs may protrude inside the active layer, allowing the utilization of surface plasmon resonance effects for enhanced exciton dissociation resulted from the local electric field at the vicinity of NRs. The IPCE increases remarkably upon the introduction of Au NRs, which complies with the enhanced Jsc observed. This can be mainly attributed to scattering effects as the enhancement in the IPCE spectrum is broad. The Au NRs doped devices significantly outperforms the pristine one, owing to a dual plasmonic effect. The enhancement caused by Au NRs is a contribution of scattering effects of the small aspect ratio NRs locate inside the TiO<sub>x</sub> ETL and LSPR of the high aspect ratio NRs that penetrate inside the photoactive layer. It can be confirmed from the DIPCE spectra of both blends that we have a synergetic effect of LSPR and scattering from Au NRs. It should also be noted that the integrated Jsc values from the IPCE spectrum as presented in Table VIII for the pristine and the Au NRs based devices are 10.61 and 11.69 mA cm<sup>-2</sup> respectively for PCDTBT:PC71BM, while in the PTB7 case are 15.75 and 16.71 mA cm<sup>-2</sup>. The IPCE calculated values are less than 3% different than the actual measured Jsc values, indicating good accuracy of the OPV measurement.

In order to confirm that the Jsc is increased due to improved light harvesting in the active layer, the diffuse reflectance of the devices was recorded. Fig. 6.32a show the reflectivity spectra of the devices fabricated with and without Au NRs on top of both photoactive blends. The lower reflectivity of the NRs embedded devices in the whole spectrum clearly indicates stronger absorption of the incident light due to scattering. The scattering effect of the Au NRs increases the effective length of the optical path, which in turn increases the generation of electron-hole pairs. This enhanced optical absorbance is directly related to the improved Jsc and PCE levels in the NRs doped BHJ devices.

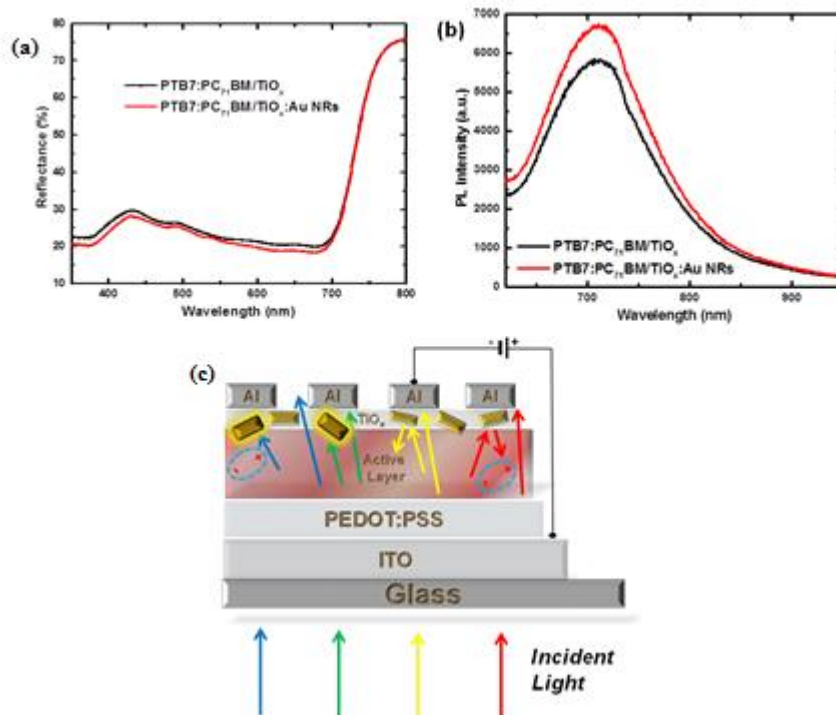


**Figure 6.32** (a) Diffuse reflectance spectra of the devices fabricated with and without Au NRs for PTB7 based active layer, (b) Photoluminescence (PL) spectra of the BHJ devices with and without Au NRs for PTB7 based active layer, (c) The schematic figure of Au NRs ETL doping explaining the light trapping mechanism.

The photoluminescence (PL) spectra of the films with and without Au NRs are presented in Fig. 6.32b in order to further validate the calculated enhanced exciton generation. The incorporation of the Au NRs, leads to broader PL spectra and an increase of the PL intensity by 15% for PCDTBT and by ~13% for the PTB7 based blend. The broadening and enhancement of the PL intensity can be attributed to the fact that the LSPR excitation of the protruded NRs and the light scattering of the NRs inside the TiO<sub>x</sub> increases the degree of light collection, thereby, leading to enhanced light excitation rate. Moreover, the enhanced PL intensity can arise from the strong coupling between the excitonic state of the polymer and the plasmonic field of the NRs, which is due to the propagating oscillation of the surface plasmon dipole plasmonic field and excitons. Thus it can be concluded that the incorporation of Au NRs significantly increases the exciton generations..

OPV devices with significantly enhanced PCEs (exceeding 8%) have been demonstrated by doping the rear ETL with Au NRs to enhance light trapping within the BHJ layer. NRs were embedded inside the TiO<sub>x</sub> ETL at the rear side of OPV enabling the construction of novel light trapping architecture to enhance light absorption. The enhanced light trapping is systematically investigated through detailed processing, characterization, microscopy, and device optimization. We attributed the recorded PCE enhancement to the efficient light trapping by the high efficient Au scattering elements located inside the TiO<sub>x</sub> and to the LSPR effects by the NRs that partially protruded inside the active layer, enabling the utilization of the near field effect caused by Au NRs. The

successful demonstration of these novel device architecture provides a very useful design guideline for achieving efficient light harnessing in thin film OPVs.

## Chapter 7

### Conclusions and Future Directions

#### 7.1 Conclusion

In summary, our group made an important contribution in the understanding of the underlying operation mechanism and optimization of plasmonic OPVs by demonstrating experimental results of incorporation of Au or Al NPs into P3HT:PCBM photoactive layer in order to understand the effect of NPs in the efficiency and stability of the devices. Moreover, we have demonstrated that by incorporating Au and Al NPs in PCDTBT:PC<sub>71</sub>BM photoactive layer the magnitude of enhancement in device performance is smaller and this may be attributed to the superior morphology of PCDTBT:PC<sub>71</sub>BM, compared to P3HT:PCBMblend. As a results the enhancement observed in P3HT:PCBM-based plasmonic OPVs can be attributed to both morphology improvement and plasmonic effects (LSPR and scattering). On the contrary, the enhancement observed in PCDTBT:PC<sub>71</sub>BM -based plasmonic OPVs can be mainly attributed to plasmonic effects. Furthermore the incorporation of Au NRs inside the TiO<sub>x</sub> ETL significantly enhanced the efficiency of PTB7:PC<sub>71</sub>BM based devices due to efficient light trapping through superior scattering efficiency of Au NRs located inside the ETL on top of the active layer and to LSPR effects of the high aspect ratio Au NRs that partially protruded inside the active layer that enables the utilization of near-field effect.

#### 7.2 Future work

Work is in progress in order to quantify the contribution of LSPR and scattering effects respectively. The following future directions are planned to be addressed:

- The simultaneous incorporation of plasmonic NPs in different layers of an OPV device in order to identify the optimum combination of the various plasmonic effects.
- Enhancement of the OPV performance by light trapping via using ordered arrays of plasmonic metallic NPs (SPP).
- Development of a theoretical inglight harvesting mechanisms taking place upon
- Incorporation of plasmonic graphene nanostructures. In particular, functionalization of graphene derivatives with plasmonic NPs and subsequent incorporation into the devices as transparent electrode will be investigated. The purpose is to fabricate OPVs onto flexible substrates, such as PET.

- Extend the fabrication of plasmonic OPV devices onto large scale flexible substrates by printing all the individual layers of the device including the plasmonic metal nanoparticles by converting the obtained solutions to high viscosity inks in order to bring the plasmonic OPVs closer to the commercialization.

## List of Publications

1. Kakavelakis G., Stratakis E., Kymakis E., Aluminum nanoparticles for efficient and stable organic photovoltaics (2013), RSC Advances, 3 (37), 16288-16291
2. Kakavelakis G., Stratakis E., Kymakis E., Synergetic Plasmonic Effect of Al and Au Nanoparticles for Efficiency Enhancement of Air Processed Organic Photovoltaic Devices, (2014), Chemical Communications, 50 (40), 5285 - 5287 [2014 Emerging Investigators Issue]
3. Kakavelakis G., Konios D., Stratakis E., Kymakis E., Enhancement of the Efficiency and Stability of Organic Photovoltaic Devices via the Addition of a Lithium-Neutralized Graphene Oxide Electron-Transporting Layer (2014), Chemistry of Materials, 26 (20), 5988–5993
4. Stylianakis M.M., Sygletou M., Savva K., Kakavelakis G., Kymakis E., Stratakis E., Photochemical Synthesis of Solution-Processable Graphene Derivatives with Tunable Bandgaps for Organic Solar Cells (2015), Advanced Optical Materials, 5, 658-666 [Appeared in the inside front cover of Adv. Opt. Mater]
5. Konios D., Petridis C., Kakavelakis G., Sygletou M., Savva K., Stratakis E., Kymakis E., Reduced graphene oxide micromesh electrodes for large area, flexible organic photovoltaic devices (2015), Advanced Functional Materials, 25, 15, 2213-2221 [Appeared in the inside front cover of Adv. Funct. Mater]
6. Kymakis E., Spyropoulos G.D., Fernandes R., Kakavelakis G., Kanaras A.G., Stratakis E., Plasmonic bulk heterojunction solar cells: The role of nanoparticle ligand coating (2015), ACS Photonics, 2 (6), 714–72
7. Sygletou M., Kakavelakis G., Paci B., Generosi A., Kymakis E., Stratakis E., Enhanced stability of Aluminum nanoparticles doped organic solar cells, Accepted, ACS Appl. Mater. Inter. (2015)